POLITECNICO DI MILANO

Scuola di Ingegneria Industriale e dell'Informazione

Corso di Laurea Magistrale in Ingegneria Aeronautica

Ocean Liming: a LES analisys of feasibility and effects of discharging slaked lime in the wake of a ship

Supervisor:

Prof. Antonella ABBA'

Authors:

Matteo COPERCINI, Matr. 920455
Francesco CUSMAI, Matr. 916053

Academic year 2019-2020

Abstract

Climate change is one of the biggest challenges for humans in the modern world. Specifically, global warming due to greenhouse gases emissions constitutes a big part of it. Objective of The Paris Agreement, signed in 2016, is to maintain the global average temperature rise well below 2°C above pre-industrial levels. However, global warming is strictly linked to another problem related to climate change: ocean acidification. Although various strategies that aim at counteracting global warming have been recently proposed and discussed, few are the technological solutions that prevent simultaneously global warming and ocean acidification. Among these, Ocean Liming technique is based on the idea of sequestering atmospheric carbon dioxide adding alkalinity to seawater, obtained by dissolution of slaked lime. The aim of this thesis work is to investigate the feasibility of Ocean Liming with the assessment of the calcium hydroxide concentration and seawater pH in the wake of a ship, conducted with a three-dimensional reactive CFD modelling, in order to incorporate dynamic chemical parameters. The simulations have been conducted with a parallel Finite Differences – Large Eddy Simulation solver, wrote in Fortran 90. The work is divided in two main parts. The first one is focused on the code validation process, with the analysis of a laminar Poiseuille channel flow and a turbulent round jet. The second one consists in the simulation of slaked lime discharge in the near wake of a ship. In particular, the proposed configurations differ in slaked lime mass flow rate, type of injection (single or double) and the operational regime of the ship propeller (modelled with R-BET physical model). To complete the study, a preliminary analysis of the hull ship (modelled with a bluff body) effect on slaked lime dissolution is presented. The results are proposed with a study of space and time evolution of slaked lime concentration levels and pH variation across the computational domain. The solver could be used for future developments on this field of research, with the study of different slaked lime discharge configurations.

Sommario

Il cambiamento climatico è una delle più grandi sfide della società contemporanea per l'uomo. Uno dei maggiori fattori che contribuiscono a questo cambiamento è il surriscaldamento globale, dovuto ai gas responsabili dell'effetto serra. L'Accordo di Parigi, firmato nel 2016, si pone come obiettivo quello di mantenere l'aumento della temperatura media globale di 2°C sotto i livelli preindustriali. Strettamente collegato al riscaldamento globale vi è un altro problema, quello dell'acidificazione degli oceani.

Il livello di diossido di carbonio atmosferico (CO_2) non solo causa l'aumento della temperatura dell'acqua negli oceani, ma a causa del ciclo del carbonio influenza anche il valore del pH acquatico. Il motivo di ciò è che la CO_2 è uno dei pochi gas atmosferici a reagire con l'acqua, la maggior parte degli altri gas semplicemente vi si dissolve. Questa reazione chimica tende a far diminuire il pH dell'acqua, creando un fenomeno di acidificazione. Il continuo aumento dell'acidità può danneggiare l'ecosistema marino, ad esempio inibendo la formazione del carbonato di calcio, un composto fondamentale per la formazione di conchiglie, plancton e barriere coralline.

Per ottemperare agli obiettivi dell' Accordo di Parigi, in futuro potrebbe rivelarsi necessario non solo limitare l'emissione dei gas serra, ma persino abbassarne i quantitativi in atmosfera. Nonostante recentemente siano state discusse e proposte varie strategie volte a contrastare il surriscaldamento globale, esistono ancora poche tecnologie che riescano a prevenire sia il riscaldamento che l'acidificazione degli oceani. Citiamo l'esperimento LOHAFEX e l'Ocean Liming tra le tecnologie ad emissione negativa. Il primo consiste nell'idea di utilizzare il solfuro di ferro come fertilizzante per la crescita delle alghe, aumentando così la richiesta nonché l'assorbimento di CO_2 da parte dell'oceano. Purtroppo, però, la rimozione di CO_2 è sotto le aspettative, in quanto i piccoli organismi tendono a mangiare le alghe (Bathmann [25th May 2009, Rome]). L'altra soluzione, discussa e trattata in dettaglio nella tesi, si basa sull'idea di aumentare l'assorbimento di CO_2 dall'atmosfera tramite l'aggiunta di alcalinità all'acqua, ottenuta disciogliendo calcina (idrossido di calcio o calce spenta). L'ideatore di questa strategia fu Kheshgi [1995]. Tuttavia, riguardo questa soluzione non ci sono attualmente molte informazioni sulla fattibilità, i limiti e gli effetti collaterali. L'impatto locale vicino al punto di rilascio della calcina è un fattore critico nel valutare gli effetti indesiderati dell'Ocean Liming, dal momento che questo produce un aumento di alcalinità. Un aumento eccessivo del pH

potrebbe essere dannoso per l'intera biologia dell'oceano; alcuni organismi, come i copepodi, soffrono l'aumento di alcalinità molto più che altri organismi (Cripps et al. [2014]; Taucher et al. [2017]).

Una valutazione preliminare al problema è stata fatta nell'articolo Caserini et al. [2021], frutto di una collaborazione tra il Dipartimento di Scienze e Tecnologie Aerospaziali (DAER) e il Dipartimento di Ingegneria Civile e Ambientale (DICA) del Politecnico di Milano, che si colloca all'interno di un progetto più ampio (Desarc-Maresanus). In tale articolo vengono seguiti due approcci per modellare l'andamento della concentrazione di calcina nella scia di una nave: un modello CFD non-reattivo tridimensionale e uno monodimensionale ma reattivo. Lo scopo di questa tesi è di investigare ulteriormente questa soluzione, valutando l'andamento della concentrazione di idrossido di calcio rilasciato nella scia di una nave. Lo studio viene condotto tramite un modello CFD tridimensionale e reattivo, in modo da tenere in considerazione i parametri chimici dinamici. In particolare ci si concentra sull'analizzare il comportamento delle particelle di idrossido di calcio nella regione di scia più vicina alla nave; il codice utilizzato è stato scritto in Fortran90 ed è un solutore parallelo a Differenze Finite con approccio Large Eddy Simulation. Il lavoro è suddiviso principalmente in due parti. La prima parte è focalizzata sul processo di validazione del codice, tramite l'analisi di un flusso laminare di Poiseuille e un getto turbolento. La prima configurazione di flusso è servita a verificare il corretto funzionamento sia della parallelizzazione, scritta con standard MPI, che del solutore di pressione adottato, con uno sguardo alle prestazioni di scalabilità del codice. Al contrario, lo studio del getto turbolento è incentrato sull'analisi delle statistiche turbulente di velocità, confrontandole con i dati di esperimenti e di simulazioni terze. Tali simulazioni hanno avuto lo scopo di verificare il corretto funzionamento del modello di sforzi di sottogriglia implementato, così come condurre un'analisi di convergenza della griglia di calcolo. La seconda parte del lavoro consiste nel simulare il rilascio di calcina nella regione più prossima della scia di una nave. Le simulazioni svolte differiscono principalmente per la portata massica di calcina, il tipo di iniezione (a orifizio singolo o doppio orifizio) e il regime di funzionamento dell'elica della nave (simulata con il modello fisico della R-BET). Lo studio è completato con l'analisi preliminare dell'influenza dello scafo della nave, modellato con un bluff body, sul processo di dissoluzione di idrossido di calcio in acqua. I risultati ottenuti sono presentati tramite uno studio dell'evoluzione spazio-temporale dei livelli di concentrazione di calcina e variazione del pH dell'acqua marina all'interno del dominio di calcolo. Il codice sviluppato potrà essere utilizzato per futuri sviluppi in questo campo di ricerca, con lo studio di diverse configurazioni di iniezione di idrossido di calcio in oceano.

Contents

List of Figures

List of Tables

List of Symbols

The most significant symbols used in this thesis are summarized hereafter

$(\cdot)'$	Residual variable
$(\cdot)_{sgs}$	Subgrid-scale variable
$< (\cdot) >$	Mean variable
α	Ratio between mass loss and mass transfer to bulk
β	Blade angle
$\boldsymbol{\omega}$	Vorticity vector
$\boldsymbol{u}$	Velocity vector
$\boldsymbol{x}$	Coordinates vector
δ_*	Initial momentum thickness
$\dot{m}$	Mass flow rate
ϵ	Rate of energy transfer
ϵ_{prop}	Propeller thickness
η	Dynamic viscosity
η_θ	Obukhov-Corrsin length scale
η_K	Kolmogorov length scale
$\hat{G}$	Filter Kernel in spectral space
λ	limiting ionic conductance
$\widetilde{(\cdot)}$	Test-filtered variable

ν	Kinematic viscosity
ω	Propeller rotational velocity
ϕ	Flow angle
Φ_0	Diffusion potential
ρ	Density
ρ_p	Slaked lime particle density
τ^R	Residual-stress tensor
τ^r	Anisotropic residual-stress tensor
τ_c	Cutoff time
$\overline{(\cdot)}$	Filtered variable
$\overline{\Delta}$	Cutoff length
B	Empirical constant
B_s	Empirical constant for similarity
C	Concentration
c	Chord length
C_0	Initial concentration
C_D	Drag coefficient
C_L	Lift coefficient
C_{max}	Slaked lime maximum concentration
C_{nr}	Concentration of a non-reactive substance
C_s	Smagorinsky constant
D	Diffusivity
$D(t)$	Dilution factor at time t
d_0	Discharge orifice diameter
D_{jet}	Jet diameter

D_{prop} Propeller diameter

d_p Slaked lime particle diameter

F Faraday constant

f Tip effect coefficient

G Filter Kernel in physical space

G_{Gauss} Gaussian kernel

$I(t)$ Dissolved $Ca(OH)_2$ at time t

J Advance ratio

K Ion valence

K Kinetic energy

k_η Kolmogorv wave number

k_θ Obukhov-Corrsin wave number

k_B Batchelor wave number

k_c Cutoff wave number

L Reference length

n Rotational velocity in rps

N_B Number of blades

P pressure

p Isotropic term of stress tensor

Pe Peclet number

Pr Prandtl number

R Universal gas constant

$r_{1/2}$ Jet half width

$R_{bluffbody}$ Bluff body radius

R_{jet} Jet radius

r_{p0}	Slaked lime initial particle radius
r_p	Slaked lime particle radius
Re	Reynolds number
S	Jet spreading rate
s	Curvilinear abscissa along streamline from injection location
S_C	Concentration source term
S_{ij}	Strain-rate tensor
S_{r_p}	Particle radius source term
Sc	Schmidt number
SW	Ship width
T	Temperature
t	Time
U_0	Jet centerline velocity
U_θ	Tangential velocity component for propeller
U_e	Co-flow velocity
U_{in}	Inlet axial velocity
U_j	Maximum axial velocity of the inlet profile
U_{ref}	Reference velocity
U_{rel}	Relative velocity between flow and propeller
U_x	Axial velocity component for propeller
x_0	Virtual origin
pH	Measure of acidity/alkalinity of an aqueous solution
pH_0	Initial pH
pH_{max}	Maximum pH

Acronyms

ADI Alternating Direction Implicit method.

AIS Automatic Identification System.

BL Boundary Layer.

CFL Courant-Friedrich-Lewy number.

CPU Central Processing Unit.

DAER Dipartimento di Scienze e Tecnologie Aerospaziali.

DICA Dipartimento di Ingegneria Civile e Ambientale.

DNS Direct Numerical Simulation.

DWT Deadweight Tonnage.

IEA International Energy Agency.

IMO International Maritime Organization.

KCS KRISO Container Ship.

KRISO Korean Research Institute for Ships and Ocean engineering.

LDA Laser Doppler Anemometry.

LES Large Eddy Simulation.

MPI Message Passing Interface.

NS Navier-Stokes.

OL Ocean Liming.

PDE Partial Differential Equation.

PHREEQC pH Redox Equilibrium (in C language).

PIV Particle Image Velocimetry.

R-BET Rotating Blade Element Theory.

RADM Rotating Actuator Disk Model.

RANS Reynolds Averaged Navier-Stokes.

RHS Right Hand Side.

RK Runge Kutta.

SGS Subgrid Scale.

SPMD Single Program Multiple Data.

UNCTAD United Nations Conference on Trade and Development.

1. Introduction

In the last century the human activities with emissions of greenhouse gases and deforestation have exacerbate the problem of global warming. Anyway, global warming is strictly linked with another ecological problem: ocean acidification. A significant part of CO_2 present in atmosphere is absorbed by the oceans. Indeed, the carbon dioxide reacts with water, dissociating into bicarbonate, carbonate ions and H^+. The increased concentration of these ion species in seawater causes a reduction of its pH value. The seawater pH is a vital parameter for marine ecosystem. The process of ocean acidification can inhibit the production of calcium carbonate, an important substance for coral reefs, seashells and plankton, with indirect consequences for the other animal and vegetal marine species. Therefore, over the last decades many were the techniques proposed to counteract ocean acidification and global warming. Among these, the so-called Ocean Liming method consists in discharging alkaline substances into the ocean, in order to increase seawater pH and favour atmospheric CO_2 uptake by the ocean.

The present work is part of an internal collaboration of Politecnico di Milano between "Dipartimento di Scienze e Tecnologie Aerospaziali" (DAER) and "Dipartimento di Ingegneria Civile e Ambientale" (DICA), that belongs to a larger project (Desarc-Maresanus), and it is dedicated to the analysis of the OL technique from a fluidynamic point of view. In particular, it has been developed a parallel finite differences code for Large Eddy Simulation (LES), written in Fortran90. This solver has been employed to numerically simulate different configurations of slaked lime discharging in the near wake of a ship.

The first part gives an overview of the OL project. Starting from a chemical point of view, the ocean carbon cycle and the reaction between slaked lime (chosen in this work as alkaline substance) and water are discussed in details. Afterwards, the entire OL process is explained, from the production of slaked lime to its discharge into the ocean. Concerning the production phase, different methods are presented with their pros and cons. For the final stage of transportation and discharging, it is given a brief overview on the ideal candidates of vessel types for the success of the project. The analysis continues with the presentation of the main side effects that an increase of the ocean alkalinity can imply on the marine ecosystem. The final part of the chapter is dedicated to a brief outline of the slaked lime behaviour into the ship wake from a fluidynamic point of view and a broad cost analysis of the entire process.

The third chapter has the scope of presenting the physical model adopted in the numerical simulations. In detail, the Navier-Stokes equations and equations for the dynamics of slaked lime concentration and particle radius, developed starting from the considerations by Tannenberger and Klein [2009], are presented. Beside those, the seawater pH approximation model, developed by DICA (and presented in Caserini et al. [2021]), is described. As regards Navier-Stokes equations a deep insight is given to the Large Eddy Simulation approach, starting from the discussion on filtering and closure operations to the presentations of subgrid stress tensor model for the momentum equation and $Ca(OH)_2$ concentration and particle radius dynamics equations. Furthermore, the theory of propeller physical model is explained in depth, with a discussion on the propeller type chosen.

The subsequent chapters have as main focus the solver code. Chapter 4 is dedicated in the first part to the presentation of the numerical grid setup and numerical algorithm for time integration of the solved equations, discretization of the equations terms and pressure correction method for momentum equation. The last part consists in the explanation of the communication method between different processors for the parallelisation of the Fortran90 code and its scaling performance. On the contrary, chapter 5 is focused on the validation process of the solver. In particular, the results of a laminar Poiseuille flow and turbulent round jet LES simulations are presented. The first has been simulated to test the parallelisation of the code and its performance, while the second to assess the turbulence LES model and lead a grid convergence analysis for the successive simulations.

Chapter 6 is a review of the slaked lime discharging numerical simulations. The study of the data of velocity, pressure, $Ca(OH)_2$ concentration and seawater pH is aimed at comparing different layouts of calcium hydroxide release into the wake of a ship, focusing on their benefits and side effects especially for the marine ecosystem. The first simulations provide a comparison of different operational regime for the ship propeller and discharging mass flow rate of slaked lime. The final simulation completes the previous study, with the addition of the ship hull, modelled as a bluff body, in the computational domain. This allows to have a configuration closer to the reality.

The thesis is ended with a concluding discussion on the results obtained and future remarks for the work development of the research.

2. Ocean Liming

The scope of this chapter is to give an overview on ocean chemistry dynamics and Ocean Liming strategy. Specifically, it is given emphasis on Ocean Liming implications on ocean carbon cycle, with the addition of a preview of OL limits of application and its cost analysis. The first Section gives an overview on ocean chemistry, showing all the substances involved in chemical reactions. The second one is an in-depth analysis of all OL aspects, going through the feasibility of production and transportation, the limits of application and a brief cost analysis.

2.1 Ocean Carbon Cycle

The presence of CO_2 in the Earth's atmosphere is strictly related to the process of Carbon Cycle, which is characterized by the interaction between atmosphere, ground rocks and oceans. This phenomenon mainly consists in three processes: weathering of silicate and carbon rocks, reaction with carbonate sediments and alkalinity of ocean. A scheme of the ocean carbon cycle is presented in figure 2.1.

2.1.1 Weathering of Silicate Rocks

The chemical weathering is defined as a set of reactions that breaks down silicate minerals. These processes are really slow due to kinetic limitations, hence the total removal of carbon hydroxide from the atmosphere by weathering reactions is estimated as ≈ 0.25 Gt C yr^{-1}. Actually, such value could be lower due to chemical constraints. Furthermore, this removal process is balanced by volcanic emissions of CO_2, that together with silicate weathering flux constitute only a very small part of the total carbon mass in the Earth's system. An imbalance between weathering and volcanic fluxes must occur for very long time periods to cause a significant change in climate and carbon system. Therefore, they poorly contribute to the atmosphere removal of CO_2.

2.1.2 Ocean Alkalinity

Alkalinity is the capacity of a solution to neutralize acid. Because of its high alkalinity and its large volume on Earth's surface, seawater is the largest inorganic C reservoir on Earth. The

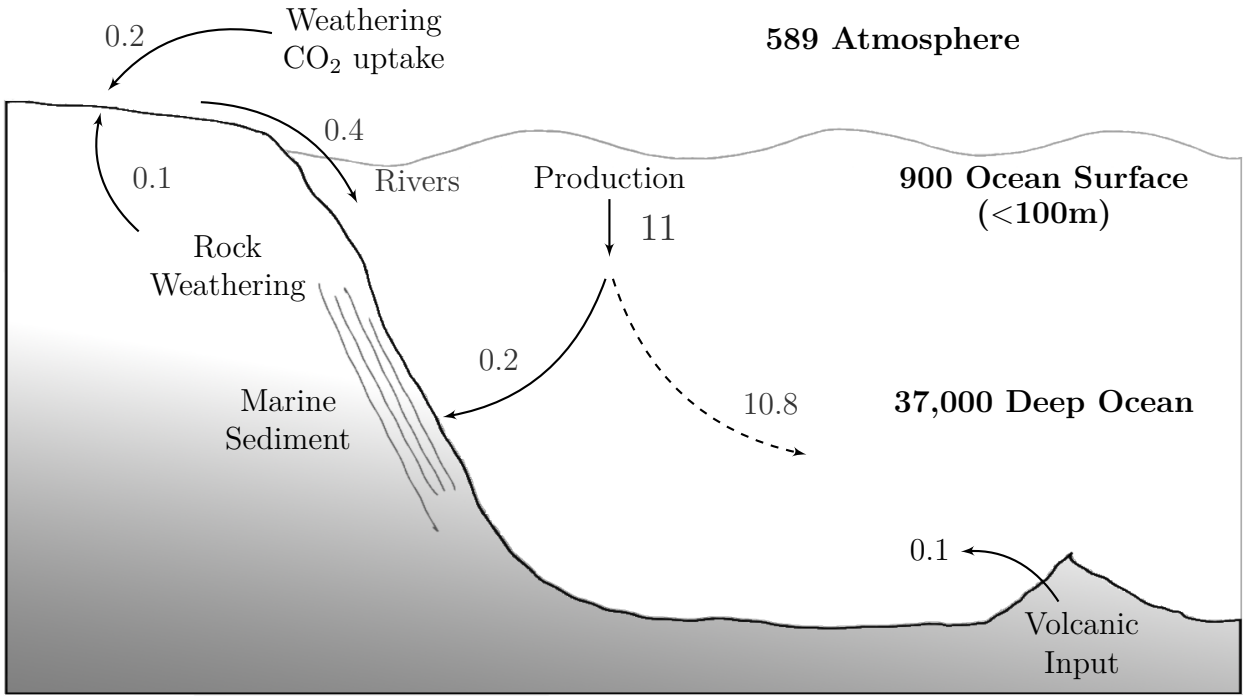

Figure 2.1: A scheme of the global ocean carbon cycle. Arrows show fluxes of Gt C yr^{-1}. Reworked from Renforth and Henderson [2017] p. 643

Large amount of C storage is given by the dissolution of bicarbonate (HCO_3^-) and carbonate (CO_3^{2-}) ions. Indeed, a partial pressure difference of CO_2, between water and atmosphere, causes the dissolution of carbon dioxide into the ocean. Part of it reacts with water to form the carbonic acid (Renforth and Henderson [2017]).

$$CO_2 + H_2O \longleftrightarrow H_2CO_3 \tag{2.1}$$

Since CO_2 is more concentrated in water than H_2CO_3, it is convenient to refer to the group of this two substances in the term $CO_{2(aq)}$. Finally, the production of bicarbonate and carbonate ions derives from these chemical processes:

$$CO_{2(aq)} + H_2O \longleftrightarrow HCO_3^- + H^+ \tag{2.2}$$

$$HCO_3^- \longleftrightarrow CO_3^{2-} + H^+ \tag{2.3}$$

The weathering removes H^+ from the solution, causing an imbalance in equations (2.2) and

(2.3). Consequently, in order to compensate, $CO_{2(aq)}$ is reduced to produce HCO_3^- and H^- and, at the same time, HCO_3^- is converted to CO_3^{2-}. For maintaining the equilibrium more CO_2 is dissolved in the liquid from the gas phase.

An important role in the active ocean alkalinity cycle is assumed by Ca^{2+}, particularly in the processes of formation and dissolution of $CaCO_3$ (also called calcite or aragonite). The calcite is supersaturated in the ocean surface, but its inorganic precipitation is inhibited by the presence of other elements. Nevertheless, some animals and plant species have the ability to precipitate $CaCO_3$, as calcite or aragonite, with a removal of Ca^{2+} from the ocean surface. This removal causes a reduction of the surface ocean alkalinity, leading a transfer of CO_2 from the ocean to the atmosphere. On the other hand, in the deep water there is a remineralization of organic C, with a decrease of pH seawater, which is compensated by the dissolution of $CaCO_3$ that causes an increase of alkalinity (the so called "carbonate compensate", Ridgwell and Zeebe [2005]). Thanks to the upwelling of higher alkalinity deep water, the surface seawater is affected by a variation of about 5% in alkalinity. Hence, dissolution and precipitation of $CaCO_3$ have a key role in alkalinity changes.

Imbalances in alkalinity fluxes can affect the capacity of the ocean to store C, which is thought to play an important role in controlling climate change. For this reason, the knowledge of these natural processes led to the development of artificial ways to control ocean chemistry.

2.1.3 The Coupling of Weathering and Ocean Alkalinity

There are two ways to remove CO_2 from the atmosphere, that are related to weathering of silicates. The released cations can reprecipitate as minerals on land (for example $CaCO_3$). On the contrary, they can be transported to the ocean promoting the production of HCO_3^- and CO_3^{2-} and the consequent uptake of CO_2 from the atmosphere. The products of silicate weathering can potentially impact more on the removal of CO_2, if they reach ocean. Indeed, the input of divalent charge ions, such as Ca^{2+}, is compensated by the formation of two ions containing C, absorbing two CO_2 molecules. Actually, the uptake is 1.4 to 1.7 molecules because of the presence of CO_3^{2-}. On the other hand, if carbonate minerals do not reach ocean there is no net effect on CO_2.

2.2 Ocean Liming Process Assessment

There are various strategies developed for preventing global climate changes, in particular global warming. In 1995 Kheshgi was the first to come up with the idea of sequestering anthropogenic carbon dioxide adding alkalinity to seawater. Such approach is called "Ocean Liming" or "Ocean Alkalinization" and allows not only to prevent global warming, but also to counteract ocean acidification and strengthen reef calcification. The process consists in discharging $Ca(OH)_2$ (Portlandite, slaked lime or hydrated lime) in seawater, which reaction

with water and carbon dioxide produces Ca^{2+} and HCO_3^- ions. The latter further breaks up into CO_3^{2-} ions, fundamental elements for the Ocean Alkalinity cycle.

$$Ca(OH)_2 + 2CO_2 + H_2O \longleftrightarrow Ca^{2+} + 2HCO_3^- \tag{2.4}$$

In the next paragraphs the practical aspects and the feasibility of the proposal will be discussed in detail.

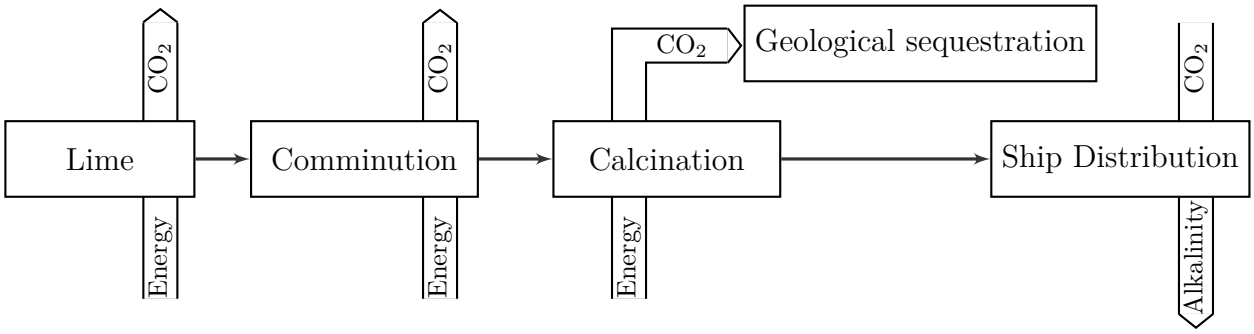

Figure 2.2: Scheme of the production of hydrated lime. Reworked from Renforth et al. [2013] p. 443

2.2.1 Hydrated Lime Production

For the ocean alkalinization two are the substances proposed by Kheshgi. The soda ash Na_2CO_3, from which $Mg(OH)_2$ can be produced, already present in nature, but not in a sufficient quantity to have a significant impact on CO_2 sequestration and the limestone $CaCO_3$, from which the slaked lime $Ca(OH)_2$ can be obtained. The latter, differently from the soda ash, is widely distributed all over the globe. Moreover, Renforth et al. [2013] investigated the possibility of using forsterite-rich olivine (Mg_2SiO_4) for Ocean Liming process. Although it minimizes the limits on plant location and decreases the overall costs by $\approx 60 \div 80\%$, $Mg(OH)_2$ needs to be significantly pure in order to avoid biological impact (because of the possible presence of Fe and Si) and its effect on ocean alkalinity has not been studied yet. Therefore, slaked lime is the substance primarily considered in this thesis work. The whole process described below, from extraction till ocean distribution, is schematized in fig. 2.2.

2.2.1.1 Extraction and Comminution

For the production of lime it is necessary to find an appropriate deposit of limestone. Thanks to its wide distribution on Earth, the extraction of this raw material will never be a limiting factor for Ocean Liming, indeed limestone deposits cover about 10% of Earth land surface. Since the dissolution dynamics of lime particles primarily depends on size reduction processes, limestone must go through the primary, secondary and tertiary steps of crushing

and, finally, grinding. In particular, assuming of not knowing the exact dissolution rate, a dimension between 50 and 100 μm is necessary for particle diameter. The energy required to obtain 'ground' particles below 1 mm depends on the amount of new surface area created and increases about 8-10% for each 1 m^2/g of surface area. As reported by Renforth et al. [2013] the estimated total energy requirement for extraction and comminution of limestone, till $\approx$ 100 μm, is approximately 90 MJ of electricity and 18 MJ of fuel per tonne of feedstock. This is equivalent to 15 $kg\ CO_2\ t^{-1}$, about three times higher than industrial average.

2.2.1.2 Calcination

The production of lime is one of the oldest industrial processes developed by humankind, though it is focused on manufacturing a substantial smaller quantity with respect to the one requested by OL. It would be necessary to achieve an expected production of millions of tonnes per day, instead of the actual few hundred of tonne per day, in order to significantly reduce atmospheric CO_2. There are two main issues to face in order to upscale the production from the actual knowledge available, satisfy the product requirements and obtain OL feasibility: a proper quality of lime and the capture and storage of almost all the CO_2 produced. Furthermore, calcination is a process that requires a huge amount of energy, which is estimated to be between 2910 and 3492 MJ per tonnes of CaO. In particular, two are the main calcination processes taken into account in the technoeconomic assessment of Renforth et al. [2013]:

- Flash Calcination with Oxy-Fuel: this name derives from the short residence time of the product within the furnace, and it is limited up to a few hundred-micron particle size. In this process upward flow calciners are used, with hot air released at the bottom with the addition of fuel, in order to go for endothermic reactions and expel CO_2 and water. Indeed, such mechanism pushes particles to lose weight and the upward flow allows the heavier particles to reside in the furnace until the volatile components are gone.

- Endex Catalytic Flash Calciner: this technology consists in pressurised steam flash calciner, in which limestone is firstly crushed in particles of 125 μm or less. Then such particles are injected in the calciner with the combustion of a natural gas and air. The main advantage of this process is a reduction of fuel consumption thanks to the integration of the hydration process in the calciner.

The production of CO_2 by the calcination process is a fundamental parameter for OL feasibility. Therefore, the isolation of the CO_2 produced is a key issue for the OL project. During calcination, the production of carbon dioxide depends on stone purity and process temperature. A full calcination of 100% pure $CaCO_3$ provides a generation of 440 kg of CO_2. The first solution that could be adopted is the storage in geological reservoir, with the direct injection of flue gas from an oxy-flue system. Two are the alternatives to reduce CO_2 geological storage requirements: solar power, combined with hydrogen, for calcination process allow to

decrease carbon dioxide production from fossil fuel combustion, but also the use of magnesium silicates could reduce the geological storage demand.

2.2.2 Slaked Lime Transportation

The transport of the lime powder to the application sites implies further cost and energy requirements. In particular, an almost global lime distribution on ocean surface could be achieved by using the underutilised space in cargo ships. Indeed, thanks to the sea freight it could be possible to take advantage of ship routes for reaching all the Earth's major oceans (approximately 8 billion tonnes of cargo is transported by 50,000 ships globally). As regards the practical aspects of lime discharge in application sites, the energy required for dispersion from a ship is primarily related to the size of the ship and the method of propulsion. The estimated fuel energy cost associated to ship distribution is approximately 100 MJ t^{-1} of material added to the ocean Renforth et al. [2013], with further 8 MJ t^{-1} for electrical energy and 19 MJ t^{-1} for fuel energy for dockside operations. However, these requirements are small compared to the whole budget. Furthermore, it is worth to underline that applying limestone powder in upwelling regions requires more transport energy, which is function of the lower discharge rate because of the limitations imposed by the poor solubility of limestone.

As stated before, it could be possible to dedicate some of the capacity of existing maritime vessels to the transport of pulverized SL. However, it must consider that the potential of SL discharge depends on many factors, such as fleet size and capacity, length of navigation routes, supply of SL and fraction of capacity usable for transport. In general, ships could be easily adapted to carry equipment for SL loading and discharging. The slaked lime has to be discharged in water as "milk of lime", a slurry form of SL generated by adding pulverized $CaOH_2$ in excess to water. This process has to be done onboard, but it could be possible to use engine cooling system water to not overuse seawater.

The number of active ships circulating detected by the Automatic Identification System (AIS) is used to estimate the average sailing days. The total equivalent hours of navigation per year could be calculated by multiplying the number of active ships by the number of average days of navigation, while the average values are calculated by weighting the values of the different size classes (considering the number of annual days at sea). In terms of deadweight tonnage, the 92% of total active capacity is associated with two ship categories: cargo (bulk carrier, container, general cargo) and tanker (chemical tanker, oil tanker). Bulk carriers and container ships represent 53% of the total commercial global fleet in terms of total active tonnage, even if they are only 17% of the total number of ships. These two types of vessels, more than any other, are directly suitable for SL discharge both for ship structure and logistic reasons.

Vessel type	**Total fleet size**	**Average days of navigation**	**Average speed**	**Distance covered**	**Average active capacity**	**Total active capacity**	
	days/year	days/year	km/h	Mkm/year	dwt	10^6 dwt	%
Bulk Carrier	10397	181	21.4	862	75752	703	40%
Container	5132	218	27.4	688	45417	220	13%
Cargo	32015	184	21.7	2224	43499	1025	59%
Tanker	12330	177	20.5	796	62584	585	33%
Other	63,404	142	16.22	5903	5768	130	8%
TOTAL	107749	170	19.2	4383	29711	1747	100%

Table 2.1: Ships data for vessel categories, IMO 2014. Reworked from Caserini et al. [2021] p. 4

Having assessed which type of vessels could be used, it is important to estimate the length of navigation at sea of them. A longer route of navigation at sea allows to either maximize or minimize the discharge rate of a fixed amount of SL. Container ships and bulk carriers have respectively an average of 218 and 181 days of navigation, a considerable value, and globally cover about 70% of the total distance of vessels. As stated by Renforth et al. [2013] about bulk carriers, the discharge time of a 300,000 DWT bulk carrier is approximately 3.5 days, with an additional day of steaming for discharging in open ocean and return to port and 6 days for loading, for a total amount of 11 days. Based on these values, 101 dedicated ships should guarantee a delivery of 1 $Gt\ \mathrm{yr}^{-1}$.

The convenience of transporting SL depends on the revenue obtainable from the spreading activity, in place of the one obtained from the transportation of other commodities (with which is obviously in competition). We know from Caserini et al. [2021] that around 10-20% of the net cargo capacity of container ships is not used and could be converted in space for carrying SL without affecting operations and performances. For this reason, ships do not need to be significantly modified to respect requirements for SL transportation, hence with few consequences on costs. Concerning the modifications of vessels, it would be limited to implement dedicated SL loading facilities in various calling ports. As previously reported, it would be easier to transport SL in pulverized form, later prepared to be discharged adding $Ca(OH)_2$ in excess to water. Due to poor calcium hydroxide solubility, it is necessary to use this slurry of water and calcium hydroxide (milk of lime) instead of just limewater. Limiting the amount of water speeds up the discharge and lowers the energy and water consumption. A good trade-off between water usage and good movement of the slurry is to use 2% of water dilution, which is equivalent to a concentration of 86.5 g/l of SL, or 11.6 litres per kilogram of SL.

The frequency of SL reload has a key role in reaching the required quantity for the discharge along the route. If vessels are loaded with SL only at starting and final ports the discharge rate

would depend only on the tonnage of the ship and route length. On the other hand, if ships are loaded during a potential intermediate stop the discharge potential would significantly increase. In order to estimate an average number of intermediate stops for bulk carriers and container ships, data on routes lengths and main routes are taken from different platforms: Marinetraffic (2019) and Vesselfinder (2019) for bulk carriers, UNCTAD (2019a) and Marinetraffic (2019) for container ships. In particular, UNCTAD 2019 handbook is used to identify main routes, while Marinetraffic allows to obtain length of routes. This led to an average of one intermediate stop for bulk containers and four for container ships. The regular time for other commodities loading operations on vessels could be a limiting factor for SL reload, it could be necessary some extra tonne for filling the portion of ships' hold reserved for the SL storing.

2.2.3 Side effects of OL

The requirement of high application rates of slaked lime for decades, in order to have significant results in reducing ocean acidification and atmospheric CO_2 , could inevitably have a substantial impact on regional ocean biology. Studying the local impact of regional alkalinity addition rate is important to identify application limits, minimizing environmental impact. Although there is not a wide and precise knowledge of the consequences of increased alkalinity on marine ecosystem, some studies were made about the subject over the past years that could help to better understand the argument. Henderson et al. [2008] stated that a significant rise in ocean alkalinity could provide a competitive advantage for calcifying organisms. Moreover, the input of silicates may grow up the ocean fertilization, with the risk of increasing the production of greenhouse gasses, such as N_2O and CH_4 (Fuhrman and Capone [1991]) and a lower dissolution of oxygen. Concerning the vegetal ocean organisms, phytoplankton is the more affected by alkalinity addition, because of the photosynthesis inhibition. Consequently, the alteration of phytoplankton's function and structure has important implications for the whole marine ecosystem. Many studies highlight also damages on marine animal species. Scott et al. [2005] discovered that the exposure to high alkalinity water (pH= 9.5) causes blood alkalosis in *perca fluviatilis* (perch) due to the restraints on sodium uptake and ammonia expulsion. From a toxicologic study, made by Locke et al. [2009], emerged that an elevated concentration of $Ca(OH)_2$ rises the mortality of *gasterosteus aculeatus* (a coastal fish) and *crangon septemspinosa* (a common shrimp). Also Cripps et al. [2013] analysed the impact of $Ca(OH)_2$ addition on marine animals, specifically on *carcinus maenas* (crab species) , pointing out the possibility of respiratory alkalosis in this species. Finally, Byrne and Dietz [1997] noted that bivalves could be the most sensitive to these environmental changes because the lack of control on their blood pH. In conclusion, a long exposure to an excess of alkalinity may have a chronic impact on flora and fauna, even if they have developed renal compensation in order to regulate the alkalinity in their organism.

2.2.4 Fluidynamics of Slaked Lime

Many are the studies about the behaviour of slaked lime in the wake of a ship, with different methodologies and fluidynamic models.

As regards dissolution rates, the simplified model adapted by the International Maritime Organization in 1975 has some limitations. Indeed, further studies [Byrne 1988; Chou 1996] demonstrated that this approach underestimates the dispersal rate up to 10 times. Therefore, in this work Tannenberger formulation is adopted [Tannenberger et al. 2009]. Such theory uses the Nernst-Haskell equation for diffusivity computation.

$$D = \frac{R \cdot T}{F^2} \cdot \left[\frac{\frac{1}{k^+} + \frac{1}{k^-}}{\frac{1}{\lambda^\circ_+} + \frac{1}{\lambda^\circ_-}} \right]$$

Where F represent Faraday constant, R the universal gas constant, k the ion valence and λ the limiting ionic conductance. As can be noted by the formula, the dilution factor is a function of temperature. However, for simplicity and since the present thesis work is focused on ocean surface, neglecting the effect of Ocean Liming on deep ocean, it is assumed a constant temperature, with a value of 20°C (293 K).

Hence, the following values of ionic conductance and diffusivity factor are obtained:

$$\lambda^\circ(T) = \frac{T}{334 \cdot \eta} \cdot \lambda^\circ(298K)$$

$$\lambda^\circ_{Ca^{2+}} = 48.33 \ \frac{A \cdot cm^2}{V \cdot eq}$$

$$D = 6.32 \cdot 10^{-10} \frac{m^2}{s}$$

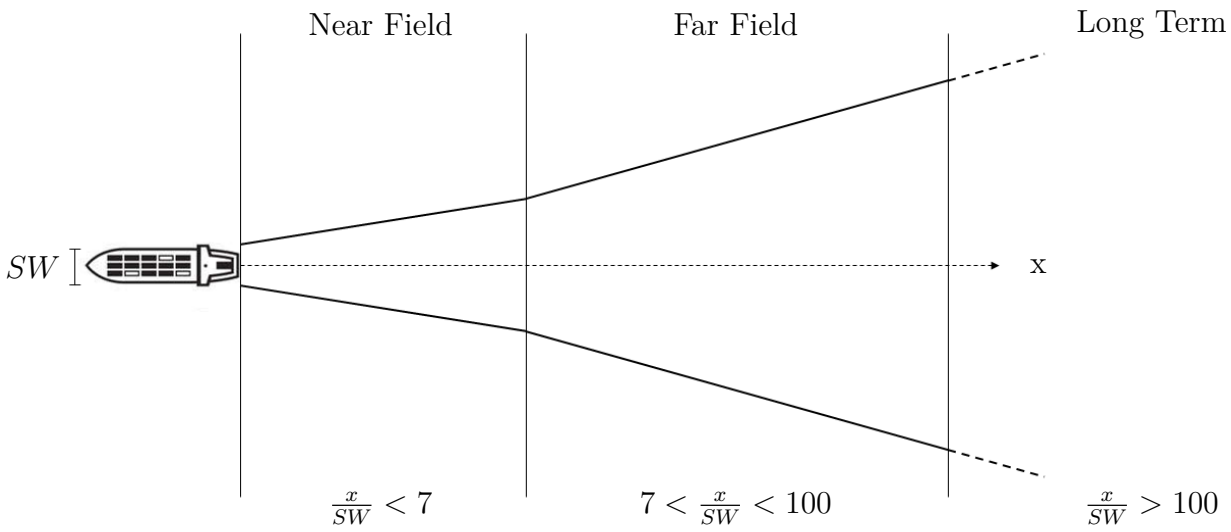

Figure 2.3: Wake of a ship: a fluidynamic point of view. Reworked from Chou [1996] p. 150

In order to better understand OL feasibility, besides a deep insight on the interaction between slaked lime and seawater from a chemical point of view, it is necessary to investigate such interaction from a fluidynamic perspective, analysing the seawater behaviour in the wake of a ship. In his work, Chou [1996] identified three regions in the ship wake with the ratio between the distance from the ship and the ship's width as parameter (x/SW), each one with a different flow behaviour:

- Long Term Region ($x/SW > 100$): the main influence on the flow motion is given by ambient turbulence and ocean currents. Here the dilution process of lime is not affected by the flow.
- Far Wake Region ($7 < x/SW < 100$): this region is independent on geometry and configuration of the problem, with a similarity of the transversal mean velocity profiles at different distances from the ship.
- Near Wake Region ($x/SW < 7$): differently from the previous two, in such region there is not a universal solution for the flow. There is a strong dependence on the ship geometry and the velocity induced by the propeller. Regarding the slaked lime, lower dilution rate and higher concentration are expected. In particular for this region it was developed by Kundu et al. [2011] a jet model for the concentration of a non-reactive substance, discharged in the wake of a ship:

$$C_{nr}(s) = 5C_0 \cdot \frac{d_0}{s} \qquad for \;\; s \geq 6d_0 \tag{2.5}$$

- C_{nr}: concentration of a non-reactive substance
- C_0: initial concentration
- d_0: discharge orifice diameter
- s: curvilinear abscissa along streamlines from injection location

It is worth to notice that in the present thesis, for sake of simplicity, the curvilinear abscissa is substituted by the axial coordinate x.

Given the assessments previously made, this thesis work is based on a Large Eddy Simulation of slaked lime in the near wake region, with the implementation of a reactive model. This approach allows to have a complete point view of the slaked lime behaviour in that region, which is more interesting to be investigated.

2.2.5 Cost Analysis

As defined in the previous paragraphs for a net sequestration of 1 $GtCO_2$ from the atmosphere 0.9-1.3 Gt of lime is required. Hence, the cost analysis made by Renforth et al. [2013] is based on this amount of slaked lime production and uses the International Energy Agency (IEA) as main reference.

Operation	*M US$*
Extraction	
Primary Crushing	3.4
Secondary Grinding	25
Raw meal silo	4.7
Stacker	2.5
Calcination	
Calciner	7.8
Fluid bed cooler	17.1
Storage silo	10.6
Electrostatic precipitator	2.1
Hydrator	18.2
Classifier	3.53
Natural Gas fuel system	1.13
Conveyor	1.8
Mill	5.9
Gas purification	
Air separation unit	11.21
Compression and purification	7.5
Ancillary	
Design and engineering	71.9
Construction	69.1
External contractor services	26.8
Contingency	16.2
Fees	8.5
Owner costs	21.2
Other costs	21.2
Total	**366**

Table 2.2: Capital costs of slaked lime production Renforth et al. [2013] p. 446

Below a resume of the highlights of this economic evaluation:

- Slaked Lime production: As regards capital cost, approximately, a budget of 120 million of euros is indicated for a cement plant in Northern Europe. This cost item could vary in a range of $\approx\pm 25$. On the other hand, the operating costs mainly depend on fuel cost, which is a very volatile variable because of political decisions (for example taxes) and market commercial forces. Furthermore, cost of CO_2 capture from calcination process has to be taken into account. In particular the compression of the gas plays the major role, with a range of cost between $US\$$ 0.2-30 tCO_2^{-1}. For an oxy-fuel system the overall cost of slaked lime production is about $US\$$ 87 $tCa(OH)_2^{-1}$.

- Distribution: In Renforth et al. [2013] study, shipping and energy distribution are included respectively with a cost of $US\$$ 177000 per day ($US\$$ 3.1 $t(lime)^{-1}$) and $US\$$ 1.5 $t(lime)^{-1}$

	Oxy fuel flash calciner	**Endex CFC**	**Solar calciner**
Calciner/Extraction	41.3	35.8	101.4
Limestone	6.8	5.7	6.1
Energy	46.5	28.8	11.4
Water	0.3	0.3	0.3
Distribution (port)	6.8	5.7	6.1
Distribution (vessel hire)	3.9	3.3	3.5
Geological sequestration	4.9	4.7	3.4
Total operational	110.5	84.1	132.1
Discounted capital	15.1	15.4	26.6
Total cost	**126.6**	**99.5**	**158.7**

Table 2.3: OL cost summary in $US\$\ tCO_2^{-1}$ Renforth et al. [2013] p. 447

In summary, for a project of 1 million tonnes of hydrated lime per year the estimated capital cost is about $US\$\ 250\ M$, that can vary depending on calcination type process and can be expressed also as $US\$\ 12\ t^{-1}$ of slaked lime produced. On the contrary the overall operational cost can be divided in energy costs (37%) and fixed costs (33%), with a total amount of $US\$126\ tCO_2^{-1}$ for an oxy-fuel flash calciner, which is the most common used.

2.2.5.1 Cost Comparison with other Technologies

Although OL has the uncertainty of CO_2 geological storage and impact on ocean environment, its energy and economic costs are generally less than other technologies that capture CO_2 from the atmosphere. Such concept is resumed in the table below.

Technology	$US\$\ tCO_2^{-1}$
OL (Oxy-fuel flash calciner: limestone)	126
OL (Endex CFC: limestone)	100
OL (Solar calciner: limestone)	159
Direct Air Capture (cont, $NaOH$ - $CaCO_3$)	780
Direct Air Capture (anionic resin)	220
Direct Air Capture (amine)	180
Direct Air Capture (contact, spray)	150
Electrochemical Weathering ($CaCO_3$)	<100

Table 2.4: Cost comparison between OL and other technologies Renforth et al. [2013] p. 448

3. Physical Model

The chapter presents a review of the mathematical and physical theoretical models on which the thesis work is based. In the first part the focus is on the description of the governing equations solved in fluidynamic simulations reported in the subsequent Chapters 5 and 6, while in the second part it is given attention to the solving approach of governing equations and the mathematical model and theory for the representation of the propeller of a ship.

3.1 Governing Equations

This chapter is devoted to present the equations solved in the simulations of this thesis work. Specifically, the focus is on the dynamic evolution in time and space of the water flow (pressure and velocity), the concentration and particle radius of slaked lime injected and pH of the water.

3.1.1 Navier-Stokes Equations

The interest of this study is the evolution of an incompressible Newtonian fluid, in particular water. In this paragraph the constitutive equations are expressed in the eulerian, pressure-velocity formulation, in physical space with a Cartesian coordinate system $\boldsymbol{x} = [x_1, x_2, x_3]$.

- Continuity Equation:

$$\frac{\partial u_i}{\partial x_i} = 0 \tag{3.1}$$

- Momentum Equation:

$$\frac{\partial u_i}{\partial t} + \frac{\partial}{\partial x_i}(u_i u_j) = -\frac{\partial p}{\partial x_i} + \nu \frac{\partial}{\partial x_i}\left(\frac{\partial u_i}{\partial x_j} + \frac{\partial u_j}{\partial x_i}\right) \tag{3.2}$$

Where $p = P/\rho$ is the isotropic term of the stress tensor, ν is the constant kinematic viscosity (assumed as uniform) and $\boldsymbol{u} = [u_1, u_2, u_3]$ is the velocity vector. However, in CFD the non-dimensionalised NS equations are commonly solved exploiting the similarity principle through

the Reynolds number $Re = U_{ref}L/\nu$ as the only similarity variable. The adimensionalisation process requires the definition of the non-dimensionalised flow variables:

$$u_i^* = \frac{u_i}{U_{ref}} \qquad t^* = \frac{tL}{U_{ref}} \qquad p^* = \frac{p}{\rho U_{ref}^2} \qquad \nabla^* = \frac{\nabla}{L} \qquad x_i^* = \frac{x_i}{L} \quad , \tag{3.3}$$

where U_{ref} and L are respectively the reference velocity and the reference length of the flow. Substituting the relations (3.3) in the equations (3.1) and (3.2) non-dimensional NS equations are obtained:

$$\frac{\partial u_i^*}{\partial x_i^*} = 0 \qquad , \tag{3.4}$$

$$\frac{\partial u_i^*}{\partial t^*} + \frac{\partial}{\partial x_i^*}(u_i^* u_j^*) = -\frac{\partial p^*}{\partial x_i^*} + \frac{1}{Re}\frac{\partial}{\partial x_i^*}\left(\frac{\partial u_i^*}{\partial x_j^*} + \frac{\partial u_j^*}{\partial x_i^*}\right) \tag{3.5}$$

.

3.1.2 Passive Scalar Dynamics Equations

The physical system of the simulations provides the injection of hydrated lime in water. Since we consider a mixture with high dilution, slaked lime does not affect the pressure and velocity dynamics of the fluid, hence its concentration and particle radius are treated as passive scalar. Therefore, the scalar dynamics is only strictly related to the fluid velocity field and there is no feedback of scalar equation in the momentum equation. The dynamic equation for the concentration of $Ca(OH)_2$ is the following:

$$\frac{\partial C}{\partial t} + \nabla \cdot (\boldsymbol{u}C) = D\nabla^2 C + S_C \tag{3.6}$$

It assumed that the molecular diffusivity D of calcium ions, which is a function of temperature, is constant (with a value of $6.32 \cdot 10^{-10}$ m^2/s, referred to 20°C) because of the hypothesis of constant surface ocean temperature. The source term S_C provides the contribution of the chemical reaction between slaked lime and water. A fundamental tool for the development of this source term is the work of Tannenberger and Klein [2009], in which the calcium hydroxide particles dissolution in water is investigated in detail. The mass flow formulation from spherical particle to water has been taken into account:

$$-\alpha \cdot \dot{m} = \frac{d}{dt}(\frac{4}{3}\pi\rho_p r_p^3) \tag{3.7}$$

$$S_C = \frac{\dot{m}}{\frac{4}{3}\pi\rho_p r_p^3} C \tag{3.8}$$

In analogy with Section 3.1.1, the normalized $Ca(OH)_2$ concentration and r_p can be introduced:

$$C^* = \frac{C}{C_0} \qquad r_p^* = \frac{r_p}{r_{p0}} \qquad S_C^* = \frac{S_C L}{U_0 r_{p0}} \qquad S_{r_p}^* = \frac{S_{r_p} L}{U_0 r_{p0}} \quad , \tag{3.9}$$

- C_0: initial concentration
- r_{p0}: initial particle radius [1] .

The key factor of the calcium hydroxide particle dissolution is the Peclet number, defined as:

$$Pe = \frac{U d_p}{D} \quad , \tag{3.10}$$

where U is the flow velocity, d_p is the particle diameter and D the molecular diffusivity. Given the flow condition simulated in this work, the high Peclet limit has been considered. Furthermore, slaked lime particles are assumed to be solid and spherical, neglecting the effects of porosity that are irrelevant according to the Tannenberger and Klein [2009] study. In order to fully take into account the chemical reaction that occurs between slaked lime and water, it is necessary to introduce a second equation that models the dynamics of the $Ca(OH)_2$ particle radius:

$$\frac{\partial r_p}{\partial t} + \nabla \cdot (\boldsymbol{u} r_p) = S_{r_p} \tag{3.11}$$

The source term S_{r_p} is defined by Tannenberger and Klein [2009] as:

$$S_{r_p} = -0.634 \cdot \Phi_0 \cdot D^{\frac{2}{3}} \cdot B^{\frac{1}{3}} \tag{3.12}$$

Where the diffusion potential Φ_0 and B are constants, respectively defined as:

$$\Phi_0 = \frac{\alpha \cdot C_0}{\rho_p} \quad ; \qquad B = 2.455 \cdot 10^6 \ \frac{1}{m \cdot s}$$

- C_0: initial $Ca(OH)_2$ concentration
- $\alpha = 0.54$: empirical constant
- ρ_p : density of slaked lime particle

In the present work a diffusion potential of $\Phi_0 = 2.09 \cdot 10^{-2}$ has been used, differently from the range of values tested in Caserini et al. [2021]. Such parameter influences the kinematics of slaked lime reaction with water, however there is no evidence on which is the correct value to be

[1] All constant values are given in the tabular 6.1

adopted. In conclusion the following non-dimensional equations, for passive scalars dynamics, are obtained:

$$\frac{\partial C^*}{\partial t^*} + \nabla^* \cdot (\boldsymbol{u}^* C^*) = \frac{D}{ReSc} \nabla^{*2} C^* + S_C^* \qquad , \tag{3.13}$$

$$\frac{\partial r_p^*}{\partial t^*} + \nabla^* \cdot (\boldsymbol{u}^* r_p^*) = S_{r_p}^* \tag{3.14}$$

The adimensionalisation of the diffusion term of the $Ca(OH)_2$ concentration equation sees the introduction of a second adimensional number, the so-called Schmidt number $Sc = \eta/(\rho D)$, which is the ratio between the kinematic diffusivity and the diffusion term for mass transfer. It is worth to highlight that in the subsequent chapters only the non-dimensional equations are taken into account, but for sake of simplicity, the asterisk as apex of the flow variables is omitted.

3.1.3 pH Evolution Equation

In order to constrain computational time an algebraic equation has been developed, instead of the convection diffusion equation, for the water pH dynamics. In particular, the simplified chemical model adopted is based on a parabolic relationship between $Ca(OH)_2$ input and pH variation and was assessed through the use of PHREEQC software, implemented by the U.S. Geological Survey (mentioned in Caserini et al. [2021]). In particular, the formula (3.16) has been obtained with a polynomial interpolation of pH increment from PHREEQC software, in function of $Ca(OH)_2$ input, for different values of local pH. Analogously, the coefficients $a(t)$, $b(t)$ and $c(t)$ are computed with formulas in (3.17) derived from a polynomial fitting of the parabolas (with the shape of (3.16)) for different values of local pH. Moreover, it is worth noticing that this approximated model was born as a monodimensional model, considering different pH steps along streamlines. However, in the present work the same model has been used in a three-dimensional way, considering the pH steps as a time evolution (for a single computational cell) instead of a spatial evolution.

In the pH computation the variation in time increment between a non-reactive substance and $Ca(OH)_2$ concentrations plays an important role. Differently from all the other governing equations solved ((3.4),(3.5),(3.13),(3.14)), equation (3.15) requires the use of non-normalized concentration.

$$I(t) = (C_{nr}(t) - C(t)) - (C_{nr}(t - \Delta t) - C(t - \Delta t)) \tag{3.15}$$

- $I(t)$: dissolved $Ca(OH)_2$
- C_{nr}: concentration of a non-reactive substance
- C: concentration of solid $Ca(OH)_2$

The concentration C_{nr} is computed solving an equation similar to (3.13), neglecting the source term S_C^*; this is equivalent to neglect the contribution of the reaction between calcium hydroxide and seawater. The increased pH is expressed with the following parabolic relationship:

$$\Delta pH(t) = a(t) \cdot I^2(t) + b(t) \cdot I(t) + c(t) \tag{3.16}$$

$$\begin{cases} a(t) = 0.000471 \cdot pH^2(t - \Delta t) + 0.00864 \cdot pH(t - \Delta t) - 0.0397 \\ b(t) = 0.0218 \cdot pH^2(t - \Delta t) - 0.401 \cdot pH(t - \Delta t) + 1.86 \\ c(t) = 0.0158 \cdot pH^2(t - \Delta t) - 0.294 \cdot pH(t - \Delta t) + 1.36 \end{cases} \tag{3.17}$$

The final formula of pH in a time step also considers the dilution in the wake of the ship:

$$pH(t) = -\log_{10} \frac{10^{-(pH(t-\Delta t)+\Delta pH(t))} + 10^{-pH_0 \cdot D(t)}}{1 + D(t)} \tag{3.18}$$

- pH_0: initial seawater pH, equal to 8.12 (Caserini et al. [2021])
- D(t): dilution factor

$$D(t) = \frac{C_{nr}(t - \Delta t)}{C_{nr}(t)} - 1$$

3.2 Large Eddy Simulation Approach

Computational Fluidynamics (CFD) is a very important tool in engineering applications, developed starting from the second half of the 20^{th} century, that consists in the numerical solution of fluid motion equations. The main objective is to predict flow behaviour and physical parameters that depend on the fluid, in order to reduce costs and time of a project. In a CFD simulation fundamental is the accuracy of its output flow data, hence the physical model and spatial-time resolution must be in compliance with the problem to investigate. In a turbulent flow the range of space-time scales is enlarged by the increasing flow Reynolds number (Re), demanding a sharper resolution and consequently rising computational time.

As regards the flow scale separation problem, three are the main approaches developed in CFD: RANS, DNS and LES.
The RANS (Reynolds-Averaged-Navier-Stokes) approach is based on the numerical solution of steady Navier-Stokes equations, with the application of an ensemble average filter to the exact solution. Therefore, the statistical average of the solution is directly computed and all the turbulent scales are modelled with the application of various turbulence models. This method

allows to drastically reduce computational effort, but with a poor representation of turbulence structures interaction. At the opposite side Direct Numerical Simulation (DNS) technique solves all space-time scales of the flow, with the direct numerical solution of unsteady NS equations. However, the demanding of computational resources is very high and worsen with increasing Re. Indeed, from Kolmogorov's theory, in a statistically homogeneous and isotropic turbulence, the ratio between the most energetic scale L and the dissipative scale η has the following formulation:

$$\frac{L}{\eta} = O(Re^{\frac{3}{4}}) \tag{3.19}$$

Therefore, higher is the Reynolds number, smaller will be the scale size to be solved.

In LES(Large Eddy Simulation) approach the largest turbulent scales of motion in space, that contain the major part of energy and anisotropy, are directly solved, while the smallest scales, which have a universal behaviour, are modelled. Indeed, at high Re the scale separation increases (3.19) and throughout the energy cascade process there is a memory loss of the large eddies, with the return to local isotropy (Pope [2000]). Hence, from a computational point of view, it is an intermediate solution between RANS and DNS, because it captures the large scales motions with more accuracy than RANS and requires a coarser mesh grid to represent the smallest structures, as DNS. For all these reasons, LES technique is the approach adopted in all the simulations of this work. The LES method of application can be declared in four step:

- Decomposition: split of the exact solution into large and small-scale components
- Filtering: Application of a filter, in physical or spectral domain, on NS equations
- Closure: Application of a mathematical model for subgrid stresses
- Numerical Solution: computation of filtered NS equations

3.2.1 Filtering and Closure Operations

The filtering operation in LES allows to identify which size of scales are resolved. It consists in the application of a scale high-pass filter, that in physical domain corresponds to a convolution product with the exact solution. For sake of simplicity, in this Section it is presented the discussion on a homogeneous and isotropic filter (for further details of an anisotropic non-homogeneous filtering consult Sagaut [2006]).

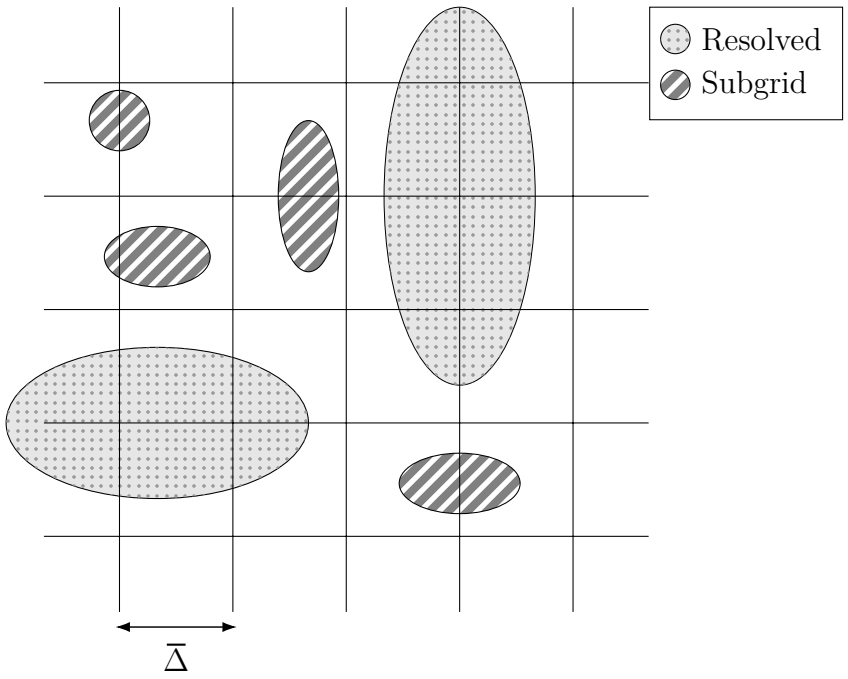

Figure 3.1: Simple scheme of the filtering operation: the cutoff wave number k_c is directly computed from the cutoff length $\overline{\Delta}$. Structures bigger than $\overline{\Delta}$ are directly resolved, the ones smaller are computed with a subgrid model. Reworked from Sagaut [2006] p. 11

The exact solution $\phi(\boldsymbol{x}$,t) can be decomposed as:

$$\phi(\boldsymbol{x},t) = \overline{\phi}(\boldsymbol{x},t) + \phi'(\boldsymbol{x},t), \tag{3.20}$$

where $\overline{\phi}(\boldsymbol{x}$,t) represents the filtered solution, with a filter of Kernel G and a cut-off scales in space and time $\overline{\Delta}$ and $\overline{\tau_c}$ [1]:

$$\overline{\phi}\,(\boldsymbol{x},t) = \iint_{-\infty}^{+\infty} \phi\,(\boldsymbol{\xi},t')\,G\,(\boldsymbol{x}-\boldsymbol{\xi},t-t')\;dt'\,d^3\boldsymbol{\xi}, \tag{3.21}$$

and $\phi'(\boldsymbol{x}$,t) corresponds to the residual solution

$$\phi'(\boldsymbol{x},t) = \phi(\boldsymbol{x},t) - \iint_{-\infty}^{+\infty} \phi\,(\boldsymbol{\xi},t')\,G\,(\boldsymbol{x}-\boldsymbol{\xi},t-t')\;dt'\,d^3\boldsymbol{\xi} \tag{3.22}$$

The most common convolution filters, in physical space, used in LES are:

- Box Filter:

$$G(x-\xi) = \begin{cases} \dfrac{1}{\overline{\Delta}} & if\ |x-\xi| \leq \dfrac{\overline{\Delta}}{2} \\ 0 & otherwise \end{cases}, \tag{3.23}$$

which is local in physical space and non-local in spectral space.

- Gaussian Filter:

$$G(x-\xi) = \left(\frac{\gamma}{\pi\overline{\Delta}^2}\right)^{1/2} \exp\left(\frac{-\gamma\,|x-\xi|^2}{\overline{\Delta}^2}\right) \quad , \tag{3.24}$$

a non-local filter both in physical and spectral space.

- Sharp cutoff Filter:

$$G(x-\xi) = \frac{\sin\left(k_c(x-\xi)\right)}{k_c(x-\xi)}, \quad with \;\; k_c = \frac{\pi}{\overline{\Delta}} \quad , \tag{3.25}$$

that inversely from the box filter is local in spectral space and non-local in physical space.

It is worth noticing that the convolution filters are presented, for sake of simplicity, in one-dimensional formulation.

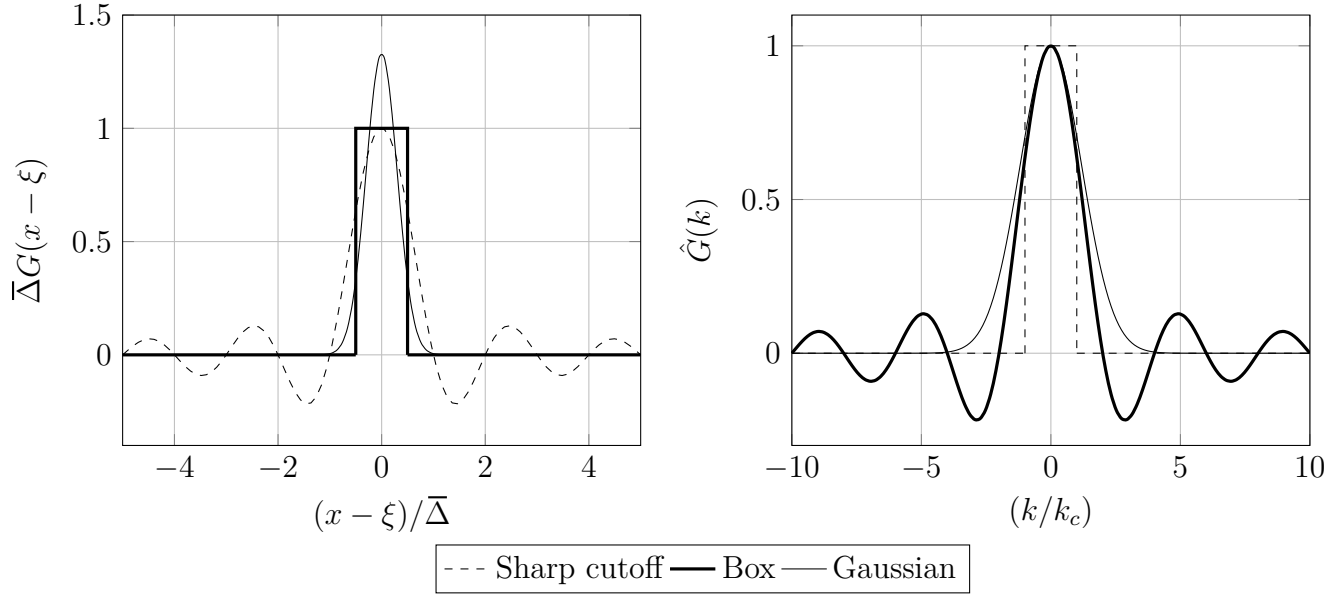

Figure 3.2: Filters convolution Kernel in physical(left) and spectral(right) spaces

[1]Further considerations can be done for a three-dimensional case. Indeed, in many cases the three-dimensional filter could not be homogeneous and isotropic making the bandwidth not so intuitive. In case of an anisotropic filter there are three different dimensions ($\Delta_1\Delta_2\Delta_3$) for the three directions and the bandwidth can be defined as: $\overline{\Delta} = (\Delta_1\Delta_2\Delta_3)^{1/3}$. Furthermore the operator of a non-homogeneous filter does not commute with the derivative operator and could introduce a commutation error.

In all the simulations of this work a non-uniform box filter is implicitly applied by the computational grid, a solution that does not burden the computational time. The application of an homogeneous filter to NS equations leads to the definitions of the filtered NS equations. These are the equations that are solved in numerical simulations. Applying an homogeneous filter to equations (3.1) and (3.2):

$$\frac{\partial \overline{u}_i}{\partial x_i} = 0 \qquad , \tag{3.26}$$

$$\frac{\partial \overline{u}_i}{\partial t} + \frac{\partial}{\partial x_j}(\overline{u_i u_j}) = -\frac{\partial \overline{p}}{\partial x_i} + \frac{1}{Re}\frac{\partial}{\partial x_j}\left(\frac{\partial \overline{u}_i}{\partial x_j} + \frac{\partial \overline{u}_j}{\partial x_i}\right) \qquad , \tag{3.27}$$

where $\overline{u}_i$ is i^{th} component of the filtered velocity and $\overline{p}$ is the filtered pressure. Similarly to equation (3.20), the exact solution of the velocity vector can be split into the filtered velocity $\overline{u}$ and the residual velocity $u\prime$, that takes into account the contribution of the non-resolved smallest scales:

$$u = \overline{u} - u\prime \tag{3.28}$$

Moreover, the filtering operation on NS equations provides the occurrence of the non-linear term $\overline{u_i u_j}$, that entails the closure problem. Indeed equation (3.27) is unclosed because there are no information about the non-linear term and must be expressed as a function of the filtered and residual velocity. Concerning this, the concepts of the residual-stress tensor, residual kinetic energy and anisotropic residual-stress tensor can be introduced:

$$\tau_{ij}^R = \overline{u_i u_j} - \overline{u}_i \overline{u}_j \qquad , \tag{3.29}$$

$$k_r \equiv \frac{1}{2}\tau_{ii}^R \qquad , \tag{3.30}$$

$$\tau_{ij}^r = \tau_{ij}^R - \frac{2}{3}k_r \delta_{ij} \qquad , \tag{3.31}$$

where $\frac{2}{3}k_r\delta_{ij}$ is the isotropic residual stress tensor and could be incorporated into the modified filtered pressure

$$\overline{p} = \overline{p} + \frac{2}{3}k_r\delta_{ij} \tag{3.32}$$

The residual-stress tensor, also defined as Subgrid Scale (SGS) tensor, identifies the interactions between resolved and unresolved scales and many are the decompositions developed over the years by fluidynamics experts. Leonard [1974] designed a triple decomposition of τ_{iJ}^R based on triadic interactions process. In particular, Leonard's theory splits the SGS tensor in the following three terms:

$$\tau_{ij}^R = L_{ij} + C_{ij} + R_{ij} \tag{3.33}$$

- $L_{ij} = \overline{\overline{u}_i \overline{u}_j}$ (Leonard stresses): describe the interaction between two resolved scales that produces a small non-resolved scale.
- $C_{ij} = \overline{\overline{u}_i u\prime_j}$ (Cross stresses): describe the interaction between a non-resolved scale and a resolved scale that generates a third resolved scale
- $R_{ij} = \overline{u\prime_i u\prime_j}$ (Reynold SGS stresses): identifies the interaction between subgrid scales, providing an effect on a resolved mode.

A more sophisticated decomposition of the residual-stress tensor was developed by Germano [1986], through the definition of Germano's identity. Therefore, substituting expressions (3.29), (3.31) and (3.32) in the filtered momentum equation (3.27):

$$\frac{\partial \overline{u}_i}{\partial t} + \frac{\partial}{\partial x_j}\left(\overline{u}_i \overline{u}_j\right) = -\frac{\partial \overline{p}}{\partial x_j} - \frac{\partial \tau^r_{ij}}{\partial x_i} + \frac{1}{Re}\frac{\partial}{\partial x_j}\left(\frac{\partial \overline{u}_i}{\partial x_j} + \frac{\partial \overline{u}_j}{\partial x_i}\right) \quad , \tag{3.34}$$

that can be solved together with (3.26) modelling τ^r_{ij}.

3.2.2 The Smagorinsky Model

The Smagorinsky [1963] model is a physical space model based on the subgrid viscosity idea. It is assumed that the subgrid stress tensor has a mathematical structure similar to the molecular diffusion, in which the molecular viscosity is replaced by a subgrid viscosity ν_{sgs}, hypothesizing that the smallest scales behaviour is analogous to the Brownian motion of the molecules (Sagaut [2006]). Boussinesq was the first to develop this concept in the following form:

$$\tau^r_{ij} = -\left[\nu_{sgs}\left(\frac{\partial \overline{u}_i}{\partial x_j} + \frac{\partial \overline{u}_j}{\partial x_i}\right)\right] \tag{3.35}$$

It is worth to underline that the subgrid viscosity ν_{sgs}, differently from the molecular viscosity, is a characteristic of the flow and not of the fluid. Furthermore, the formulation (3.35) implies that there is an alignment of the eigenvectors of strain rate tensor and subgrid tensor. However, such concept is physically incorrect because in a turbulent flow there is not a clear separation of scales. In particular in Smagorinsky model the subgrid scales presence depends on the characteristics of the resolved scales and the intrinsic hypothesis of linear dependence between the strain rate tensor and the deviatoric part of subgrid scale tensor is adopted:

$$\tau^r_{ij} = -2\nu_{sgs}\overline{S}_{ij} \tag{3.36}$$

Moreover, the subgrid viscosity is modelled as:

$$\nu_{sgs} = (C_s\overline{\Delta})^2\left|\overline{S}\right| \quad , \tag{3.37}$$

where $\left|\overline{S}\right|$ is the strain rate tensor module, $\overline{\Delta}$ is the LES filter width and C_s is the Smagorinsky constant, which could assume different values in relation to the type of flow studied. For

isotropic homogeneous turbulence and channel flow cases a range values of $C_s = 0.1 - 0.2$ is commonly used, however in the present work a value of $C_s = 0.02$ is used in all the simulations.

Although it is a very efficient way to model the anisotropic residual stress tensor and to represent the dissipative mechanism of turbulence, some are the limits of application of the Smagorinsky model, related to the representation of the energy cascade process and the interactions between resolved and subgrid scales. In a turbulent flow there is a large departure from the local equilibrium, because the turbulent timescale is larger than the shear timescale, causing the subgrid stresses to have a memory of the shear flow. The problem could be solved adopting a non-linear relation between the residual stress tensor and the strain-rate tensor, in which the memory process is introduced. Moreover, for the Smagorinsky model the rate of energy transfer to the subgrid modes can be expressed as (Pope [2000]):

$$\epsilon \equiv -\tau_{ij}^{r}\overline{S}_{ij} = \nu_{sgs}\overline{S}^{2} \tag{3.38}$$

Therefore, looking at equation (3.37) it is evident that the energy transfer rate is always positive, namely the only phenomenon of forward cascade is taken into account, neglecting the negative dissipation of the back-scatter process. Hence, improved subgrid models have been developed such as the dynamic Germano model (Germano et al. [1991]), in which the C_s parameter is not a constant, but it is locally computed and adjusted in relation to the flow behaviour. It is worth noticing that the latter are more computationally demanding rather than the Smagorinsky model.

3.2.3 The Dynamic Germano Model

As mentioned earlier the dynamic Germano model (Germano et al. [1991]) allows to adapt locally the value of C_s parameter. In particular, the LES equations are solved with the application of two different filters: the so-called grid filter, with a bandwidth $\overline{\Delta}$ and the test filter with a bandwidth $\tilde{\Delta} = 2\overline{\Delta}$. The double filtering operation leads to a triple decomposition of the velocity vector:

$$\boldsymbol{u} = \tilde{\overline{\boldsymbol{u}}} + \left(\overline{\boldsymbol{u}} - \tilde{\overline{\boldsymbol{u}}}\right) + \boldsymbol{u}' \quad , \tag{3.39}$$

where the term $\tilde{\overline{\boldsymbol{u}}}$ represents the double filtered velocity, while $\left(\overline{\boldsymbol{u}} - \tilde{\overline{\boldsymbol{u}}}\right)$ defines at the same time the smallest scales resolved by a size $\overline{\Delta}$ and the largest scales not resolved by a width $\tilde{\overline{\Delta}}$. Concerning the residual stress tensor, in 1986 Germano developed its own decomposition, alternative to the Leonard's one (Germano [1986]):

$$\tau_{ij}^{R} = L_{ij} + C_{ij} + R_{ij} \tag{3.40a}$$

$$L_{ij} = \widetilde{\tilde{u}_i\tilde{u}_j} - \tilde{\tilde{u}}_i\tilde{\tilde{u}}_j \tag{3.40b}$$

$$C_{ij} = \widetilde{\tilde{u}_i u_j'} + \widetilde{u_i'\tilde{u}_j} - \tilde{\tilde{u}}_i\tilde{u}_j' - \tilde{u}_i'\tilde{\tilde{u}}_j \tag{3.40c}$$

$$R_{ij} = \widetilde{u_i' u_j'} - \tilde{u}_i' \tilde{u}_j' \tag{3.40d}$$

The application of a single filter gives the following definition of the residual stress tensor:

$$\tau_{ij}^R = \overline{u_i u_j} - \overline{u}_i \overline{u}_j \quad , \tag{3.41}$$

while the double filtering operation leads to:

$$T_{ij} = \widetilde{\overline{u_i u_j}} - \tilde{\overline{u}}_i \tilde{\overline{u}}_j \tag{3.42}$$

Substracting equation (3.42) to equation (3.41), the Germano's identity is obtained:

$$G_{ij} \equiv T_{ij} - \tau_{ij}^R = \widetilde{\overline{u}_i \overline{u}_j} - \tilde{\overline{u}}_i \tilde{\overline{u}}_j \tag{3.43}$$

Furthermore, a revised Smagorisnky model can be employed for the deviatoric part of τ_{ij}^R and T_{ij}:

$$\tau_{ij}^r \equiv \tau_{ij}^R - \frac{1}{3}\tau_{kk}^R \delta_{ij} = -2C_s \overline{\Delta}^2 |\overline{S}| \overline{S}_{ij} \quad , \tag{3.44}$$

$$T_{ij}^d \equiv T_{ij} - \frac{1}{3} T_{kk} \delta_{ij} = -2C_s \tilde{\overline{\Delta}}^2 |\tilde{\overline{S}}| \tilde{\overline{S}}_{ij} \tag{3.45}$$

Differently from the Smagorinsky model, the parameter C_s does not appear as squared (see equations (3.36),(3.37),(3.44) and (3.45) for comparison), allowing the backscatter phenomenon. In conclusion, it is presented the final formulation for dynamically determining the C_s parameter for every time instant all over the computational domain:

$$C_s(\boldsymbol{x}, t) = \frac{M_{ij} G_{ij}}{M_{kl} M_{kl}} \quad , \tag{3.46}$$

with

$$M_{ij} = 2\overline{\Delta}^2 \widetilde{|\overline{S}| \overline{S}_{ij}} - 2\tilde{\overline{\Delta}}^2 |\tilde{\overline{S}}| \tilde{\overline{S}}_{ij}. \tag{3.47}$$

3.2.4 Eddy Diffusivity Model

Similarly to the NS equations the application of a homogeneous filter to equations (3.6) and (3.11) provides the definition of the filtered equations for the calcium hydroxide concentration and particles radius dynamics:

$$\frac{\partial \overline{C}}{\partial t} + \nabla \cdot (\overline{\boldsymbol{u}} \overline{C}) = \frac{D}{ReSc} \nabla^2 \left(\overline{C} \right) + \overline{S}_C - \nabla \cdot \tau_C \qquad , \tag{3.48}$$

$$\frac{\partial \overline{r}_p}{\partial t} + \nabla \cdot (\overline{\boldsymbol{u}} \overline{r}_p) = \overline{S}_{r_p} - \nabla \cdot \tau_{r_p} \qquad , \tag{3.49}$$

where τ_C and τ_{r_p} are the residual fluxes and can be decomposed analogously to the subgrid tensor of the NS momentum equation:

$$\tau_C \equiv \overline{\boldsymbol{u}C} - \overline{\boldsymbol{u}}\overline{C} = L_C + C_C + R_C \qquad , \tag{3.50}$$

$$\tau_{r_p} \equiv \overline{\boldsymbol{u}r_p} - \overline{\boldsymbol{u}}\overline{r}_p = L_{r_p} + C_{r_p} + R_{r_p} \qquad , \tag{3.51}$$

with $L_C, L_{r_p}, C_C, C_{r_p}, R_C, R_{r_p}$ as analogous to Leonard, Cross and Reynolds stresses.

The modelling operation of subgrid passive scalar dynamics is not a trivial task, because there are three physical regimes in isotropic turbulence depending on the Prandtl number (Sagaut [2006]), expressed as:

$$Pr \equiv \frac{\nu}{D} \tag{3.52}$$

Regarding this, it is worth to define the scalar diffusion cutoff length, also named as Obukhov-Corrsin scale as a function of the Kolmogorov scale η_K:

$$\eta_\theta = \left(\frac{1}{Pr}\right)^{3/4} \eta_K \qquad , \tag{3.53}$$

which can be expressed in form of wave number as:

$$k_\theta = Pr^{3/4} k_\eta \tag{3.54}$$

The three regimes are the following ones (the spectrum of which is shown in figure 3.3 in function of the wave number of the scales):

- $Pr \ll 1$: the molecular viscosity is much smaller than the molecular diffusivity.
- $Pr \cong 1$: in this regime the scalar diffusion cutoff scale η_θ is very close to the viscous cutoff scale of velocity η_K.
- $Pr \gg 1$: in this regime the scalar diffusion cutoff scale is much smaller than the viscous cutoff scale of velocity.

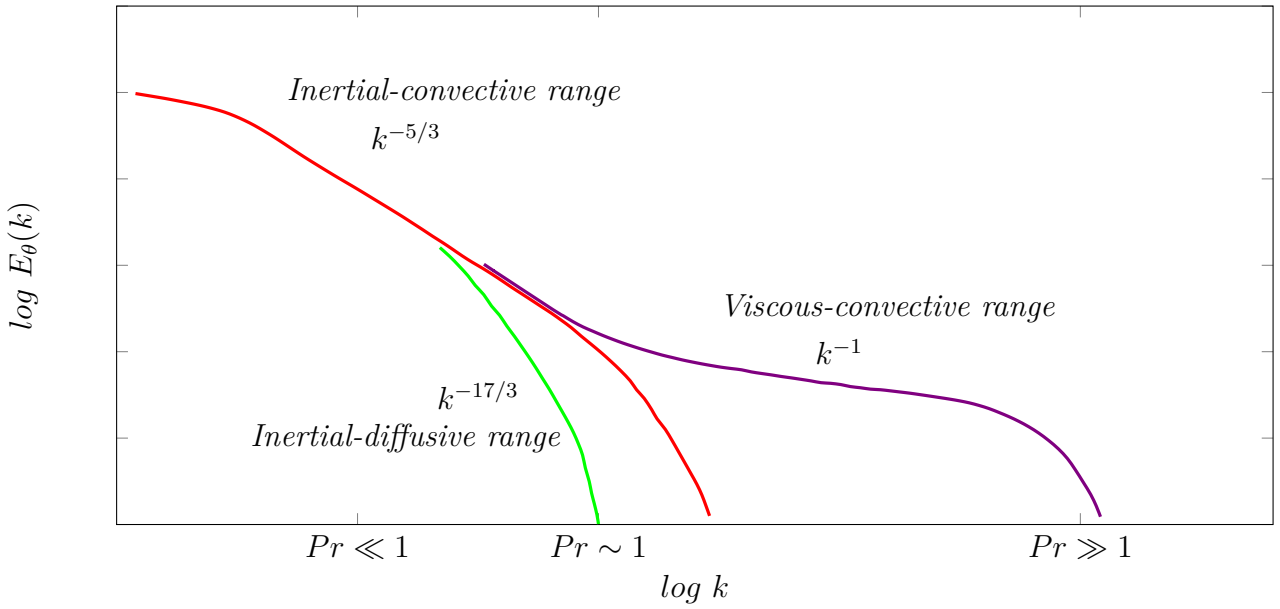

Figure 3.3: Schematic of passive scalar variance spectrum for three regimes: $Pr \ll 1$ (red), $Pr \cong 1$ (green), $Pr \gg 1$ (purple). Sreenivasan [2019] p. 18177

As regards the scalar diffusion cutoff length for the physical regime $Pr \gg 1$ the Obukhov-Corrsin is not valid and it is substituted by the Batchelor wave number:

$$k_B = \left(\frac{\epsilon}{\nu D^2}\right)^{1/4} \quad , \tag{3.55}$$

where ϵ is the energy dissipation rate and ν the molecular kinematic viscosity. In particular the kinetic energy spectrum provides the existence of an inertial-convective range ($k \ll k_\theta \ll k_\eta$), in which the scalar and velocity structures are not influenced by viscosity and diffusivity and a viscous-convective range ($k_\theta \ll k \ll k_\eta$), where velocity scales are hugely affected by molecular viscosity, while molecular diffusivity does not influence scalar scales. On the contrary the regime for $Pr \ll 1$ besides the inertial-convective range presents an inertial-diffusive range, in which diffusivity strongly affects scalar fluctuations, while molecular viscosity has no effect on velocity fluctuations. Therefore, the modelling operation of scalar subgrid scales must take into account in which range of the energy spectrum the LES cutoff is set. However, for most LES analysis the cutoff is located in the inertial-convective range, because a cutoff in the viscous-convective range requires a very fine grid of computation.

The closure procedure commonly used for modelling subgrid scales of the passive scalar consists in defining the so-called subgrid Prandtl number Pr_{sgs}. The subgrid Prandtl number is the base of the Eddy diffusivity model used in this study. Similarly to the Boussinesq's hypothesis for modelling the residual stress tensor of velocity, the Eddy diffusivity model assumes the subgrid tensor of the generic passive scalar θ as alligned to the gradient of the

filtered passive scalar, by means of the subgrid diffusivity:

$$\tau_\theta = -D_{sgs}\nabla\overline{\theta} \qquad , \tag{3.56}$$

with

$$D_{sgs} = \frac{\nu_{sgs}}{Pr_{sgs}} \tag{3.57}$$

The eddy viscosity ν_{sgs} is the one computed by the Smagorinsky model in the filtered momentum equation (see Section 3.2.2), while the subgrid Prandtl number varies typically into a range between 0.1-1 and the most common value, also used in this study, is $Pr_{sgs} = 0.6$ and it is kept constant (Sagaut [2006]).

Despite the idea of establishing a subgrid Prandtl number is intuitive, there are some limits of application. Indeed, the subgrid Prandtl number does not have a universal behaviour, depending on the case studied. Concerning this a detailed explanation is given in the study of a passive scalar in isotropic turbulence by Lesieur and Rogallo [1989]. Hence, a passive scalar modelling approach based on a subgrid Prandtl number arises some errors because there could be substantial differences between kinetic energy and passive scalar variance spectrum. The eddy diffusivity model could be improved adopting a dynamic subgrid Prandtl number, that would be a function of space and time. Although it would not still be sufficient to represent the case of LES cutoff wave number set in the viscous-convective range, it would be able to faithfully model the case in which all the passive scalar scales are solved, while some subgrid velocity scales exist.

3.3 Propeller modelling

A further step for simulating a ship's wake is to introduce the propeller effects on the flow. In order to do so, it is necessary to find an appropriate modelling for both propeller and forces generated. The presence of the propeller intensely changes the behaviour of the flow, a quite realistic model is indeed required. Nevertheless, introducing a propeller model demands a high resolution, significantly increasing the computational cost. A simple way to implement a propeller is to predict the rotor volume forces and replace the actual blades with their effect on the flow. Therefore, the forces computed are directly the forces applied on the fluid. They are introduced as body forces f_i in the Navier-Stokes equations, similarly to a source term.

The model used in this thesis is a Rotating Blade Element Theory (R-BET), a method that combines the BET with the Rotating Actuator Disk Model (RADM), reworked from the Zangrandi [2019] work and previously developed by Ciri et al. [2015]. However, a first analysis is made without considering blades, introduced later.

In the blade element theory the propeller forces are calculated for an infinitesimal section of the blade. This section is characterized by:

- chord c;
- blade angle β;
- lift and drag coefficients (C_L and C_D);
- local flow properties (velocity U and flow/relative angle ϕ).

A scheme of the blade with all the parameters is reported in fig. 3.4.

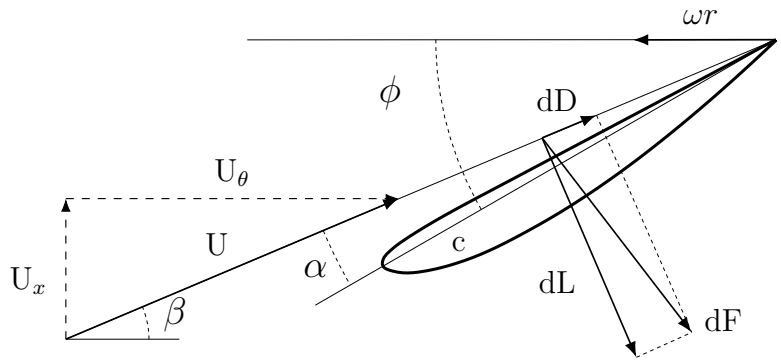

Figure 3.4: Scheme of forces and angles for the propeller blade section

The flow angle is computed as:

$$\phi = \arctan\left(\frac{U_x}{U_\theta - \omega r}\right) \tag{3.58}$$

Where U_x and U_θ are the velocities in the axial and azimuthal (tangential) directions, ω the angular velocity of the blades and r the local radius. The velocity in the radial direction is neglected. In order to compute U_θ, it is necessary to project the y- and z-components of the local velocity along the tangential direction. The relative velocity is computed consequently:

$$U_{rel} = \sqrt{U_x^2 + (U_\theta - \omega r)^2} \tag{3.59}$$

The values of lift and drag coefficients have been taken from Zhiheng et al. [2019], which gives punctual values on specific positions along the radius. These values are specific for the KP-505 propeller, which is the propeller of the Korean Research Institute for Ships and Ocean engineering (KRISO) container ship (KCS) (the same type of ship used in Dall'Aglio [2019]). The choice fell on this kind of vessel because their considerable days of navigation and total distance covered make them a good candidate for Ocean Liming project:

R	0.1	0.16	0.2	0.24	0.28	0.32	0.36	0.4	0.44	0.48
$\mathbf{C}_L$	0.150	0.220	0.226	0.223	0.213	0.199	0.186	0.173	0.154	0.199
$\mathbf{C}_D$	0.009	0.026	0.032	0.031	0.029	0.025	0.021	0.016	0.012	0.012
c	0.236	0.270	0.299	0.327	0.348	0.358	0.355	0.337	0.298	0.225

Table 3.1: Chord, Lift and Drag coefficients for the propeller KP-505 with J=0.6

R	0.1	0.16	0.2	0.24	0.28	0.32	0.36	0.4	0.44	0.48
$\mathbf{C}_L$	0.308	0.373	0.369	0.361	0.350	0.343	0.336	0.342	0.387	0.675
$\mathbf{C}_D$	0.097	0.107	0.104	0.097	0.089	0.080	0.071	0.062	0.064	0.100
c	0.236	0.270	0.299	0.327	0.348	0.358	0.355	0.337	0.298	0.225

Table 3.2: Chord, Lift and Drag coefficients for the propeller KP-505 with J=0.12

Those coefficients are computed for specific advance ratios J, defined as:

$$J = \frac{U}{nD_{prop}} \tag{3.60}$$

where U is the freestream velocity, n is the rotational speed of the propeller in RPS (rounds per second) and D_{prop} is the propeller diameter. With the parameters used in table 6.1, the advance ratios adopted in the present work are $J = 0.6$ and $J = 0.12$.

An interpolation between two values must be done for cells in intermediate positions. Those values are assumed to be constant, with no twist of the blades and constant Angle of Attack. The force components of the blade section are computed from those parameters as follows:

$$f_{axial} = \frac{1}{2}U_{rel}^2 c_{interp} D_p rop \left(fC_{L_{interp}} \cos\phi - C_{D_{interp}} \sin\phi\right) \quad , \tag{3.61}$$

$$f_\theta = \frac{1}{2}U_{rel}^2 c_{interp} D_p rop \left(fC_{L_{interp}} \sin\phi - C_{D_{interp}} \cos\phi\right) \quad , \tag{3.62}$$

where f is a coefficient that takes into account the tip effect (the same implemented in OpenFOAM and presented in Dall'Aglio [2019]), defined as follows:

$$\begin{cases} f = 1 & for\ r_{cell} < 0.96R \\ f = 0 & for\ r_{cell} > 0.96R \end{cases}$$

and R is the disk radius. The subscript "$axial$" refers to the x-direction (perpendicular to the propeller disk), but f_x is used to indicate the volumetric force.

It is necessary to return to x-, y- and z-components, so they can be added in calculation of the three Right-Hand Side terms.

$$f_x = f_{axial}\ N_B\ dx\ dy \left(\frac{1}{2\pi r_{cell}\ dx\ dy\ dz}\right) \quad , \tag{3.63}$$

$$f_y = -f_\theta\ N_B\ dx\ dy \left(\frac{z_{cell}}{r_{cell}}\right)\left(\frac{1}{2\pi r_{cell}\ dx\ dy\ dz}\right) \quad , \tag{3.64}$$

$$f_z = f_\theta\ N_B\ dx\ dy \left(\frac{y_{cell}}{r_{cell}}\right)\left(\frac{1}{2\pi r_{cell}\ dx\ dy\ dz}\right) \quad , \tag{3.65}$$

When blade are introduced, in order to recreate them each force component is multiplied by a Gaussian function(Zangrandi [2019]). This Gaussian kernel is defined as:

$$G_{Gauss} = exp\left[-\left(\frac{x - x_{disk}}{\epsilon_{prop}}\right)^2\right] \cdot exp\left[-\left(\frac{\theta - \theta_B}{\pi/N_B}\right)^2\right] \tag{3.66}$$

with $\epsilon_{propeller}$ the disk thickness (in this work a thickness of two adjacent cells is adopted to avoid instability Martinez-Tossas et al. [2015]) and N_B the number of blades (here 5 blades are used).
This function is dependent on the cell position in axial and azimuthal directions (x and θ), the position of a blade θ_B and the longitudinal position of the disk x_{disk}. The function generates a distribution similar to the front view of the blades, having its maximum near every θ_B and going to zero elsewhere. Finally, each component of the total force $\boldsymbol{F} = [F_x, F_y, F_z]^T$ is computed as:

$$F_i = \frac{f_i\ G_{Gauss}}{2\pi} \tag{3.67}$$

4. Code Implementation

The code is a parallel Finite Differences - Large Eddy Simulation solver, wrote in Fortran90 language and based on a staggered Cartesian grid. The peculiarity of this grid is that the velocity values are located on the interface between two cells, marked with consecutive indices (see figure 4.2). The parallel computation is obtained by using the Message Passing Interface (MPI) approach. Because of the dimension and complexity of this code, it is divided in multiple interactive modules that are coordinated by a main file built for a specific test case. The whole code (main file and modules) is launched by a "Makefile" that starts the simulation. This work is focused on the development of the modules related to LES approach and passive scalar dynamics. In the following paragraphs all the features mentioned above will be exploited in detail.

4.1 Staggered Grid

A staggered grid is a kind of grid that uses different control volumes for the fluid dynamic quantities: the velocity components are located on the interface between two consecutive cells, while the scalar quantities, such as pressure and passive scalar, are located at the centre of the cell. A representation of this grid is given in fig. 4.2. This grid configuration is a solution to an instability problem: in case pressure and velocity components locations were the same, there would be spurious pressure modes that cause instability (for the details of this instability problem we refer to Quarteroni [2016]).

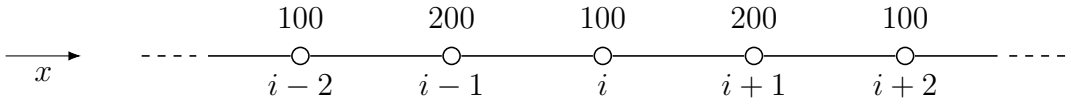

Figure 4.1: Wavy pattern of pressure (or velocity)

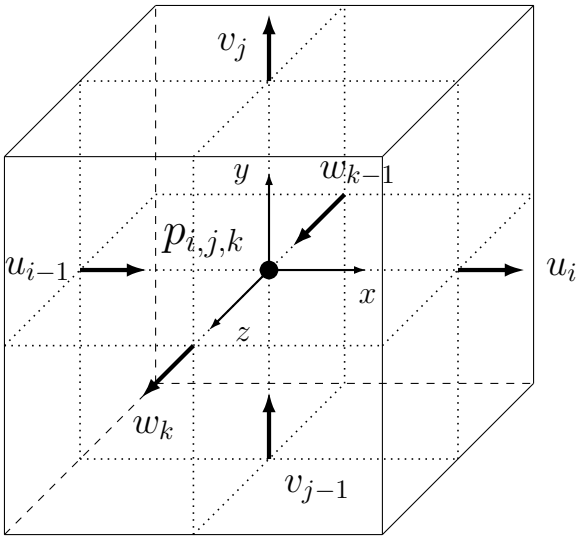

Figure 4.2: Three-dimensional staggered grid

An intuitive example of such problem, related to the spurious pressure modes, is highlighted in Patankar [1980]. As it can be seen in fig. 4.1, a wavy pattern of pressure (or a velocity component) could arise in a time-marching numerical simulation. Therefore, if a centred-finite difference scheme is employed for the computation of a first order derivative at the point of index i, this calculation only depends on values of $i+1$ and $i-1$ points. For example, the finite difference discretization of the pressure gradient in the x-direction momentum equation, assuming uniform grid, would be:

$$\frac{dp}{dx} \cong \frac{p_{i+1} - p_{i-1}}{2\Delta x} \tag{4.1}$$

The consequence is that the first derivative would result to be null, thus such pressure field would be felt as uniform by the momentum equation, making such unrealistic solution preserved throughout the simulation. The same would happen for velocity components, because an alternate pattern would still satisfy the discretized continuity equation. Similar considerations could be done for two-dimensional and three-dimensional problems with a checkerboard pattern of the pressure and velocity field.

The use of a staggered grid allows to prevent such problems. Since the three components of the momentum equation are evaluated at the corresponding nodes of the velocity components and the continuity equation is evaluated at pressure nodes, the first order derivative centred finite differences are computed between two adjacent nodes. However, with the implementation of a staggered grid particular attention has to be taken with respect to the boundary conditions. Indeed, some variables could not be well determined at the boundaries, hence is suggested (Harlow and Welch [1965]) the use of ghost cells outside the boundaries, inside

which the variable assume a certain value in order to have desired value with an appropriate interpolation at the boundaries.

In conclusion, one of the advantages of using a staggered grid is that only "reasonable" velocity fields could satisfy the continuity equation, preventing wavy velocity and pressure field as possible solutions. Another important advantage is that the pressure difference between two consecutive grid points naturally drives the flow velocity located between these grid points.

4.2 Cauchy Problem

The numerical solution of Navier-Stokes Equations, as a PDE, implies to define an initial condition for problem variables across the entire domain and boundary conditions over the entire boundary of the computational domain for every time instant. For this reason, the time integration of the NS Equations is analogous to solve a Cauchy problem, which is a system of equation formulated as:

$y : I \subset \mathbb{R} \to \mathbb{R}$ such that

$$\begin{cases} u'(t) = f(t, u(t)) \\ u(t_0) = u_0 \end{cases} \tag{4.2}$$

Unfortunately, rare are the cases in which this kind of problem admits an explicit solution. In many cases the solution is not even given in implicit form. Therefore, the strategy is to use a numerical method in order to find a numerical solution. Such numerical methods could be classified as single step or multistep methods, which, in turn, can be divided in explicit and implicit methods.

Classic and simple single step methods are the so called forward or backward Euler method:

$$u_{n+1} = u_n + hf_n \qquad Forward \;\; Euler \tag{4.3}$$

$$u_{n+1} = u_n + hf_{n+1} \qquad Backward \;\; Euler \tag{4.4}$$

where h represents the discretized time-step. In particular, while for the forward Euler method the numerical solution u_{n+1} depends only on the previous value u_n, in the backward method the numerical solution depends also on itself. Hence the first is said to be explicit and second implicit method. Consequently, the implicit methods are computationally more expensive than the explicit ones. However, the first have better stability properties than the latter (A. Quarteroni [2008]). Moreover, both Forward and Backward Euler methods are of first

order accuracy. Among the single-step methods the implicit trapezoidal method is the one with second order accuracy, and it is defined as:

$$u_{n+1} = u_n + \frac{1}{2}h(f(u_n) + f(u_{n+1})) \tag{4.5}$$

There are other methods that allow to achieve high accuracy, the so-called *multistep methods*. Such numerical methods use high order polynomial interpolation between several previous values of the solution and/or its derivative.
Among them the r-step linear multistep methods are widely used and have the following form:

$$\sum_{r}^{j=0} \alpha_j u_{n+j} = k \sum \beta_j f(u_{n+j} t_{n+j}) \tag{4.6}$$

The value U_{n+r} is obtained from the previous ones and the function f evaluated at these points. If $B_r = 0$ than the method is explicit, while for $B_r \neq 0$ it is implicit. There are different classes of these methods that are functional. The Adams methods which have the following form:

$$u_{n+r} = u_{n+r-1} + k \sum_{j=0}^{r} \beta f(u_{n+j}) \tag{4.7}$$

These methods have these conditions on α :

$$\alpha_r = 1, \quad \alpha_{r-1} = -1, \quad and \quad \alpha_j = 0 \quad for \quad j < r-1$$

The higher accuracy can be achieved, alternatively, with the implementation of a single-step multistage method. Specifically, this is the case of the present work, in which code a three-stage explicit Runge Kutta method algorithm is employed. This method provides the final solution of a single time-step is determined, through the definition of intermediate values of the solution.

The scheme used, presented in Kennedy et al. [2000], is a low-storage three-stage explicit Runge-Kutta method. What distinguishes it is the efficiency accuracy, because it is a third-order accuracy method with a required memory storage comparable to the amount of memory required in a second-order method. The updated solution of subsequent time-steps are computed through three intermediate fractional steps formulated as:

$$u_i^{rk+1} = u_i^{rk} + \beta \Delta t RHS^{rk-1}(u_i^{n-1}) + \alpha \Delta t RHS^{rk}(u_i^{n-1}) \qquad for \quad rk = 1, 2, 3 \tag{4.8}$$

where $\Delta t = t_{n+1} - t_n$ is the time step and RHS represents the right hand side of NS or passive scalars equations. A third-order Taylor-series expansion of the solution at time t_{n+1} gives the following values of α and β parameters:

$$\alpha_1 = \frac{8}{15} \quad \alpha_2 = \frac{5}{12} \quad \alpha_3 = \frac{3}{4}$$

$$\beta_1 = 0 \quad \beta_2 = -\frac{17}{60} \quad \beta_3 = -\frac{5}{12}$$

It is worth noticing that $\beta_1 = 0$ in order to have an explicit algorithm.

To complete the discussion about the numerical time integration scheme the following paragraph is dedicated to the comparison between multi-step and one-step methods. The single-step methods can be applied starting as early as the first time step from the initial conditions, while the multi-step algorithms need another method to be initially started. Furthermore, the multi-step schemes require more attention in cases of non smooth solutions and variable time steps. On the contrary, a multi-stage Runge-Kutta method requires the evaluation of the right hand side of the equations several times, making the scheme more expensive and complicated to implement than a multi-step method.

4.3 Discretization of the convective and diffusion terms

The RHS of filtered NS and passive scalars equations are composed by the convective term, the diffusion term and the subgrid scales contribution introduced in Sections 3.2.2 and 3.2.4 of Chapter 3. The RHS of filtered NS equations presents also the pressure gradient term, that needs a more detailed discussion that is developed in Section 4.4.

Concerning the NS equations a mimetic finite difference discretization has been adopted, developed by Abbà and Bonaventura [2008], with a vorticity preservation that allows to correctly reproduce energy or enstrophy spectra. Consequently, the incompressible NS equations have been reformulated in the following way:

$$\nabla \cdot \boldsymbol{u} = 0 \qquad , \tag{4.9}$$

$$\frac{\partial \boldsymbol{u}}{\partial t} = -\boldsymbol{\omega} \times \boldsymbol{u} - \nabla (p + K) + \frac{1}{Re} \nabla \times \boldsymbol{\omega} \qquad , \tag{4.10}$$

where $\boldsymbol{\omega} = \nabla \times \boldsymbol{u}$ is the vorticity, while $K = |\boldsymbol{u}|^2 / 2$ represents the kinetic energy. Considering the staggered grid configuration of figure 4.2, the vorticity fluxes are computed at the cell faces with the following formulation:

$$\omega^x_{i,j+1/2,k+1/2} = \frac{w_{i,j+1,k+1/2} - w_{i,j,k+1/2}}{\Delta y_{j+1/2}} - \frac{v_{i,j+1/2,k+1} - v_{i,j+1/2,k}}{\Delta z_{k+1/2}} \tag{4.11}$$

$$\omega^y_{i+1/2,j,k+1/2} = \frac{u_{i+1/2,j,k+1} - u_{i+1/2,j,k}}{\Delta z_{1+1/2}} - \frac{w_{i+1,j,k+1/2} - w_{i,j,k+1/2}}{\Delta x_{i+1/2}} \tag{4.12}$$

$$\omega^z_{i+1/2,j+1/2,k} = \frac{v_{i+1,j+1/2,k} - v_{i,j+1/2,k}}{\Delta x_{i+1/2}} - \frac{u_{i+1/2,j+1,k} - u_{i+1/2,j,k}}{\Delta y_{j+1/2}} \tag{4.13}$$

The equations (4.9) and (4.10) have been discretized and the definitions of vorticity vector components have been applied to them. The discretized equations obtained are shown in detail in appendix A. This mimetic approach, differently from the other classic methods, prevents spurious vorticity production, enhancing the local accuracy and stability of the code.

On the contrary, for the slaked lime concentration and particle radius equations a conservative scheme, with a second-order accuracy discretization, is employed.

$$\frac{\partial C}{\partial t} = -\nabla \cdot (\boldsymbol{u}C) + \frac{1}{ReSc}\nabla^2(C) + S_c \tag{4.14}$$

The discretized equation of (4.14) are also presented in appendix A.

4.4 Pressure Correction

The system composed by continuity equation (4.9) and momentum equation (4.10) must be solved to compute the space and time evolution of pressure and velocity of the flow. However, rearranging them in a single discretized linear system of equations corresponds to solve a saddle-point problem, more difficult to solve (Zanelli [2018]). In the present work a more efficient solution method is adopted, presented in Guermond and Minev [2011]. It consists in solving incompressible NS equations by decoupling the incompressibility constraint from the momentum equation with a fractional time stepping technique alongside a direction splitting algorithm for pressure correction term in the momentum equation. The discretization of time progress for velocity in the momentum equation can be expressed with the following formulation:

$$\frac{\boldsymbol{u}^n - \boldsymbol{u}^{n-1}}{\Delta t} = RHS(\boldsymbol{u}^{n-1}) - \nabla(p^{n-1} + \Phi) \quad , \tag{4.15}$$

where $RHS(\boldsymbol{u}^{n-1})$ includes convective and diffusive term evaluated at the previous time step, while Φ represents the pressure increment. To solve equation (4.15), it is decomposed with the projection method, firstly proposed by Chorin [1968]. However, in this thesis the Crank-Nicholson incremental scheme is applied, because the introduction of the pressure increment Φ allows to improve the splitting error and time accuracy with respect to the Chorin formulation (Guermond and Minev [2011]). The method is presented below:

$$\begin{cases} \dfrac{\boldsymbol{u}^* - \boldsymbol{u}^{n-1}}{\Delta t} = RHS(\boldsymbol{u}^{n-1}) - \nabla(p^{n-1}) \\ \nabla^2\Phi = \dfrac{1}{\Delta t}\nabla \cdot \boldsymbol{u}^* \\ \dfrac{\boldsymbol{u}^n - \boldsymbol{u}^*}{\Delta t} = -\nabla\Phi \\ p^n = p^{n-1} + \Phi \end{cases} \tag{4.16}$$

The momentum equation is primarily solved without the incompressibility constraint, then applying the divergence operator to the first equation of system (4.16) with the addition of the pressure increment, the incompressibility condition is satisfied projecting the resulting velocity $\boldsymbol{u}^*$ onto this function space. It is worth to notice that the projection method step of the system (4.16) must be integrated with the Runge-Kutta step (4.8). Hence, the complete time advance of the velocity field can be summarized in the following steps:

$$\begin{cases} \boldsymbol{u}^{*\,rk} = \boldsymbol{u}^{n-1} + \beta \Delta t RHS^{rk-1} + \alpha \Delta t RHS^{rk} \\ \nabla^2 p^{rk} = \dfrac{1}{\Delta t} \nabla \cdot \boldsymbol{u}^{*\,rk} \qquad\qquad for\ rk = 1, 2, 3 \\ \boldsymbol{u}^{rk} = \boldsymbol{u}^{*\,rk} - (\alpha + \beta) \nabla p^{rk} \end{cases} \tag{4.17}$$

4.4.1 Thomas Algorithm

The advantages of using a projection method for the solution of the momentum equation could be nullified if an equally efficient algorithm for solving the Poisson equation for pressure increment is not used. Guermond and Minev [2011] proposed to substitute the Laplacian operator in the Poisson equation with a generic operator, presented in details in Section 4.4.2, that allows to solve a sequence of one-dimensional problems. Each of these one-dimensional problems can be rearranged in tridiagonal form, enabling to apply the efficient Thomas algorithm (A. Quarteroni [2008]).

Given the system $A\Phi = d$ with matrix A in tridiagonal form:

$$A = \begin{bmatrix} a_1 & c_1 & & 0 \\ e_2 & a_2 & \ddots & \\ & \ddots & & c_{n-1} \\ 0 & & e_n & a_n \end{bmatrix} , \tag{4.18}$$

where the matrix components are zero, except the ones on the diagonal and first supra-diagonal and sub-diagonal. The Gauss factorisation of A ($LU = A$) consists in two bi-diagonal matrix of the form:

$$L = \begin{bmatrix} 1 & & & 0 \\ \beta_2 & 1 & & \\ & \ddots & \ddots & \\ 0 & & \beta_n & 1 \end{bmatrix}, \; U = \begin{bmatrix} \alpha_1 & c_1 & & 0 \\ & \alpha_2 & \ddots & \\ & & \ddots & c_{n-1} \\ 0 & & & \alpha_n \end{bmatrix}. \tag{4.19}$$

The α and β coefficients of L and U matrix can be obtained from the following recursive formulas:

$$\alpha_1 = a_1, \quad \beta_i = \frac{e_i}{\alpha_{i-1}}, \quad \alpha_i = a_i - \beta_i c_{i-1}, \qquad for\ i = 2, ..., n \tag{4.20}$$

Subsequently, the system $A\Phi = d$ can be decomposed in two bidiagonal systems $L\Psi = d$ and $U\Phi = \Psi$, which solution is given below:

$$(L\Psi = d) \qquad \Psi_1 = d_1, \quad \Psi_i = d_i - \beta_i \Psi_{i-1}, \qquad for\ i = 2, ..., n \tag{4.21}$$

$$(U\Phi = \Psi) \qquad \Phi_n = \frac{\Psi_n}{\alpha_n}, \quad \Phi_i = \frac{\Psi_i - c_i \Phi_{i+1}}{\alpha_i}, \qquad for\ i = n-1, ..., 1 \tag{4.22}$$

The Thomas algorithm is one of the most efficient techniques for the solution of linear equations system. Indeed, Gaussian elimination method requires a computational cost of n^3-order of operations, while the Thomas algorithm has a cost of order n. Furthermore, the latter is more scalable making its application easier in a parallel code, as in the present work.

4.4.2 Alternating Direction Implicit Method

In order to take advantage of Thomas algorithm efficiency for the solution of a boundary value problem, the Poisson equation must be rearranged so that only one-directional derivative operator has to be solved at a time. This is the main concept of the splitting operator employed in the Alternating Direction Implicit method (ADI). In particular, the Laplacian operator is substituted by the following A operator (for details of the method see Guermond and Minev [2011]):

$$\nabla^2 \Phi = -\nabla \cdot \boldsymbol{u}^* \qquad \longrightarrow \qquad \nabla \cdot \boldsymbol{u}^* + \Delta t A \Phi = 0 \tag{4.23}$$

$$A = \left(1 - \frac{\partial^2}{\partial x^2}\right)\left(1 - \frac{\partial^2}{\partial y^2}\right)\left(1 - \frac{\partial^2}{\partial z^2}\right) \quad , \tag{4.24}$$

that applied to equation (4.23) corresponds to the solution of this system:

$$\begin{cases} \psi - \dfrac{\partial^2 \psi}{\partial x^2} = -\dfrac{1}{\Delta t} \nabla \cdot \boldsymbol{u}^* & \dfrac{\partial \psi}{\partial x}|_{x \in \partial\Omega} = 0, \\ \chi - \dfrac{\partial^2 \chi}{\partial y^2} = \psi & \dfrac{\partial \chi}{\partial y}|_{y \in \partial\Omega} = 0, \\ \phi - \dfrac{\partial^2 \phi}{\partial z^2} = \chi & \dfrac{\partial \phi}{\partial z}|_{z \in \Omega} = 0 \end{cases} \tag{4.25}$$

The parallel formulation of ADI technique provides the decomposition of A matrix, in order to split the problem into smaller and semi-independent sub-problems, for which solution the Schur complement technique is adopted.

4.4.3 Schur Complement Method

As stated in Section 4.4.2, the ADI technique allows to decompose the solution of the Poisson equation, for pressure increment, in the solution of a tridiagonal linear system of equations. The Schur complement algorithm, presented in Zanelli [2018], has the advantage to split the solution of a tridiagonal linear system into a series of smaller, semi-independent assignments. A representation of the layout of a tridiagonal system, which domain is divided into several processes, is given below:

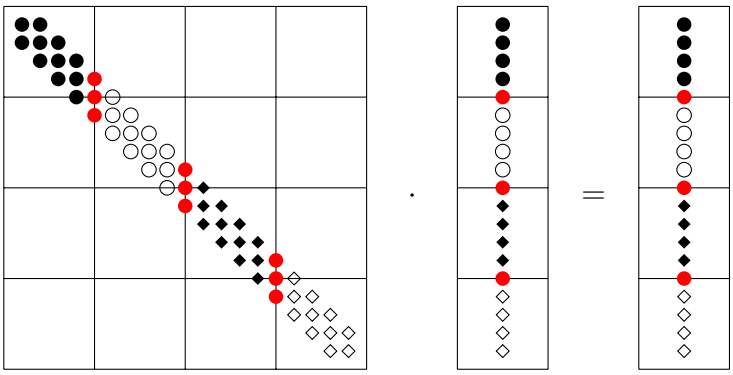

Figure 4.3: Tridiagonal system for several processes. Reworked from Zanelli [2018]

where the red circles represent the components shared by two processes. Given a generic system:

$$\boldsymbol{M} \cdot \begin{Bmatrix} x \\ y \end{Bmatrix} = \begin{Bmatrix} a \\ b \end{Bmatrix} \tag{4.26}$$

matrix M can be split into blocks:

$$\boldsymbol{M} = \begin{bmatrix} \boldsymbol{A} & \boldsymbol{B} \\ \boldsymbol{C} & \boldsymbol{D} \end{bmatrix} \tag{4.27}$$

Hence, the Schur complement of a single matrix block can be introduced:

$$\boldsymbol{M}/\boldsymbol{D} = \boldsymbol{A} - \boldsymbol{B}\boldsymbol{D}^{-1}\boldsymbol{C} \qquad \textit{D Schur Complement} \tag{4.28}$$

$$\boldsymbol{M}/\boldsymbol{A} = \boldsymbol{D} - \boldsymbol{C}\boldsymbol{A}^{-1}\boldsymbol{B} \qquad \textit{A Schur Complement} \tag{4.29}$$

Applying $\boldsymbol{A}$ and $\boldsymbol{D}$ Schur complement to system (4.26), the problem can be split into two independent tasks:

$$\begin{cases} x = (\boldsymbol{M}/\boldsymbol{D})^{-1} \left(a - \boldsymbol{B}\boldsymbol{D}^{-1}b\right) \\ y = (\boldsymbol{M}/\boldsymbol{A})^{-1} \left(b - \boldsymbol{C}\boldsymbol{A}^{-1}a\right) \end{cases} \tag{4.30}$$

Despite the splitting into smaller sub-problems, the configuration of the system of figure 4.3, with the application of Schur complement, requires many matrices inversions. Furthermore, the interfaces values between processes represent a bottle-neck for the efficiency of the system solution. In order to avoid these issues the system can be rearranged such that the interface components are isolated from the ones internal to the processes. This procedure is presented in the following figure:

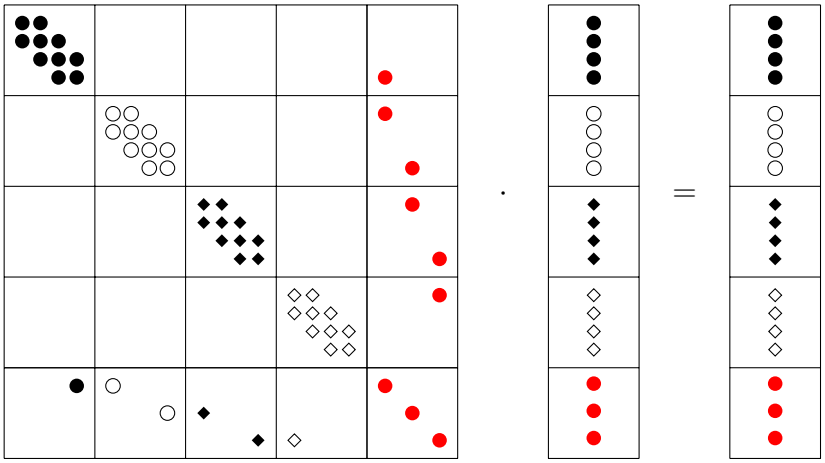

Figure 4.4: Rearranged tridiagonal system with isolated interface components. Reworked from Zanelli [2018]

Therefore the system can be divided into internal and interface blocks:

$$\begin{bmatrix} \boldsymbol{A}_{ii} & \boldsymbol{A}_{ie} \\ \boldsymbol{A}_{ei} & \boldsymbol{A}_{ee} \end{bmatrix} \cdot \begin{Bmatrix} x_i \\ x_e \end{Bmatrix} = \begin{Bmatrix} f_i \\ f_e \end{Bmatrix} \tag{4.31}$$

where $\boldsymbol{A}_{ii}$ is block-diagonal and each block corresponds to the internal values of a single process. Once restructured the problem as in figure 4.4, its solution is composed by the following stages:

- At the beginning the Master processor computes the Schur complement:

$$\boldsymbol{A}/\boldsymbol{A}_{ii} = \left(\boldsymbol{A}_{ee} - \boldsymbol{A}_{ei}\boldsymbol{A}_{ii}^{-1}\boldsymbol{A}_{ie}\right) \tag{4.32}$$

- Subsequently each processor solves its portion of the system with the Thomas algorithm, for every time step:

$$x_i^p = \boldsymbol{A}_{ii}^{p-1} f_i^p \tag{4.33}$$

$$\boldsymbol{A}_{ii} = \begin{bmatrix} \boldsymbol{A}_{ii}^1 & 0 & \dots & 0 \\ 0 & \boldsymbol{A}_{ii}^2 & \dots & 0 \\ \vdots & \vdots & \ddots & \vdots \\ 0 & 0 & \dots & \boldsymbol{A}_{ii}^{N_p} \end{bmatrix} \quad , \quad f_i = \begin{Bmatrix} f_i^1 \\ \vdots \\ \vdots \\ f_i^{N_p} \end{Bmatrix}$$

- Each processor sends $\boldsymbol{A}_{ei}^{p}\boldsymbol{A}_{ii}^{p-1}f_i^p$ to the Master, that assembles every portion in the complete vector $\boldsymbol{A}_{ei}\boldsymbol{A}_{ii}^{-1}f_i$.
- The Master process finds the solution for x_e:

$$x_e = (\boldsymbol{A}/\boldsymbol{A}_{ii})^{-1}(f_e - \boldsymbol{A}_{ei}\boldsymbol{A}_{ii}^{-1}f_i) \quad , \tag{4.34}$$

  and broadcasts it to the other processes.
- Each process computes its portion of the vector x_i:

$$x_i^p = \boldsymbol{A}_{ii}^{p-1}(f_i^p - \boldsymbol{A}_{ie}^{p}x_e) \tag{4.35}$$

Given the number of points N in a single direction in the interface between two processes, the complete procedure of data exchange has a computational cost of N^2.

4.5 Numerical Time Stability

Despite the stability of the Runge-Kutta method presented in Section 4.2, the choice of the advancement time step of the simulations must be in compliance with specific conditions for convective and viscous terms, to ensure numerical stability. Since the convective term is treated explicitly, the concept of Courant-Friedrich-Lewy number (CFL) must be introduced. The CFL number condition, firstly proposed by R.Courant et al. [1967], limits the distance travelled by a particle in a single direction with reference to the grid size in such direction:

$$\begin{cases} CFL = \left|\dfrac{u_i \Delta t}{x_i}\right| \\ \left|\dfrac{u_i \Delta t}{x_i}\right|_{max} \leq CFL_{max} \end{cases} \tag{4.36}$$

The CFL_{max} limit cannot be defined a priori, but it is a specific parameter of the flow conditions simulated, in the majority of the cases $CFL_{max} \leq 1$. Therefore, refining the mesh means to make the CFL condition more strict, reducing the amplitude of the time step and increasing the computational cost. Analogously, the explicit treatment of the viscous term forces to respect another stability restriction (presented in detail by Peyret and Taylor [2012]):

$$\frac{\Delta t}{x_i^2 Re} \leq \frac{1}{2n} \quad , \tag{4.37}$$

for n-dimensional domain. This condition constraints the diffusion in a grid cell for a single time step. In the present thesis each time step is chosen as the minimum time step among the ones computed in the three directions, considering the conditions (4.36) and (4.37) in the entire computational domain. It is worth noticing that the stability conditions for convective and viscous terms can be avoided employing a implicit numerical method, nonetheless computationally more demanding.

4.6 Parabolic Grid Deformation

The generation of a proper grid for CFD problems is a key step to obtain reliable results. The grid deformation has to fit the specific problem, creating higher density in the regions where the flow behaviour needs to be studied in detail. On the other hand, all the regions where the flow remains almost unperturbed a deeper analysis is not needed. According to those guidelines, the mesh used in this thesis work has been made denser near the centerline of the longitudinal direction, smoothly changing density till the lateral boundaries. The change in cell dimension going outward (or inward) has a limit, indeed a cell can not be too smaller or too bigger compared to the adjacent ones. In order to verify this limit, the ratio between the dimension of two consecutive cells has to stay within a range:

$$0.9 \leq \frac{dx_1}{dx_2} \leq 1.1 \tag{4.38}$$

the fulfillment of this condition is necessary to avoid numerical instabilities. A quadratic function is used to obtain a suitable deformation, the parabola equation is the classic one:

$$y = a_1 \cdot x^2 + a_2 \cdot x + a_3 \ .$$

In order to compute the coefficients, first of all it is necessary to introduce the creation of the constant region:

$$x_{i-1} = x_c + (i-1) \cdot res - \frac{1}{2} res \qquad for\ i = 2, ...n_{cr} \tag{4.39}$$

where:

- x_c is the center position, half of the side dimension;
- *res* is the resolution, the "density" of cells in the center region;
- x_{cr} position where the constant region ends;
- n_{cr} is the index of position where the constant region ends, computed as:

$$n_{cr} = round\left(\frac{x_{cr} - x_c}{res}\right) \ .$$

Given the total number of grid points N_{TOT} of one of the directions and naming N_{CR} the number of cells in the constant region, the number of remaining cells for the parabolic region is:

$$N_{PR} = \frac{1}{2} N_{TOT} - N_{CR}$$

It is now possible to compute the coefficients of the parabola:

$$\begin{cases} a_3 = \dfrac{res}{L - \frac{1}{2}L_{CR}} \\ a_1 = \dfrac{1 - a_1 \cdot (1 + (N_{PR} - 1))}{(N_{PR} - 1)(N_{PR} - 2)} \\ a_2 = a_3 - a_1; \end{cases} \tag{4.40}$$

Once the coefficients are known, the equation that generates the grid points of the deformation is the following:

$$x_i = x_{cr} + \left(a_1 (i-1)^2 + a_2 (i-1) + a_3\right) \cdot (L - x_{cr}) \tag{4.41}$$

The points generated by the two cycles (4.39) and (4.41) only gives half points of the deformation. The final step is to save those points in a vector, invert it and unite the two vectors generating the grid deformation. Once the vector that contains all the positions of cells is generated, it is possible to verify if the deformation fulfills the condition in (4.38). If it is not satisfied, it is easy to adjust the deformation just by modifying only two parameters: the resolution (*res*) and the total number of grid points N_{TOT}. In the simulations of this thesis work, this kind of deformation is adopted for the y- and z-directions of the domain, as shown in figure 5.5.

4.7 MPI Code Parallelization

Parallel computation is the answer of a problem for Central Processing Unit (CPU) vendors at the turn of the century. In those years, CPUs reached a clock speed (the number of cycles per second a CPU performs) in the order of Giga-Hertz, which was a plateau in performances and hard to improve further. For this reason, manufacturers started to produce multiprocessing systems: more than one CPU is used within a single computer system, capable of running at the same time. This kind of architectures was first used in supercomputers since the 70s, only reaching the consumer market in the early 2000s. Some of the greatest benefits of these CPUs are the possibility of solving bigger problems, overcoming memory issues, and significantly reduce the calculation time.

Parallel computing is the simultaneous use of more processes for solving a computational problem. In order to do so, the problem has to be split into smaller tasks that are run at the same time by different processes. However, the decomposition of an algorithm is a non-trivial problem, sometimes even impossible. Tasks, indeed, need a communication between the processes, which requires a certain amount of time. The scalability of the parallel algorithm depends on the quantity of communication necessary: the lesser communication it needs, the

closer the scaling factor by running the algorithm in parallel will be to the number of processes used. There are two approaches for interaction among processes during the parallelization of tasks: the shared-memory and the message-passing. In the former all the processes have access to the same memory address, that they can read and write to, while in the latter each process has its own set of data that are exchanged through passing messages (a series of communication events).

In the message-passing parallelization the execution model is a Single Program Multiple Data (SPMD), namely every process runs the same program on his local memory: the code is the same but each processor behaves differently, depending on its data and its rank in the "hierarchy" of processes. For this reason, a communication between processes is needed. In this approach the cooperation of processes happens through a point-to-point interprocess communication: a process (called sender) sends the message to another process (the receiver) that receives this message. The MPI (acronym for Message Passing Interface) is a library interface specification for this model, a standard for developers and users. MPI is a programming tool that allows to manage a group of processes and the message exchange between them. The message is composed by:

- **source**: identifier of the sender process;
- **destination**: identifier of the receiver process;
- **communicator**: defines the relation between processes;
- **tag**: identifier of the message;
- **buffer**: data contained in the message;
- **datatype**: class of data in the message;
- **count**: number of data in the message.

The communication in MPI message passing can be synchronous or asynchronous. In the asynchronous one the process continues its computation after sending a message, even if the receiver has not received it. On the other hand, in the synchronous communication after a message is sent the execution waits for the message to be received. As stated above, all processes share the same code so it may happen that, if a send is immediately followed by a receive, the computation freezes. To avoid this situation, called "*deadlocks*", it is necessary to insert some control checks in order to organize send-receive in the correct sequence and only when it is required. For example, when the subroutine for writing the results is called, all processes has to send their data to the master, so they will read only send calls in the code. The master, which only has to receive data, will only execute the receive function, one for every process.

Concerning the communicator, in MPI the default one is the MPI_COMM_WORLD that assigns a number to each process from 0 to $N-1$ (where N is total number of processors). Despite its simplicity, a more intuitive organization of processes is employed. The code used in this work implements a Cartesian communicator, where a $N-$dimensional rank is assigned to each process, defining its position along the Cartesian axes, and arranged along those N orthogonal axes. This allows to decompose the physical domain into blocks, assigning each process to one of those blocks depending to the position in the previous decomposition. In this way the boundaries between processes corresponds to the ones between sub-domains. MPI allows to define sub-communicators, so for the Cartesian communication it is possible to manage a single Cartesian direction communication.

4.7.1 Parallel Scaling Performance: Strong Scaling

In order to estimate the scalability of the code, a scaling performance has been made by running a single simulation with different number of processors, each one running for 100 non-dimensional time steps and on a domain of $500 \times 120 \times 120$ total number of cells. The table 4.1 summarise the performance for each simulation, containing the CPU time and the percentage (of each CPU time) in relation to the simulation with only one process. The last column is the ratio between the computational load, tied to the volume, and the communication, tied to the surface, for each process. The volume considered is in terms of the number of points.

Processes	**CPU Time T(p)**	**T(1)/(p × T(p)) × 100**	**Vol/Sup**
$1 \times 1 \times 1 = 1$	1133	100	
$2 \times 1 \times 1 = 2$	638	89	48
$2 \times 2 \times 1 = 4$	475	60	34
$2 \times 2 \times 2 = 8$	492	29	27

Table 4.1: Simulations with increasing number of processes for the strong scaling

It is worth noticing that while the work of a single process decreases when more processes are involved, the total CPU time doesn't change much when using more than 4 processes. Despite of that, the effective time necessary for doing 100 time steps decreases anyway.

4.7.2 Weak Scaling

The Weak Scaling is another way of estimating the scalability of the code, but differs from the strong scaling in the number of points in a single process. Now each process has an almost constant number of points, which is $250 \times 60 \times 60$. The non-dimensional time steps simulated are still 100.

Processes	**Total Points**	**CPU Time T(p)**	**T(1)/T(p) × 100**
$1 \times 1 \times 1 = 1$	$250 \times 60 \times 60$	123	100
$2 \times 1 \times 1 = 2$	$500 \times 60 \times 60$	148	83
$2 \times 2 \times 1 = 4$	$500 \times 120 \times 60$	207	59
$2 \times 2 \times 2 = 8$	$500 \times 120 \times 120$	494	25

Table 4.2: Simulations with increasing number of processes for the weak scaling

In those simulations the computational load and the CPU time may only increase because of the growing number of total points, despite of this the total CPU time for a single process decreases. Both of these scalings shows that using more processes allows to reduce the total time necessary for simulations, which is worth it until a certain number of processes (obviously for a small number of them). This could also be caused by the virtualization of processors: in modern computers a "dual-core" CPU could split the two physical processors into further two, becoming a "quad-core" CPU, with the so-called "virtualization". In this case a simulation with eight processes is only slightly faster than using four processes, it is not twice faster as going from one to two processes. It would be necessary to use a machine with more physical processors installed. In conclusion, the maximum number of processors used for the simulations is 4, with the domain partition of $1 \times 2 \times 2$.

5. Code Validation

This chapter is devoted to the process of validation of the numerical schemes presented in the previous Chapter and adopted to solve the governing equations (Section 3.1). The first case study taken into account is a reproduction of Poiseuille's flow in a laminar condition. The second part is dedicated to the analysis of a turbulent round jet and its statistics, a configuration that has a flow behaviour similar to the wake generated by the body and the propeller of a ship.

5.1 Poiseuille's Flow

The Poiseuille's Flow is the first case solved for validating the code. Because of its simplicity, the simulation of this configuration is primarily focused on validating both the pressure solver (based on Shur complement) and the MPI parallelization of processors; for the same reason, the only parameter extracted from the simulation is the axial velocity. The theoretical solution is obtained by considering non-dimensional governing equations (NS) of a two-dimensional problem, in particular the x-direction momentum equation. Those equations are simplified by considering that vertical velocity is zero ($v = 0$), x-derivatives of velocity has to be null (for the homogeneity in this direction) and pressure gradient is constant. The momentum equation reduces to:

$$\frac{\partial^2 u}{\partial y^2} = Re\ \frac{\partial p}{\partial x}; \tag{5.1}$$

the solution of which is obtained by imposing velocity at boundaries ($u(0) = 0;\ u(1) = 0$):

$$u(y) = \frac{Re}{2}\frac{\partial p}{\partial x}\left(y^2 - y\right). \tag{5.2}$$

The simulation has been made with a three-dimensional domain of $20 \times 80 \times 20$ cells (x,y,z directions) composed of a uniform grid, while its size is, in non-dimensional units, $3 \times 1 \times 1$. The Boundary Conditions used for velocity and pressure are:

Boundary Conditions	Velocity	Pressure
Inflow Conditions	Neumann	Neumann
Outflow Conditions	Neumann	Neumann
Left & Right Conditions	Neumann	Neumann
Upper & Lower Conditions	Laminar BL	Neumann

Table 5.1: Boundary Conditions for Poiseuille simulation

The Neumann condition is equivalent to impose a null derivative in the orthogonal direction of the boundary plane, *i.e.* the same values for boundary and penultimate cell. In the Laminar Boundary Layer (BL) condition the velocity component orthogonal to the boundary face is imposed null, while the other two velocity components have the same value but opposite sign to the ones of the penultimate cell.

The parameters for the analytical solution are $Re = 100$ and $\partial p/\partial x = -0.08$, and the comparison between simulation results and theoretical solution is shown in 5.1. In 5.2 is presented the axial velocity between the two walls, which is a slice of the domain with normal parallel to the z-axis.

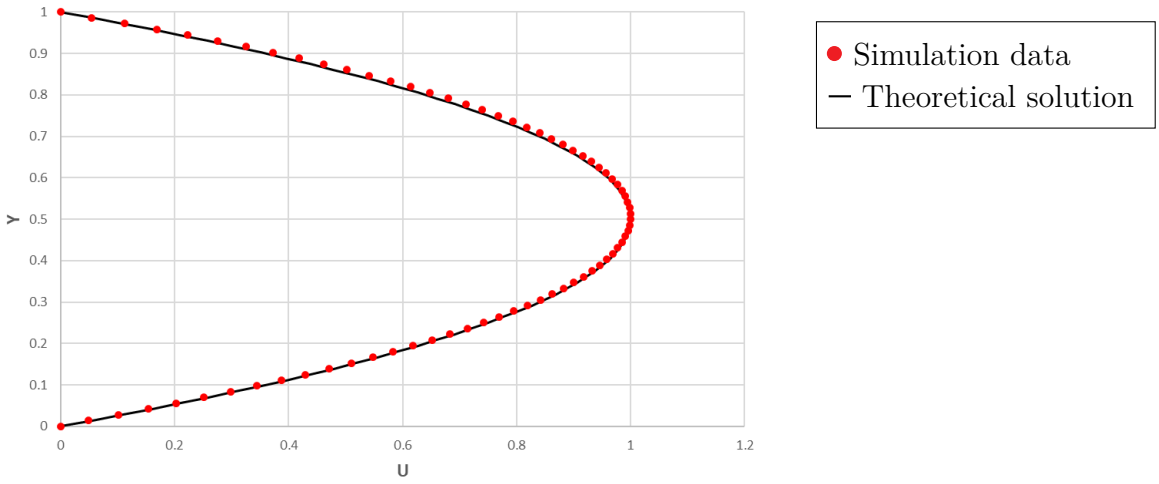

Figure 5.1: Plot of axial velocity of Poiseuille Flow

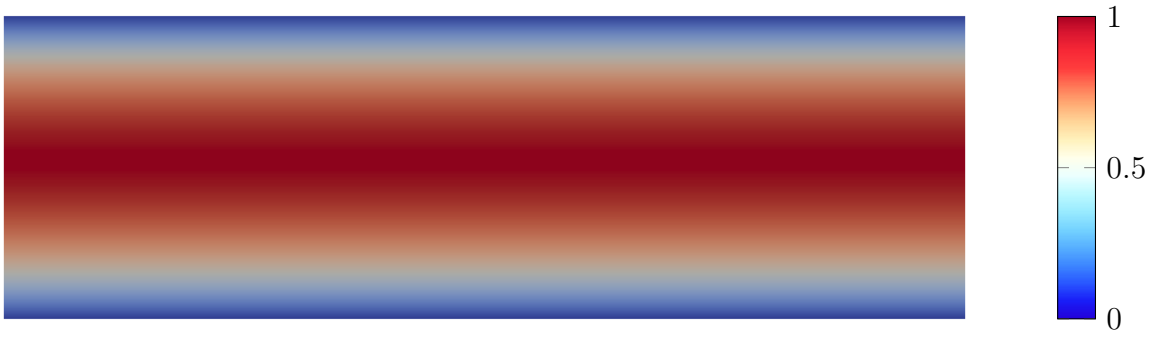

Figure 5.2: Axial velocity of Poiseuille flow

A similar scaling as the one presented in Section 4.7.1 has been made for the simulation of the Poiseuille's flow. The two kind of scaling (strong and weak) have been redone with similar considerations: for the strong scaling two kind of grids ($100 \times 100 \times 100$ and $200 \times 200 \times 200$) has been used, while for the weak scaling the number of points for a single process has been maintained constant ($100 \times 100 \times 100$). The three simulations with the increasing number of processes are presented in tables 5.2,5.3,5.4:

Processes	**CPU Time T(p)**
$1 \times 1 \times 1 = 1$	43.2
$2 \times 1 \times 1 = 2$	32.23
$2 \times 2 \times 1 = 4$	23.3
$2 \times 2 \times 2 = 8$	28.1

Table 5.2: Strong scaling for Poiseuille flow simulation, $100 \times 100 \times 100$ grid

Processes	CPU Time T(p)
$1 \times 1 \times 1 = 1$	554.4
$2 \times 1 \times 1 = 2$	371.4
$2 \times 2 \times 1 = 4$	291.5
$2 \times 2 \times 2 = 8$	298.7

Table 5.3: Strong scaling for Poiseuille flow simulation, $200 \times 200 \times 200$ grid

Processes	CPU Time T(p)
$1 \times 1 \times 1 = 1$	43.2
$2 \times 1 \times 1 = 2$	63.2
$2 \times 2 \times 1 = 4$	126
$2 \times 2 \times 2 = 8$	297

Table 5.4: Weak scaling for Poiseuille flow simulation, $100 \times 100 \times 100$ points for process

As previously stated in Section 4.7.2, using eight virtual processes, rather than four, is not as much convenient as doubling physical processors. This is caused by the virtualization process, that does not always guarantee an improvement in performances. In order to verify the effect of the processors virtualization on lack of improvement in performance, a strong scaling analysis has been conducted on Politecnico di Milano DAER machine "Castore". The results are presented in table 5.5.

Processes	CPU Time T(2)/T(p)
$2 \times 1 \times 1 = 2$	1
$2 \times 2 \times 1 = 4$	1.77
$2 \times 2 \times 2 = 8$	2.77
$4 \times 2 \times 2 = 16$	5.46
$4 \times 4 \times 2 = 32$	7.86

Table 5.5: Strong scaling for Poiseuille flow simulation, on Castore machine with $400 \times 400 \times 400$ grid

It is evident that, comparing results from tables 5.2 and 5.5, doubling the number of processors using virtualization leads to a worse scalability performance. On the other hand, doubling the number of physical processors leads to a continuous improvement in performance.

5.2 Turbulent Round Jet

The turbulent round jet is a free-shear, axisymmetric flow that develops away from walls,. From a physical point of view two regions can be identified:

- Potential core: this is the first region of the jet, in which the flow is laminar and is surrounded by the annular mixing layer. Such mixing layer tends to grow up moving far from the injection zone, causing the transition of the potential core from laminar to turbulent. The section of transition and consequently the extension of the potential core region vary depending on the value of Re.
- Pure Jet: this is the purely turbulent region of the jet, characterized by the self-similarity behaviour of the centerline mean axial velocity and the jet half-width.

In particular, the self-similar profile of the centerline mean axial velocity has the following formulation (Pope [2000]):

$$\frac{U_0(x)}{U_j} = \frac{B_s}{(x - x_0)/D_{jet}} \tag{5.3}$$

- U_0: centerline mean axial velocity
- U_j: maximum axial velocity of the inlet profile
- B_s: empirical constant for similarity
- x: axial coordinate
- x_0: virtual origin
- D_{jet}: jet diameter

Analogously to the centerline mean axial velocity, also the jet half width is characterized by a self-similar trend. In particular, the jet half width is defined as the location in radial direction, where the mean axial velocity is halved with respect to the centerline mean axial velocity. The self-similar profile of the jet half width is linear and can be expressed as (Pope [2000]):

$$r_{1/2} = S \cdot \frac{(x - x_0)}{D_{jet}} \tag{5.4}$$

- $r_{1/2}$: jet half width
- S: jet spreading rate

5.2.1 Problem geometry and Setup

The LES simulations of a turbulent round jet, in this work, provide the jet diameter D_{jet} as the reference length of the domain geometry. Considering the Cartesian coordinate system (x, y, z) the computational domain develops into $30D_{jet}$ along the axial direction x, while $11D_{jet}$ both in y and z directions. The pipe jet at the inlet section is represented by a circular area of a reference diameter $D_{jet} = 1$, in order to have a non-dimensional geometry, which centre is located at the point of coordinates $C(0, 5.5D_{jet}, 5.5D_{jet})$.

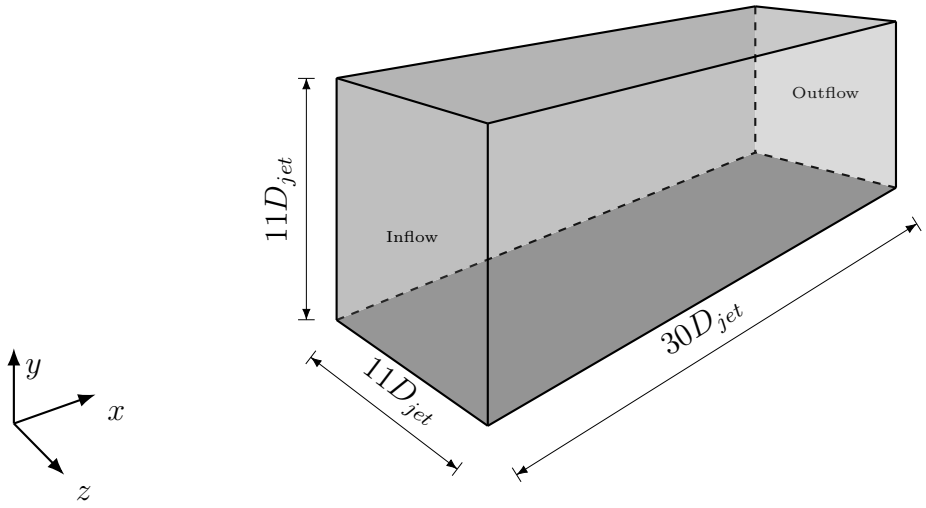

Figure 5.3: A schematic of the round jet geometry setup of simulations

The setup of the simulations is analogous to the ones presented in Ilyushin and Krasinsky [2006], which results are taken into account, together with the results of the studies by Boersma et al. [1998] ($Re = 25,000$),Hussein et al. [1994] ($Re = 95,500$) and Wygnanski and Fiedler [1969] ($Re \approx 10^5$), as reference solutions. The main parameters of the simulations are summarized in the following table:

$\mathbf{Re} = \frac{UD_{jet}}{\nu}$	25,000	
Boundary Conditions	**Velocity**	**Pressure**
Inflow Conditions	Inlet Velocity Profile	Neumann
Outflow Conditions	Developed Flow	Neumann
Lateral Conditions	Free-shear Flow	Neumann

Table 5.6: Setup parameters of turbulent round jet simulations

The boundary conditions of the simulations required a deeper insight:

- Inflow conditions: as regards the inlet jet velocity profile, for the axial velocity profile an hyperbolic tangent law has been adopted

$$U_{in}(r) = \frac{1}{2}U_j \left[1 + \tanh\left(\frac{R_{jet} - r}{2\delta_*}\right)\right] \tag{5.5}$$

  where $r = \sqrt{y^2 + z^2}$ is the radial coordinate, $R_{jet} = D_{jet}/2$ is the jet radius, $U_j = 1$ is the non-dimensional maximum axial velocity component and $\delta_* = 0.0024$ is the initial momentum thickness, different from Ilyushin and Krasinsky [2006] work, in which $\delta_* = 0.0048$ is extrapolated from PIV data (Alekseenko et al. [2005]), to have a stronger gradient of the inlet velocity profile. Moreover, it is worth to underline that, in the present work, no axial velocity fluctuations have been imposed at the inlet. However, to reproduce the effect of turbulent pulsations a circular bluff body of radius $R_{bluffbody} = 2.71D_{jet}$, concentric to the pipe jet, is located at the inlet. External to the bluff body, a co-flow non-dimensional constant axial velocity $U_e = 0.037$ (for details consult Ilyushin and Krasinsky [2006]).

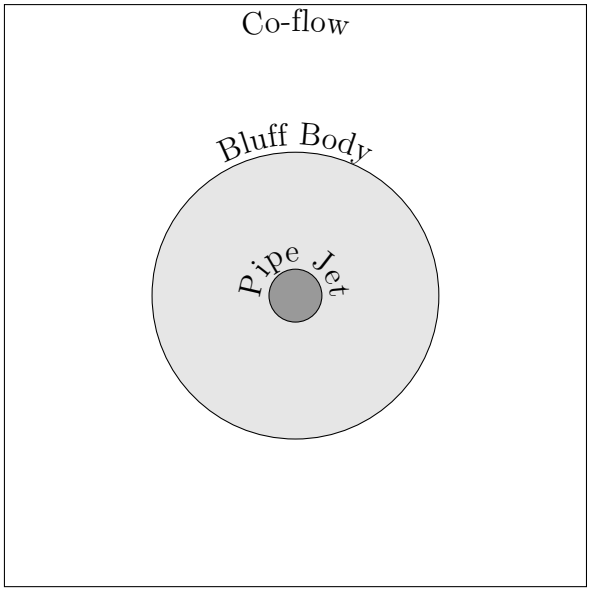

Figure 5.4: Inlet section of turbulent round jet simulations

  On the contrary the velocity components in y and z directions are imposed to zero, while concerning the pressure a Neumann's boundary condition has been applied.

- Outflow Conditions: for the velocity a condition for developed flows has been applied. It consists in applying a Neumann's boundary condition for the axial velocity component,

while the velocity in y and z direction is set as null. The boundary pressure is governed by a Neumann's condition as well as at the inflow.

- Lateral Conditions: the boundary domain faces in y and z directions are characterized by the use of a modified free-shear flow condition. In particular, for boundary faces, which plane is perpendicular to y-axis and z-axis:

$$\begin{cases} \boldsymbol{u} \cdot \boldsymbol{t} = u_{inf} \\ \boldsymbol{u} \cdot \boldsymbol{n} = 0 \end{cases},$$

where $\boldsymbol{t}$ and $\boldsymbol{n}$ are respectively the unit vectors tangent and normal to the boundary plane. The pressure, in analogy to inflow and outflow conditions , is governed by a Neumann's boundary condition.

Furthermore, it is worth to highlight that shear-flow lateral conditions and the developed flow in outflow prevent the reflection of pressure waves from the boundaries, as confirmed by the results presented in Section 5.2.3.

Concerning the initial conditions over the entire domain, the pressure is imposed as uniform and equal to zero, while for velocity the hyperbolic tangent law is applied all along the axial length of the domain, instead the region outside the jet is characterized by the co-flow axial velocity, except for the inflow region of the bluff body. The main reason of this particular choice is to satisfy the mass conservation principle in the computational domain, otherwise the simulation would diverge. On the contrary, the velocity components in y and z directions are initialized to zero in the entire domain.

5.2.2 Mesh generation

The type of flow analysed influences the mesh grid structure of the simulations. In the present work, for turbulent round jet simulations a Cartesian grid is employed. In order to properly represent the strong velocity gradient of the jet in the hyperbolic tangent law (see equation (5.5)) the computational grid is refined at the center of the xy plane in a box $2D_{jet} \times 2D_{jet}$ with a constant resolution, while the region external to the box is characterized by the parabolic grid deformation presented in Section 4.6. On the contrary, the numerical grid is not deformed in the axial direction. In figures 5.5 and 5.6 is presented a visualization of the grid configuration $500 \times 120 \times 120$ (see table 5.7).

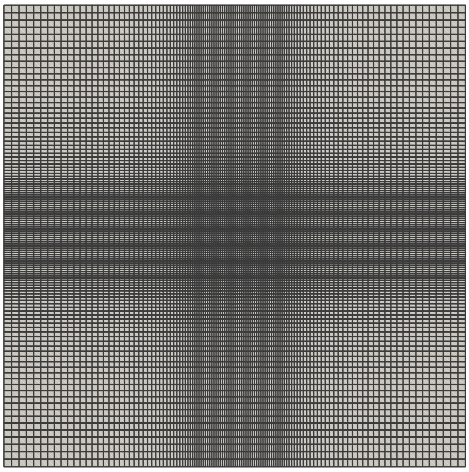

Figure 5.5: Mesh Grid in y-z plane for turbulent round jet simulations, configuration $500 \times 120 \times 120$

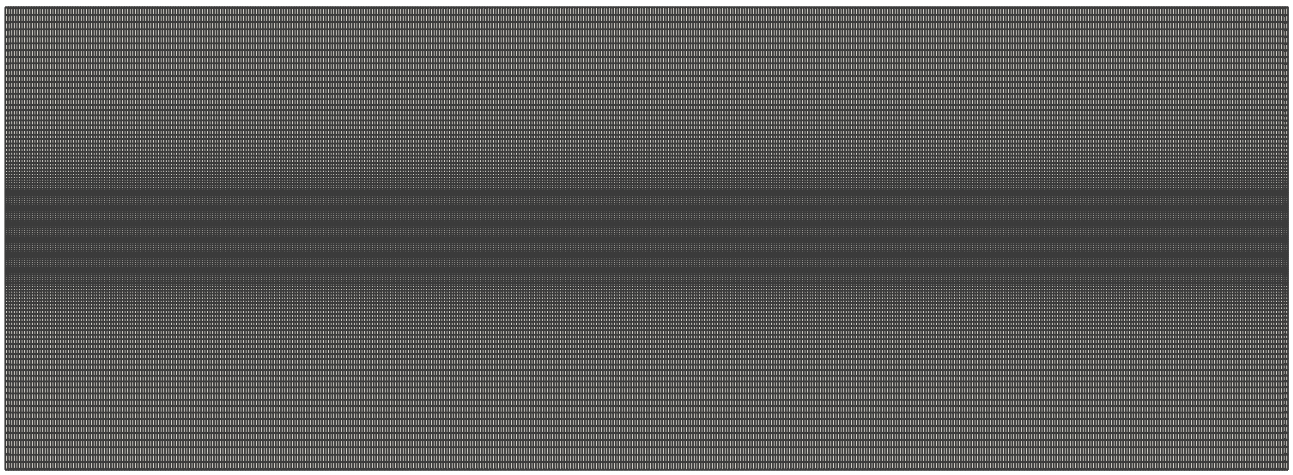

Figure 5.6: Mesh Grid in x-y plane for turbulent round jet simulations, configuration $500 \times 120 \times 120$

Throughout the process of code validation for the turbulent round jet case two mesh configurations have been analysed, which parameters are summarised in the following table:

ΔX_{min}	ΔY_{min}	ΔZ_{min}	X Cells	Y Cells	Z Cells	Total Cells number
0.075	0.06	0.06	400	100	100	$4 \cdot 10^6$
0.06	0.05	0.05	500	120	120	$7.2 \cdot 10^6$

Table 5.7: Mesh Grid configurations for the turbulent round jet

Note: from now onwards, "Max Res" will be used referring to the minimum cell dimension in the mesh, *i.e.* the maximum grid resolution.

5.2.3 Results

In order to test the quality of the code on representing the turbulent round jet, the attention has been focused on the self-similarity behaviour of the flow. Furthermore, the LES accuracy has been studied analysing a grid convergence with the configurations of table 5.7.

A first look is given to the self-similarity of the jet axial mean centerline velocity (U_0), whose plot is represented in figure 5.7.

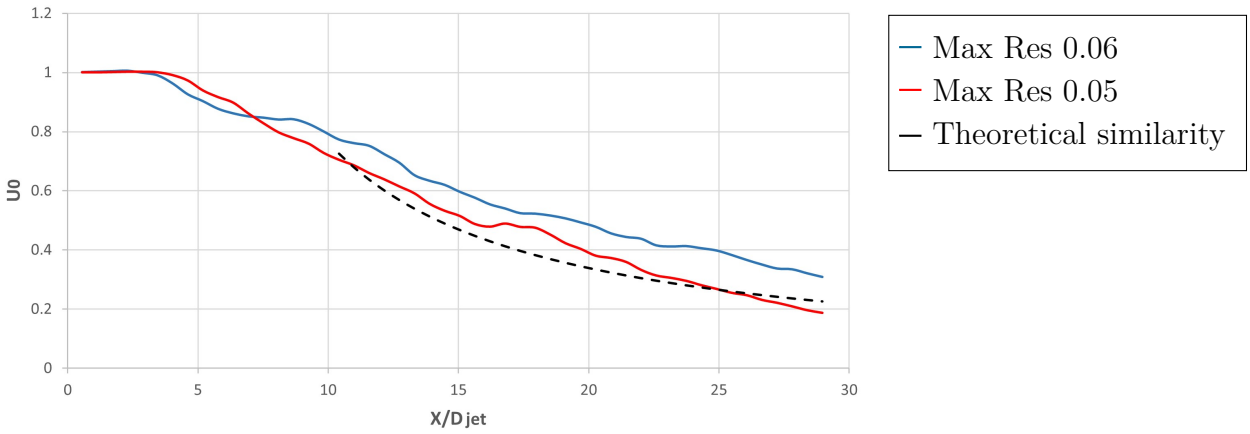

Figure 5.7: Grid convergence of the axial centerline velocity. A comparison with the jet self-similarity.

It is evident from the figure 5.7 that the simulation with a larger total cells number reproduces more precisely the variation $U_0 \sim x^{-1}$. However, it would have been better to make longer simulations for smoother velocity profiles, not performed for lack of computational resources. Moreover, the data of the simulations of the present work better fit into the similarity law of the axial velocity component with the empirical constant $B_s = 6.1$ and the virtual origin $x_0 = 2$, while the experiment of Hussein et al. [1994] reported $B_s = 5.8$ and $x_0 = 4$ and in the

experiment of Wygnanski and Fiedler [1969] $B_s = 5.7$ and $x_0 = 3$ (the different similarity laws are compared in figure 5.8). A smaller value of the virtual origin in the data of this thesis is probably caused by the presence the circular bluff body at the inflow, which anticipates the location of the transition point from laminar to turbulent flow.

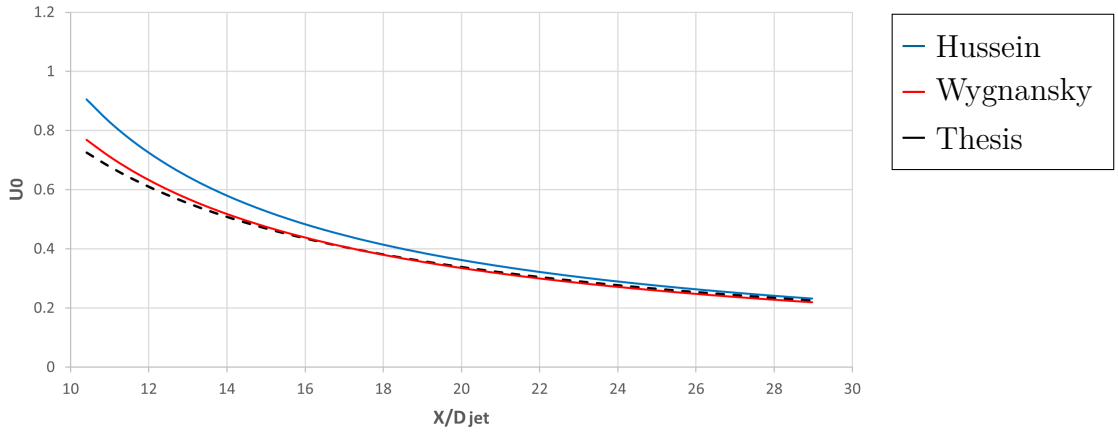

Figure 5.8: A comparison of the jet axial velocity similarity law.

The self-similarity of the jet in the axial direction has been also investigated in the jet half width.

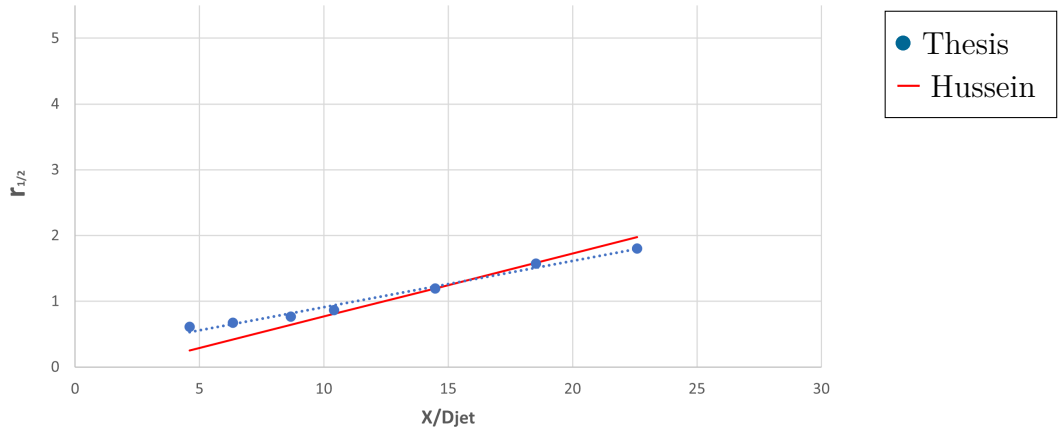

Figure 5.9: Development of the jet half width in the axial direction

The simulation with a better grid resolution gives a clear linear trend of the jet half width, consistent with the equation (5.4) presented in Section 5.2. In detail, the data extrapolated are located on a straight line of spreading rate $S = 0.0704$, with a coefficient of determination $R^2 = 0.9852$, which indicates how strong is the linear relation for a set of data. Differently,

the study of Hussein et al. [1994] reported a spreading rate $S \equiv 0.095$, with a difference in the conical divergence of the jet of $\sim 1°$, with respect to the simulations of the present work. This small difference can be caused both by the presence of a co-flow axial velocity, external to the jet, and by the Smagorinsky subgrid model, which is a dissipative model that neglects the backscatter process. A larger dissipation of the subgrid-scale model and the absence of backscatter, not allowing the energy transfer from smallest to largest scales, prevents the generation of a larger shear flow, with a smaller spreading rate of the jet half width. The pure jet region is characterized by a self-similarity behaviour of the jet velocity variables in radial direction. The present study is focused on analysing the statistics of axial and radial velocity components in two cross sections along the axial direction. First of all, the radial profile of the axial velocity component is taken into account in figures 5.10 and 5.11, comparing it with the statistics from Ilyushin and Krasinsky [2006].

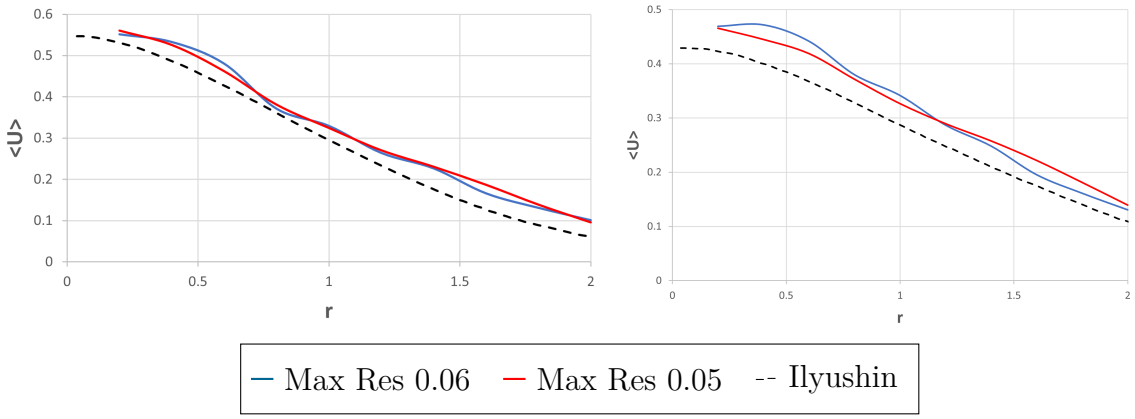

Figure 5.10: Radial profile of the axial velocity at $x/D_{jet} = 14.5$ (left) and $x/D_{jet} = 18.5$ (right)

It is worth noticing that Ilyushin and Krasinsky [2006] data are taken in $x/D_{jet} = 12$ and $x/D_{jet} = 16$, which are the locations where data from the article better match with our simulations. This could be due to a different extension of the jet potential core. A similar consideration can be made with the comparison between the self-similar behaviour of the present work statistics with the ones from the DNS data of Boersma et al. [1998] and LDA data of Hussein et al. [1994]. In particular, the similarity variable η is defined as:

$$\eta = \frac{r}{(x - x_0)} \tag{5.6}$$

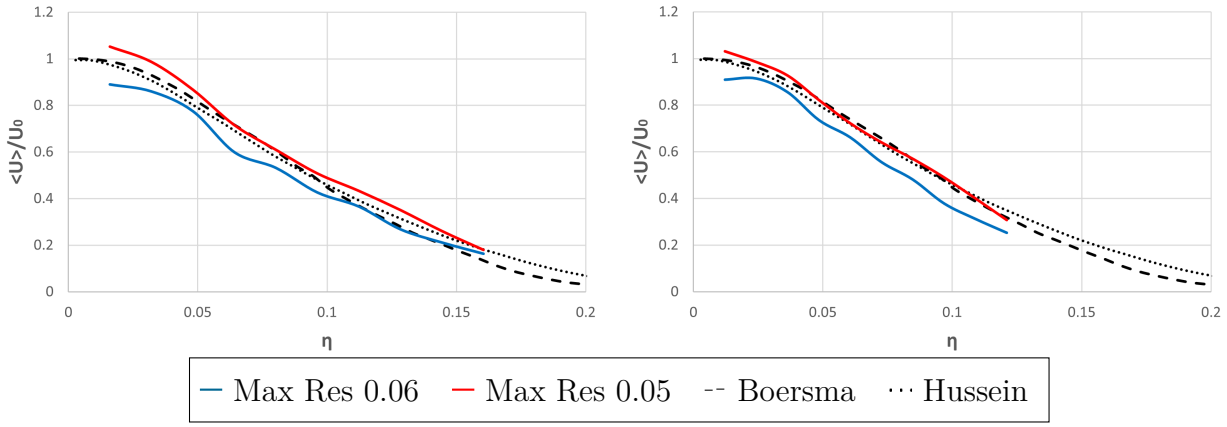

Figure 5.11: Radial profile of the axial velocity at $x/D_{jet} = 14.5$ (left) and $x/D_{jet} = 18.5$ (right) - with η as abscissa

It is evident from figure 5.11 that the simulation conducted with a maximum grid resolution of 0.05 fits very well with the data of Boersma et al. [1998] and Hussein et al. [1994].

Concerning the axial velocity of the jet, a further insight is given by the study of the turbulence intensity $u\prime/ < U >$, defined as the ratio between of the axial velocity root mean square (rms) $u\prime$ and the mean axial velocity $< U >$, presented in figure 5.12.

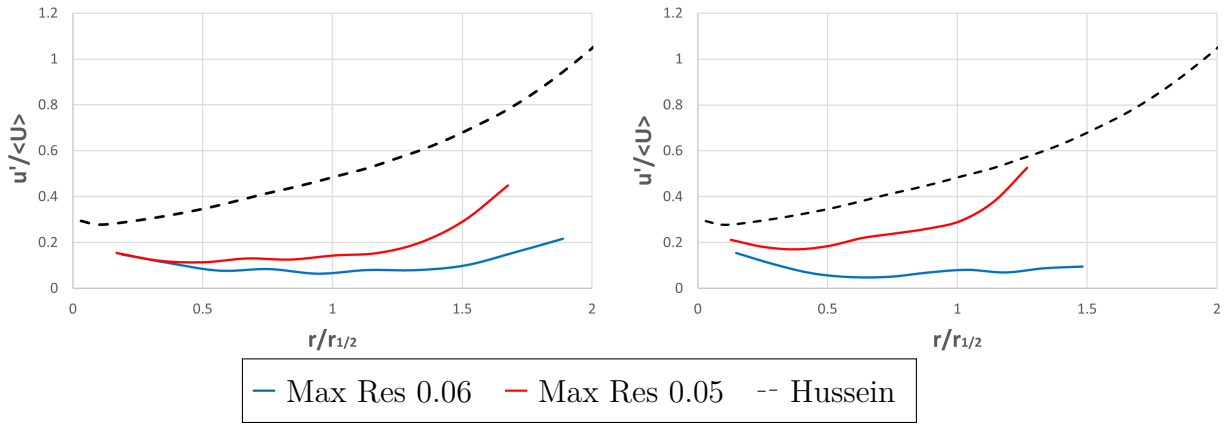

Figure 5.12: Radial profile of the axial turbulence intensity at $x/D_{jet} = 14.5$ (left) and $x/D_{jet} = 18.5$ (right)

The graphs in figure 5.12 highlight that the trend of data from the experiment by Hussein et al. [1994] is similar to the one of this work. However, the turbulence intensity values are quite different, since the modelled sgs stresses are represented by a traceless tensor and because of the use of a dissipative LES model as Smagorinsky model.

The cross sections in the pure jet region reveal, as shown in figure 5.13, a self-similar behaviour of the radial velocity component in accordance to the data assumed as reference solution. The grid convergence and the accuracy of the simulations is tested also analysing the radial profile of the radial velocity component in comparison with the simulations of Ilyushin and Krasinsky [2006], reported in figure 5.14.

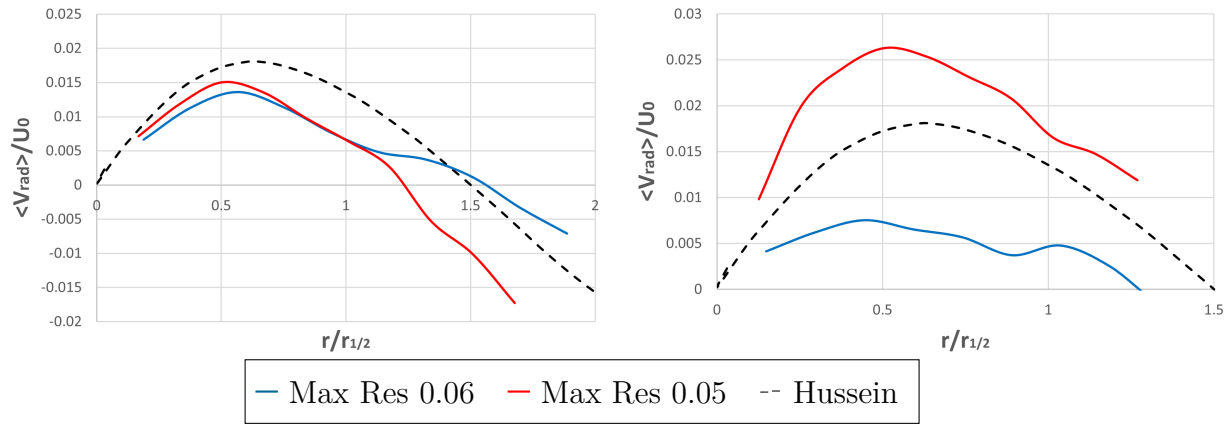

Figure 5.13: Similarity in radial direction of V_{rad} in cross section located at $x/D_{jet} = 14.5$ (left) and $x/D_{jet} = 18.5$ (right)

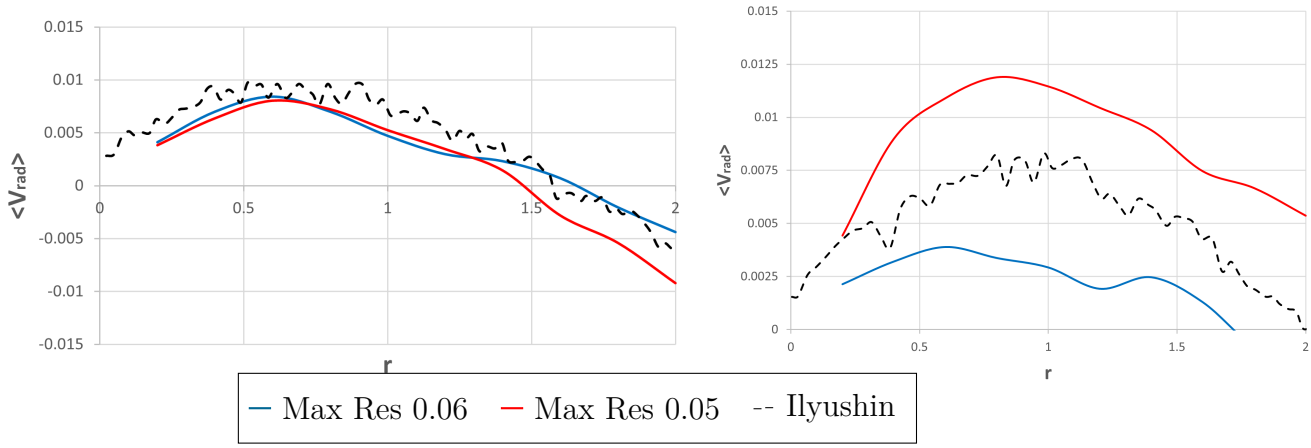

Figure 5.14: Radial profile of V_{rad} at cross section located at $x/D_{jet} = 14.5$ (left) and $x/D_{jet} = 18.5$ (right)

It is worth to notice how the radial velocity component tends to become negative for radius coordinates larger than a threshold value, that varies along the axial direction, confirming the entrainment process by the annular mixing layer of the jet.

In conclusion, figures 5.15 and 5.16 represent different visualisations of the jet vortex structures, in which it is clear the linear conical divergence of the jet and the limited extension of the potential core due to the anticipated transition section caused by the circular bluff body at the inlet.

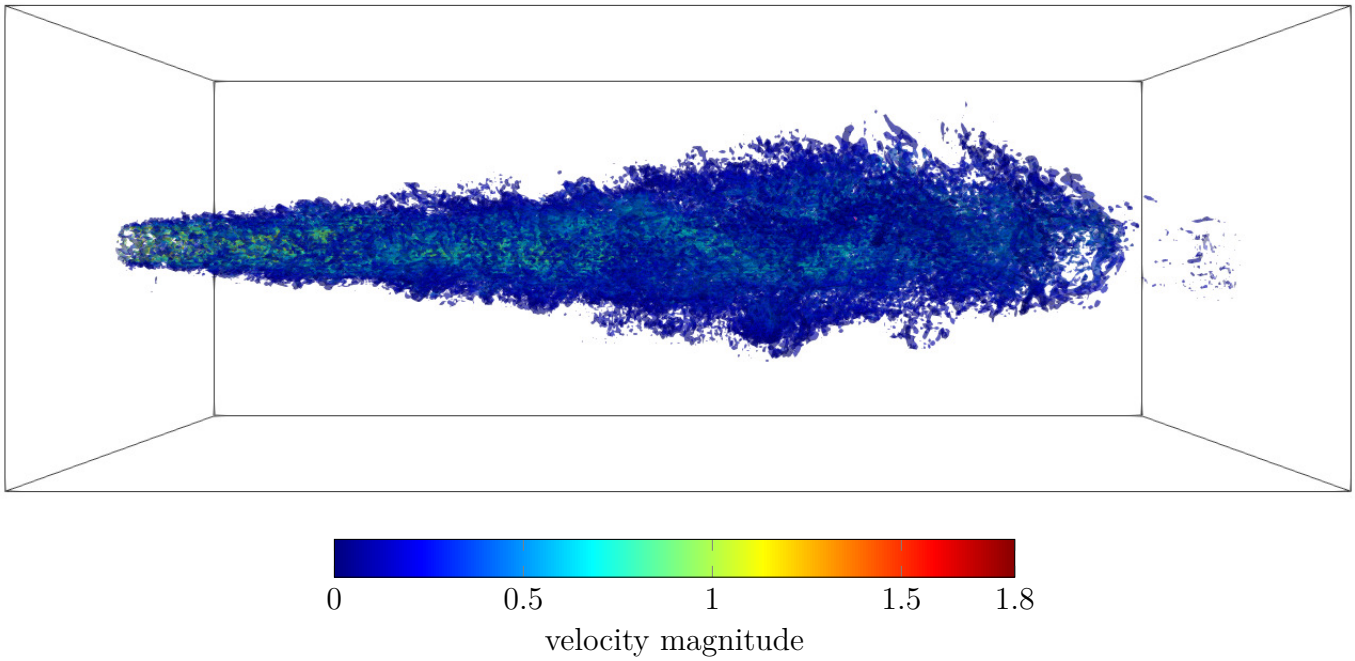

Figure 5.15: Iso-surfaces of $Q-criterion = 0.4$ for eddies identification, coloured with velocity magnitude

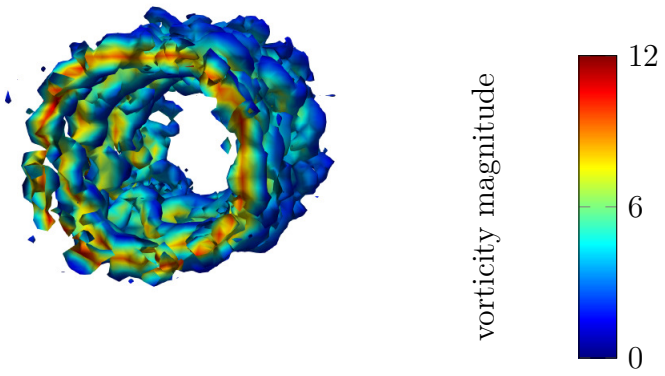

Figure 5.16: Instability of the vortex rings in the mixing layer surrounding the potential core. Iso-surfaces of $Q - criterion = 0.5$ coloured with vorticity magnitude

6. Ocean Liming Simulations

This chapter presents in detail the discussion about the results of slaked lime discharge simulations. In particular, different configurations of discharge are simulated. Firstly, the present work focuses its attention on calcium hydroxide dilution in the wake of a ship propeller, modelled as explained in Section 3.3. The discharge of $Ca(OH)_2$ is simulated with two layouts: single injection orifice and double injection orifices. These first simulations allow to better understand the impact of the propeller wake on the reaction kinematics between calcium hydroxide and water and the consequent local pH variations. However, considering the only wake of the propeller makes the study limited, with an ideal environment of simulation further away from a real case.

Therefore, the second part of the chapter is dedicated to the presentation of the results of simulations with the addition of a bluff body at the inlet domain face. Such configuration, approximately, simulates the wake of ship body that influences the propeller wake and dilution of slaked lime, making the case study more complete.

6.1 Slaked lime discharge in propeller wake

As previously introduced in this chapter, the first simulations of slaked lime discharge provide the presence, in the computational domain, exclusively of the propeller. This choice enables to analyse the behaviour of propeller model and the impact of its wake on $Ca(OH)_2$ dilution process.

6.1.1 Problem geometry and Setup

The LES simulations of the ship propeller with the injection of slaked lime are conducted with a setup analogous to that of turbulent round jet simulations, presented in Section 5.2. The parameters of the simulations in real dimensions, used in the adimensionalisation process of flow variables and geometry, are summarized in the following table:

Propeller	
Diameter	9.8 m
ω	60 rpm
J	0.12 - 0.6
Slaked Lime	
Mass Flow Rate	100 - 7800 kg/s
Initial Concentration	85.6 kg/m^3
Initial Particle Diameter	50 μm
Injection Diameter	0.86 m
Particle Density	2240 kg/m^3
Seawater Density	1024.75 kg/m^3
Seawater Dynamic Viscosity	$1.08 \cdot 10^{-3}$ $Pa \cdot s$

Table 6.1: Simulation parameters in real dimensions

The domain geometry is identical to that of figure 5.3, with a reference diameter of the propeller $D_{prop} = 1$ for adimensionalisation. The propeller is located at 3 diameters from the inflow, in order to limit the influence of the inflow conditions and has a non-dimensional rotational velocity of $\omega = 5.13$. It is important to underline that for lack of time resources in the simulations of $Ca(OH)_2$ single injection with J=0.12 the propeller has been located at 5 diameters from the inflow. In order to have a clear comparison with the other simulations, its data have been translated back of 2 diameters in axial direction. Such choice is justified in Sections 6.1.3,6.1.4.

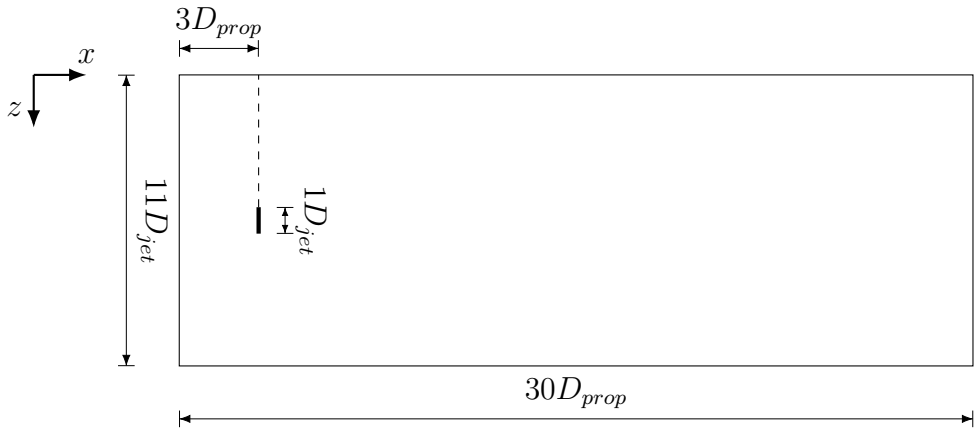

Figure 6.1: Problem geometry for propeller simulations

As regards boundary conditions for velocity components and pressure, they have already been presented in table 5.6 at Section 5.2. However, at the inflow the axial velocity component

is a uniform, constant profile of value $u(0, y, z) = 1$ and a Reynolds number $Re = 25,000$. The low Re number simulated is given by lack of computational resources. For the initial conditions both the pressure and the velocity are imposed as uniform over the entire domain. In particular, the pressure and velocity components in y and z directions are initialized as null, while the axial velocity component is imposed to one.

Concerning the slaked lime discharge, the injection orifice has a diameter $D_{inj} = 0.88D_{prop}$ located at the inlet face with center at point of coordinates $(0, 5.25D_{prop}, 5.5D_{prop})$ for single injection layout and centers of coordinates $(0, 5.5D_{prop}, 5.25D_{prop})$,$(0, 5.5D_{prop}, 5.75D_{prop})$ for double injection. $Ca(OH)_2$ is injected with a non-dimensional velocity $u = 0.0128$ for single injection and $u = 0.0064$ for double injection, that reproduce a lime mass flow rate of 100 kg/s for a first case and with a non-dimensional velocity $u = 1$, which simulates a lime mass flow rate of $7,800$ kg/s (single injection) and $15,600$ kg/s for the second case study. About the initial and boundary conditions, the slaked lime concentration and particle radius are imposed as zero over the entire domain, except the injection orifice at the inlet, while Neumann conditions are applied at the boundaries, excluding the inlet, both for concentration and particle radius. Similar considerations can be done for seawater pH, which is initialized as equal to the reference initial value $pH_0 = 8.12$ over the entire domain.

6.1.2 Mesh Generation

Since the propeller wake behaves, except for swirl addition, similarly to the turbulent round jet, the simulations are conducted with the same computational grid configuration presented in Section 5.2.2. A refined box of $2D_{prop} \times 2D_{prop}$, in y and z directions, contains the wake of the propeller. Outside the refinement box, the grid is made coarser in y and z directions by the parabolic grid deformation algorithm, presented in Section 4.6. On the contrary, the computational grid is uniform in axial direction, with the same resolution of the refinement box. In light of the results obtained by the grid convergence of turbulent round jet simulations, it was decided to employ the second mesh layout, presented in table 5.7, with a more refined maximum grid resolution.

ΔX_{min}	ΔY_{min}	ΔZ_{min}	X Cells	Y Cells	Z Cells	Total Cells number
0.06	0.05	0.05	500	120	120	$7.2 \cdot 10^6$

Table 6.2: Mesh Grid configuration for propeller wake simulations

6.1.3 Propeller Wake

The operating regime of the ship propeller is a fundamental factor that affects the dilution process of slaked lime in seawater. For this reason, in the present work the propeller working

has been studied in two configurations of advance ratio, presented in Section 3.3. The following paragraphs are dedicated to the presentation of the main flow parameters in the wake of the propeller to assess the physical and mathematical model employed in the two operational regimes.

First of all an overview of the modelled five blades of KP505 propeller is given in figure 6.2, that represent the axial velocity distribution on a cross section of the propeller:

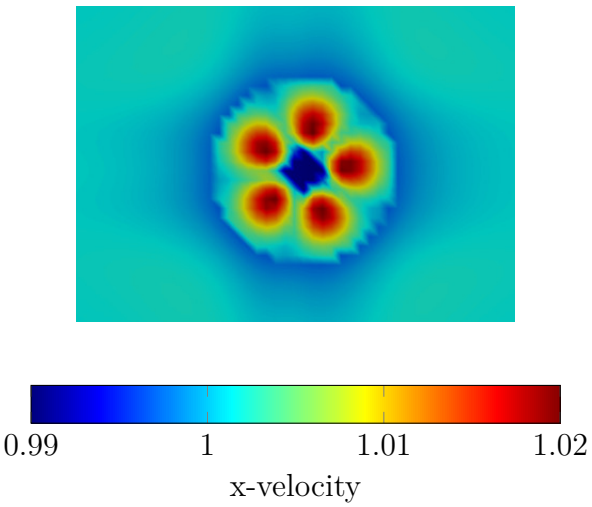

Figure 6.2: Axial Velocity distribution on a cross section at $x/D_{prop} = 3$ with J=0.6

From figure 6.2 it is evident the presence of five blades, with larger axial velocity values in correspondence of each of them. On the contrary, the axial velocity values in the propeller axis are < 1; namely, slower than the unperturbed flow. As stated in Section 6.1.1, the propeller has been simulated in two advance ratio configurations, that allow to better understand the behaviour of $Ca(OH)_2$ discharging. Before studying the slaked lime data, it is interesting to focus on the flow variables across the propeller and its wake. In this work, the data has been collected on three lines, located in different positions, that cross the entire domain.

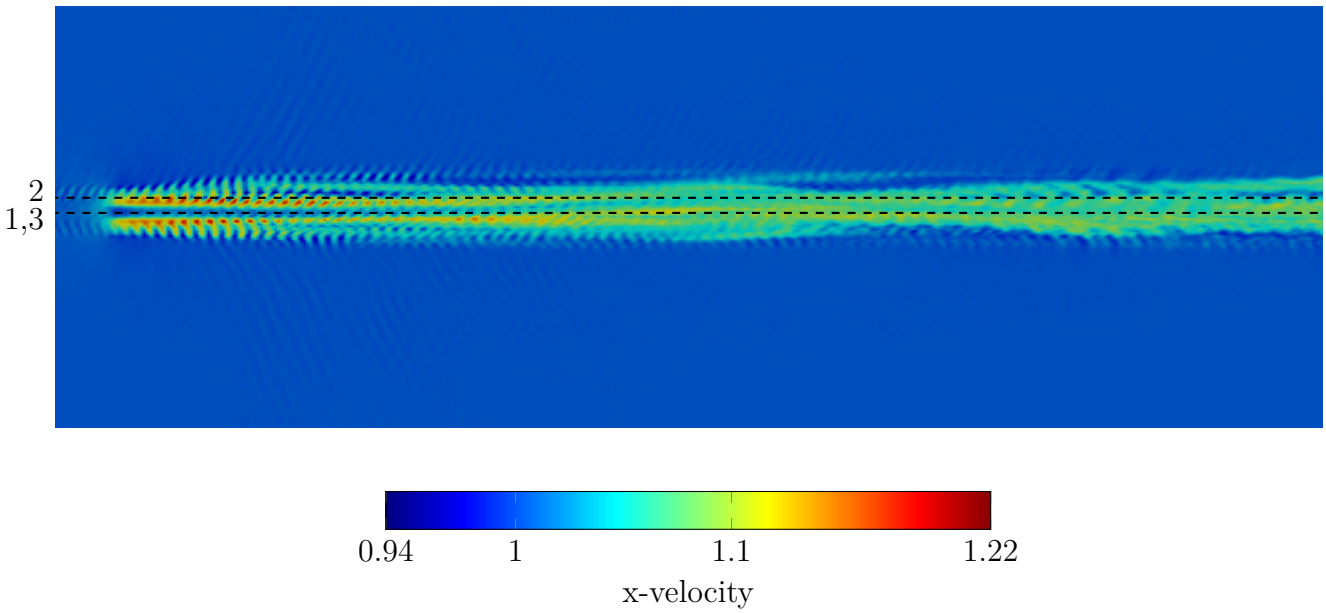

Figure 6.3: Axial velocity of propeller wake in longitudinal section with J=0.6

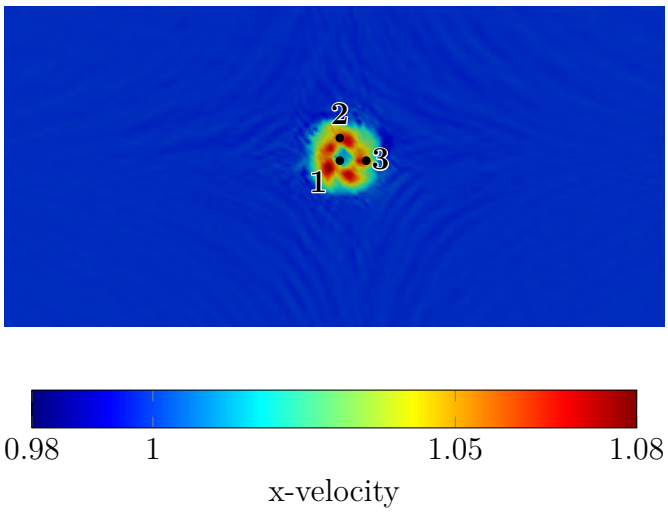

Figure 6.4: Axial Velocity of propeller wake on cross section at $x/D_{prop} = 3$ with J=0.6

As previously introduced the data of the case J=0.12 have been translated of 2 diameters in axial direction, in order to have a coherent comparison with the case J=0.6. This is possible because at the inflow there are neither a bluff body or velocity fluctuations imposed, hence in the region between the inlet face and the propeller does not change. It is worth noticing that, given the three lines in figures 6.3 and 6.4, along line 2 it is possible referring to V as radial

velocity component and to W as tangential velocity component; viceversa, along line 3 the opposite is true. Concerning the data acquired at the centerline of the propeller wake (line 1 in figures 6.3,6.4), the first comparison between the two operating regimes is made considering the pressure jump given by the propeller (figure 6.5).

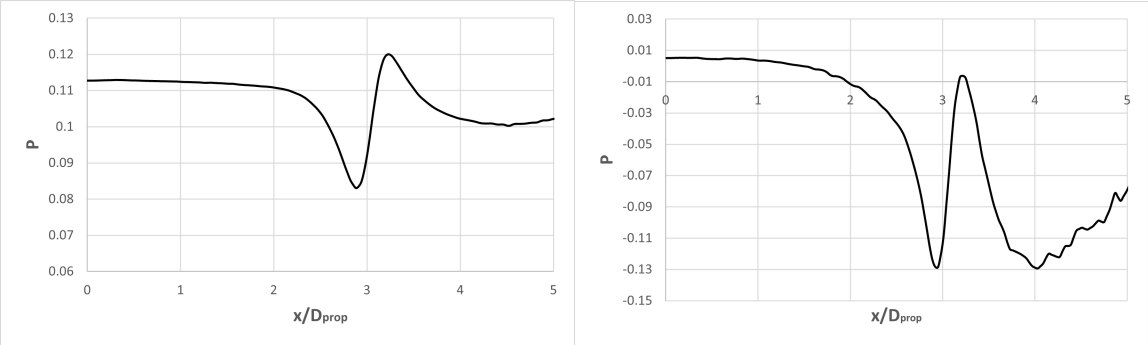

Figure 6.5: Instantaneous pressure jump of propeller wake centerline with J=0.6 (left) and J=0.12 (right) at about t=90

The case of J=0.12 provides a larger pressure jump to the flow (right plot of figure 6.5), as consequence of quite larger hydrodynamic coefficients with respect to the case of J=0.6 (see tables 3.1,3.2). Similar considerations can be done with the three velocity components:

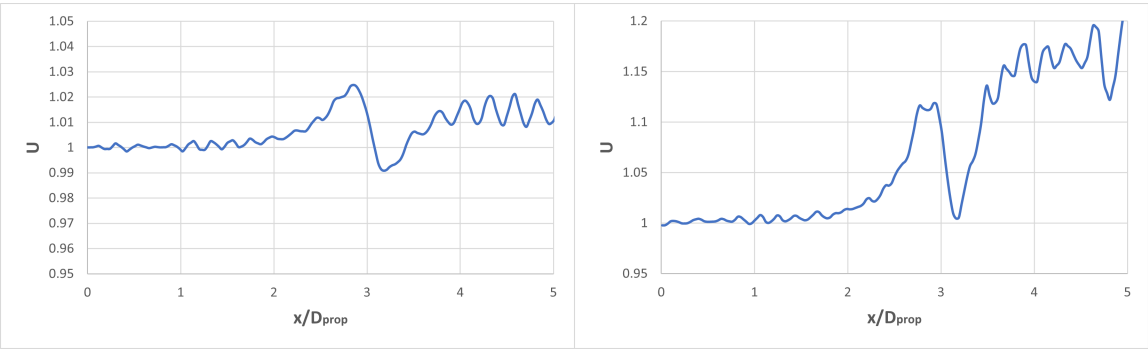

Figure 6.6: Instantaneous x-velocity jump of propeller wake centerline with J=0.6 (left) and J=0.12 (right) at about t=90

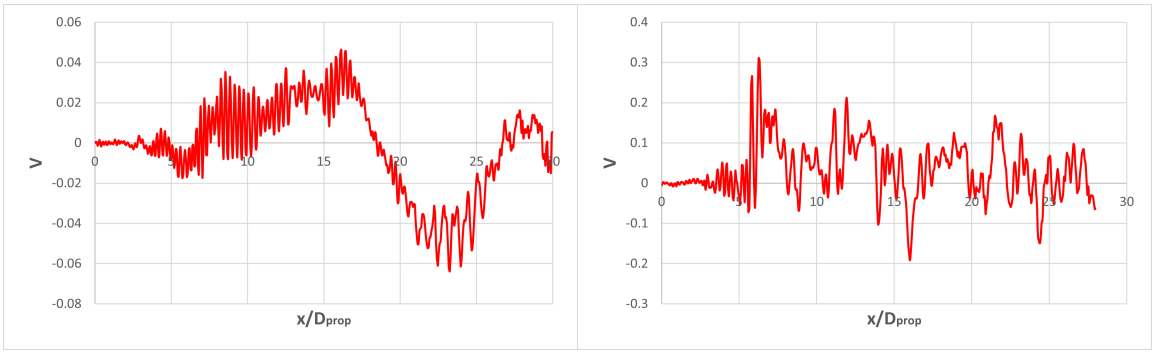

Figure 6.7: y-velocity component at propeller wake centerline with J=0.6 (left) and J=0.12 (right) at about t=90

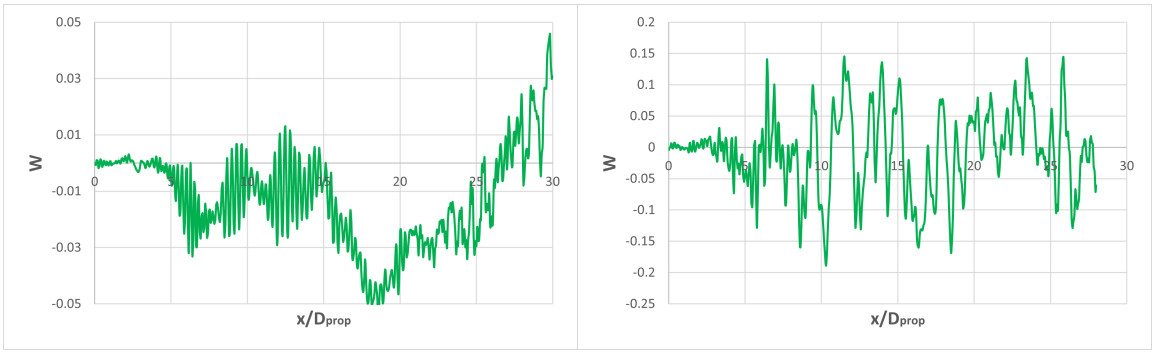

Figure 6.8: z-velocity component at propeller wake centerline with J=0.6 (left) and J=0.12 (right) at about t=90

Analogously to the instantaneous pressure, the axial velocity jump is more pronounced for J=0.12, while in both working regimes V and W are averagely near zero. This because at the centerline the influence of the blades tends to vanish.

The same variables are analysed along lines 2 and 3, defined in figures 6.3 and 6.4:

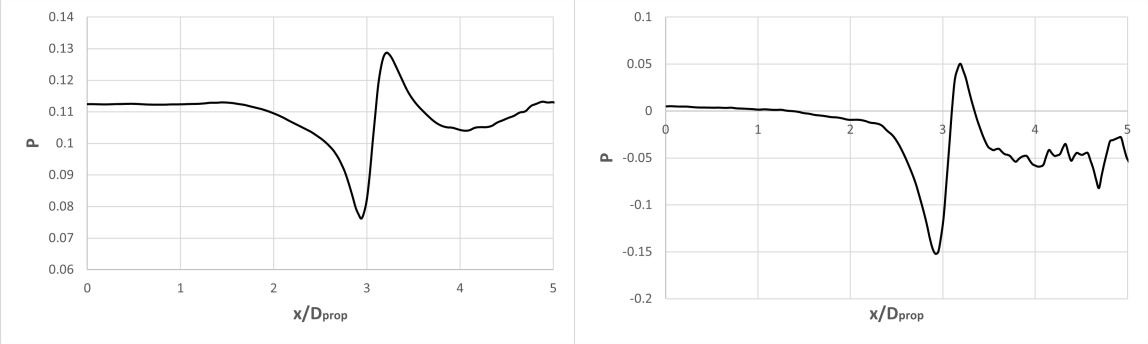

Figure 6.9: Instantaneous pressure jump along line 2 with J=0.6 (left) and J=0.12 (right) at about t=90

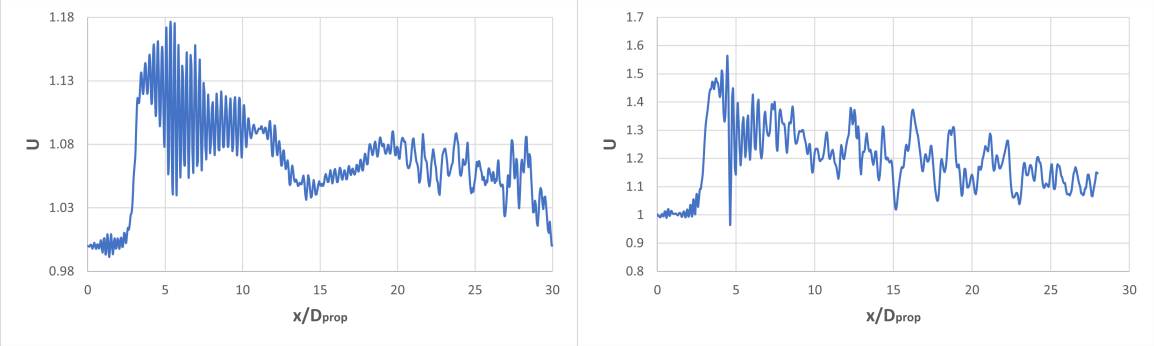

Figure 6.10: x-velocity component along line 2 with J=0.6 (left) and J=0.12 (right) at about t=90

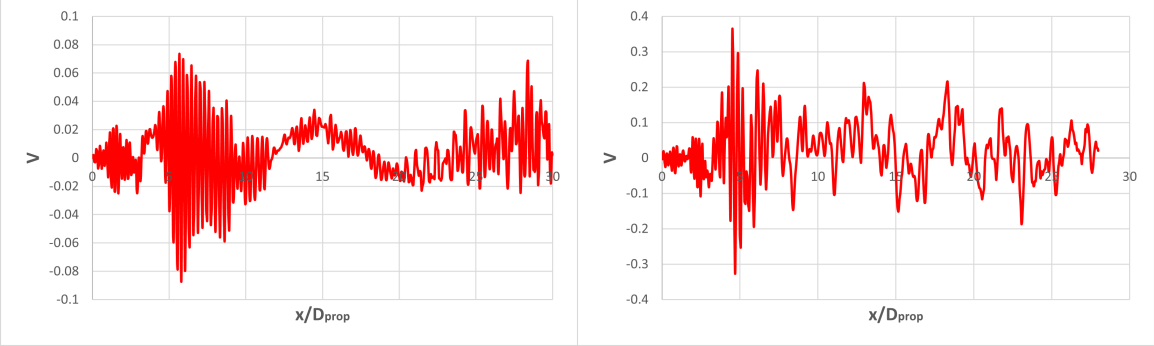

Figure 6.11: y-velocity component along line 2 with J=0.12 (left) and J=0.12 (right) at about t=90

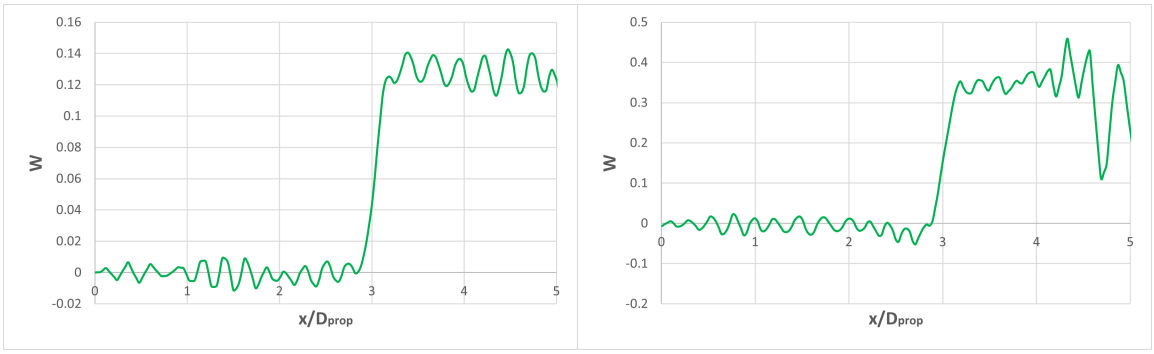

Figure 6.12: Instantaneous z-velocity jump along line 2 with J=0.6 (left) and J=0.12 (right) at about t=90

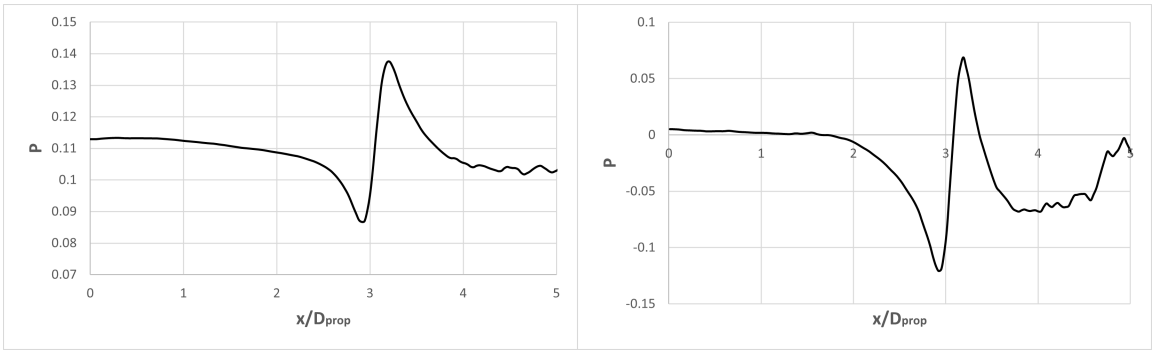

Figure 6.13: Instantaneous pressure jump along line 3 with J=0.6 (left) and J=0.12 (right) at about t=90

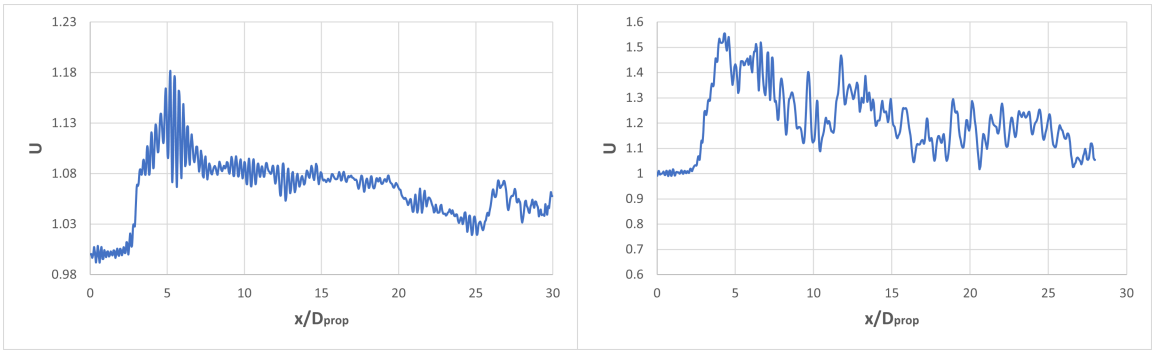

Figure 6.14: x-velocity component along line 3 with J=0.6 (left) and J=0.12 (right) at about t=90

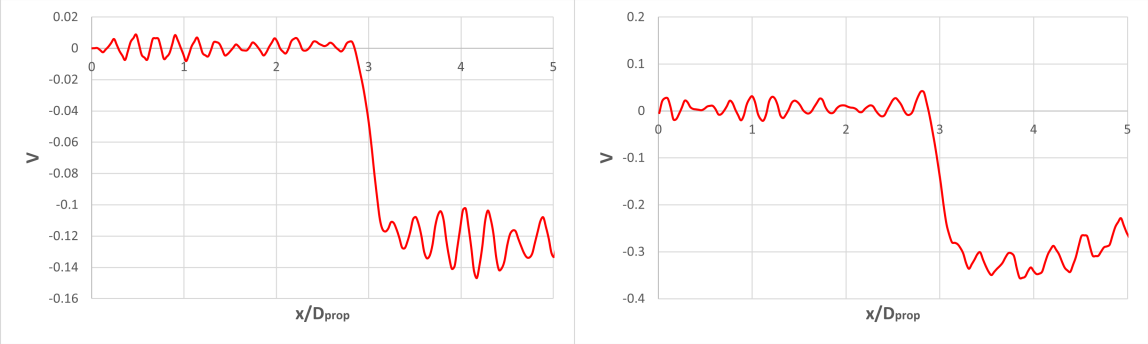

Figure 6.15: Instantaneous y-velocity jump along line 3 with J=0.6 (left) J=0.12 (right) at about t=90

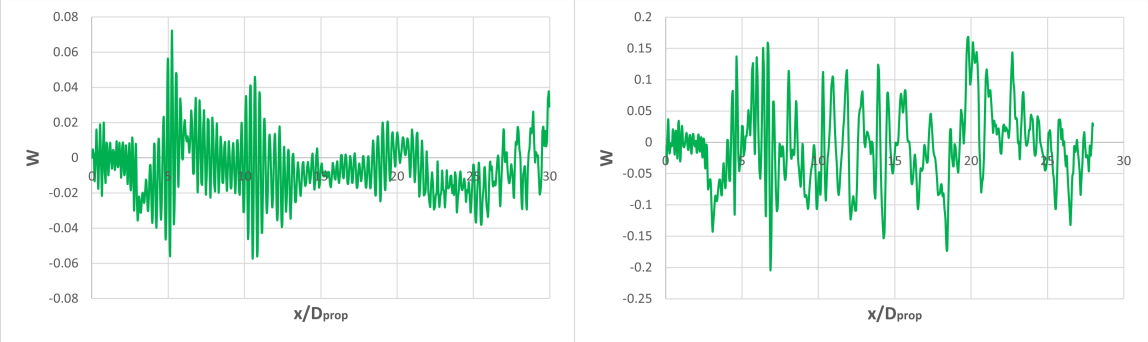

Figure 6.16: z-velocity component along line 3 with J=0.6 (left) and J=0.12 (right) at about t=90

The data collected along line 2 and line 3 confirm the considerations made for the flow variables data of line 1. A working regime characterized by J=0.12 transfers larger hydrodynamic forces to the flow. Figures 6.9 and 6.13 highlight a higher pressure jump across the propeller. Comparing left figures of 6.5, 6.9 and 6.13 (*i.e.* fixing advance ratio) it is evident that the pressure jump is higher along lines 2 and 3 with respect to the line 1 (centerline); this behaviour is caused by the presence of the blades. Moreover, as can be seen in figure 6.12, along line 2, the tangential velocity W induced by the propeller is larger for the configuration J=0.12. Similarly, along line 3, the tangential velocity V in figure 6.15 is higher for J=0.12. In particular, a negative V jump along line 2 and positive W jump along line 3 is the result of a clock-wise direction of rotation of the blades. A further confirmation of the different behaviour of the propeller is given by the trend of the axial velocity in figure 6.10 for line 2 and figure 6.14 for line 3. Furthermore, it is possible to notice (see figures 6.6, 6.7, 6.8, 6.10, 6.11, 6.12, 6.14, 6.15 and 6.16) that the oscillations in velocity components have a frequency equal to the rotational frequency of the five blades (5ω).

An interesting food for thought is provided by the analyses of eddy structures in the propeller wake, presented in the figures 6.17 and 6.18.

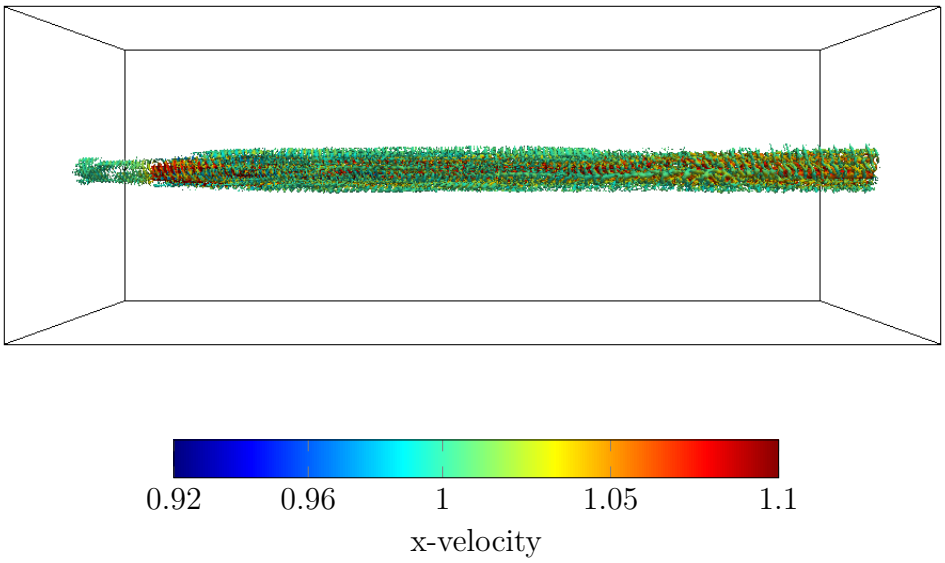

Figure 6.17: Iso-surfaces of Q-criterion=0.01, coloured with x-velocity case J=0.6

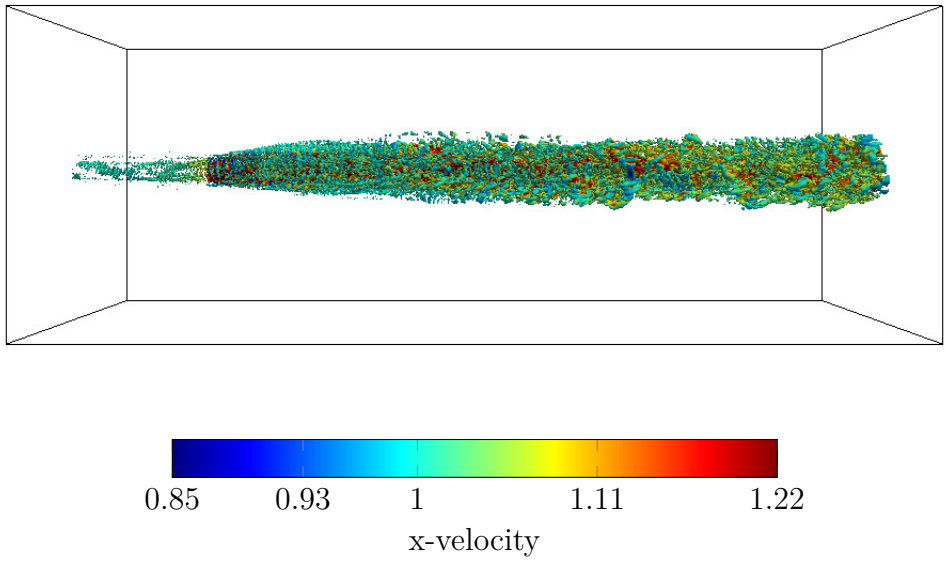

Figure 6.18: Iso-surfaces of Q-criterion=0.1, coloured with x-velocity case J=0.12

What firstly stands out is the clear presence of the blades tip vortex for the operational regime of J=0.6. Differently for J=0.12, such vortex is not detectable and breaks down in smaller turbulence structures. A better representation of blades tip vortex, for the case with J=0.6, is given in figures 6.19.

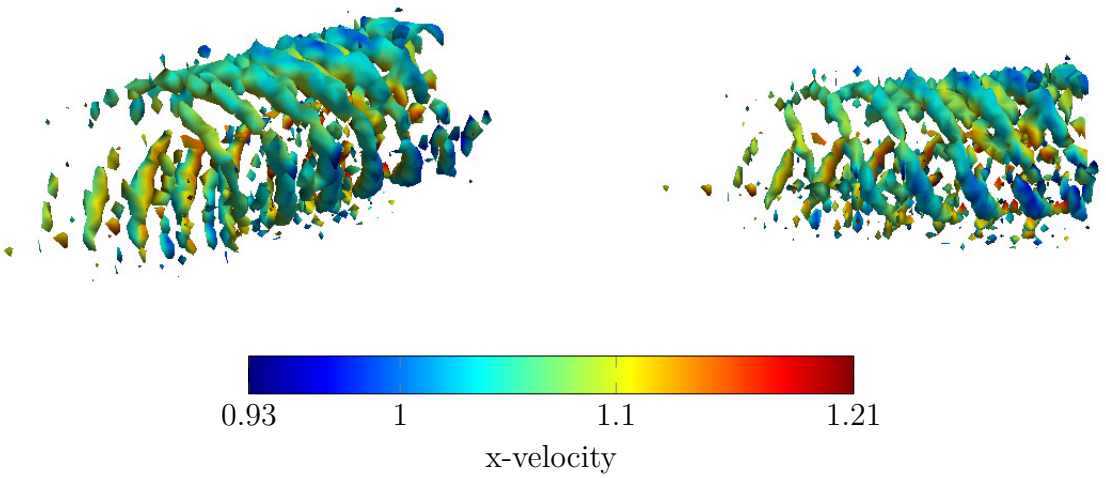

Figure 6.19: Iso-surfaces of Q-criterion=0.8 coloured with x-velocity, case J=0.6 at about t=90

In light of the previous discussions about pressure, velocity and turbulence structures of the propeller wake, it can be stated that a working regime of J=0.12 would favour the mixing and dilution process of slaked lime downstream of the propeller.

6.1.4 Single Injection

The present Section is dedicated to the analysis of data collected throughout the simulation of slaked lime discharging in the wake of a ship propeller by a single orifice. A first comparison is made considering a lime discharge with an adimensional injection velocity $u = 1$ and two different operational regimes of the propeller, characterized by two different advance ratio ($J = 0.12$ and $J = 0.6$). For the assessment of OL feasibility, it is necessary to study the evolution in space and time of the maximum values of $Ca(OH)_2$ concentration and seawater pH. After about 90 non-dimensional time units, the axial distribution of the maximum concentration and pH are presented in figures 6.20 and 6.22:

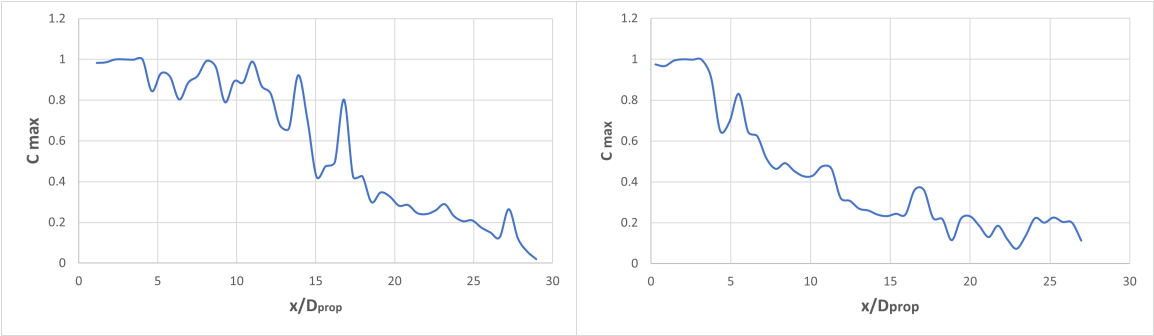

Figure 6.20: Axial distribution maximum concentration, cases J=0.6 (left) and J=0.12 (right) at about t=90

The translation in axial direction of the J=0.12 simulation data, mentioned in Section 6.1.3, is justified by the fact that in the first region of the computational domain, before the propeller location, the slaked lime variables do not have any influence, as demonstrated in the figure 6.21:

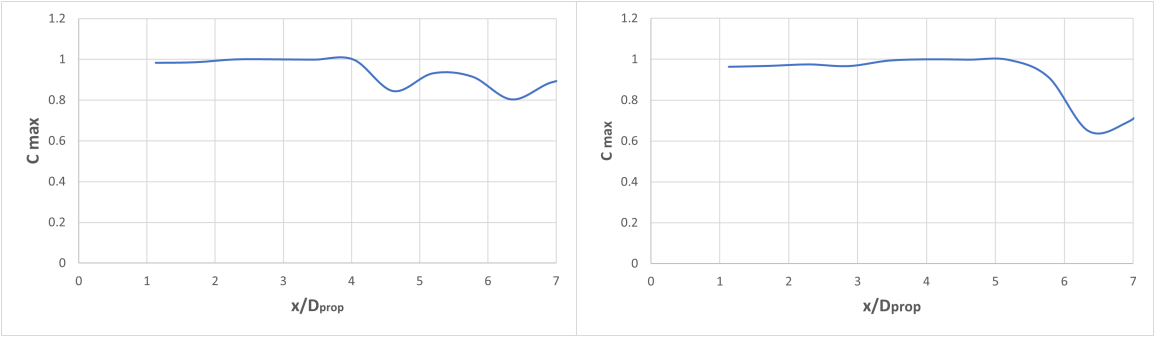

Figure 6.21: Axial distribution maximum concentration, cases J=0.6 (left) and J=0.12 (right) at about t=90, inflow region

It is clearly evident that the case with J=0.12 provides a maximum concentration profile in axial direction that is characterized by smaller values of maximum concentration with respect to the case J=0.6. This confirms the fact that the operational regime J=0.12 allows a strong mixing effect favouring the dissolution of $Ca(OH)_2$.

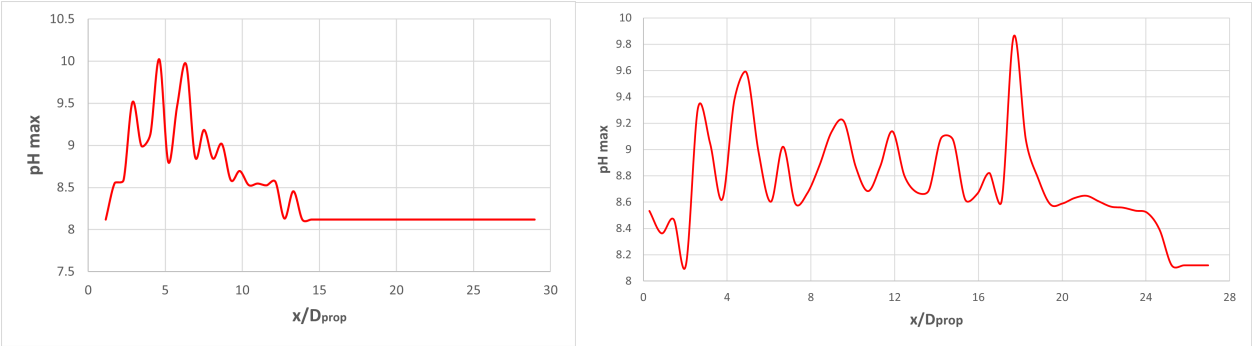

Figure 6.22: Axial distribution maximum pH, cases J=0.6 (left) and J=0.12 (right) at about t=90

Differently from the maximum concentration distribution, in both propeller configurations there is not a clear pattern of maximum seawater pH, with the presence of multiple peaks, that could affect the surrounding marine environment. A detailed discussion about time and space extension of such pH peaks is presented in the following paragraphs. The main differences of the two graphs in figure 6.22 is the more pronounced pH variation towards the outflow region for the configuration J=0.12. It is interesting to analyse the location of maximum slaked lime concentration and seawater pH. Hereafter, the following graphs represent their position in three-dimensional domain, with the addition of images of concentration and pH iso-surfaces.

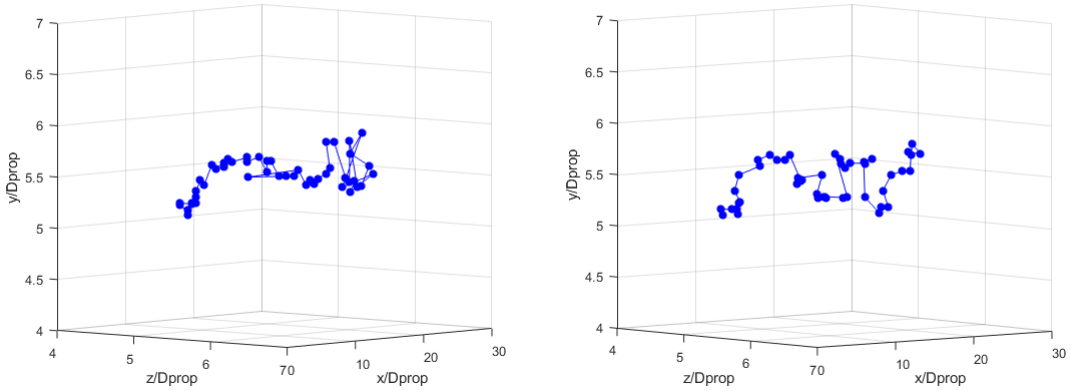

Figure 6.23: Locations of $Ca(OH)_2$ maximum concentration, cases J=0.6 (left) and J=0.12 (right) at about t=90

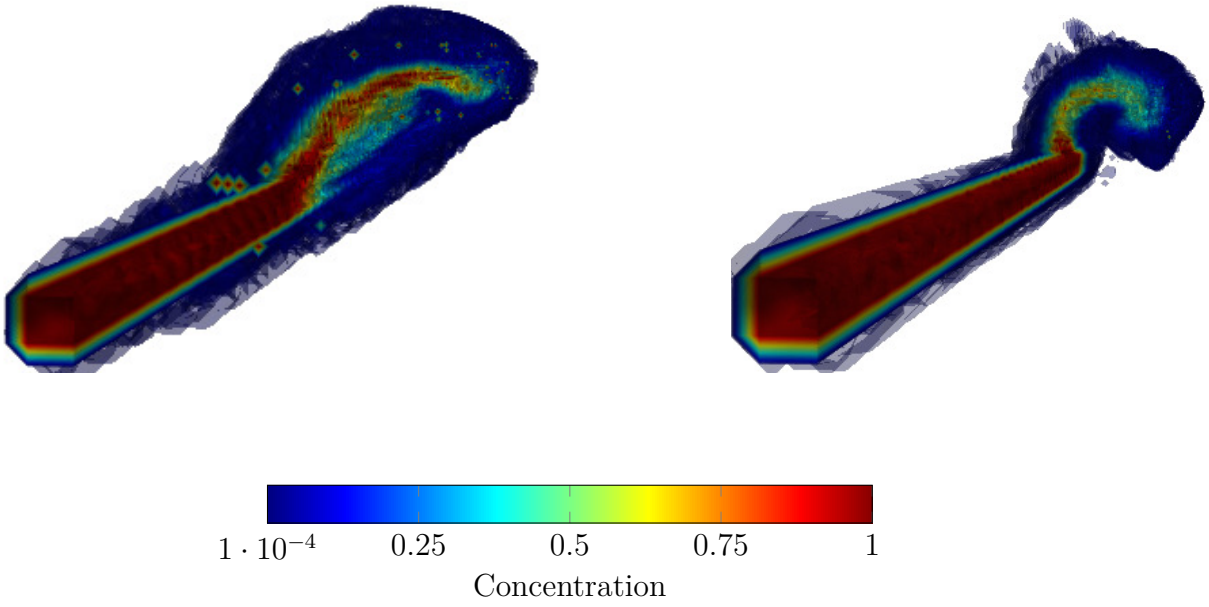

Figure 6.24: Iso-surfaces of $Ca(OH)_2$ concentration, cases J=0.6 (left) and J=0.12 (right) at about t=90

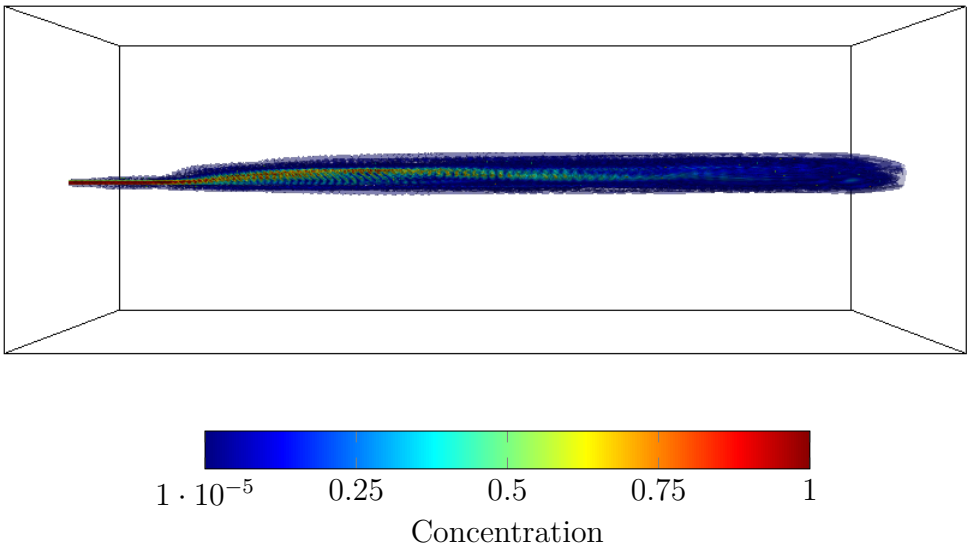

Figure 6.25: Iso-surfaces of $Ca(OH)_2$ concentration along axial direction, case J=0.6 at about t=90

From the figure 6.24 it is clear that the slaked lime concentration follows a spiral pathway, because is influenced by the propeller blades rotation. Moreover, figure 6.24 reaffirms a more prominent $Ca(OH)_2$ dissolution for the propeller with an advance ratio of J=0.12. Furthermore, it can be stated that the slaked lime does not diffuse outside the propeller wake region; this is could be due to the fact that the ship body has not been taken into account in these simulations. Figure 6.25 is proposed to highlight how slaked lime extends in axial and transversal directions.

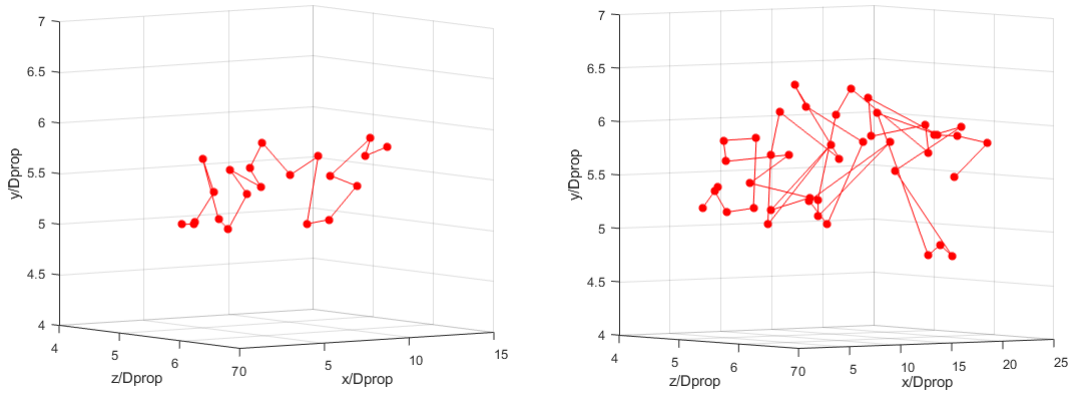

Figure 6.26: Locations of maximum pH, cases J=0.6 (left) and J=0.12 (right) at about t=90

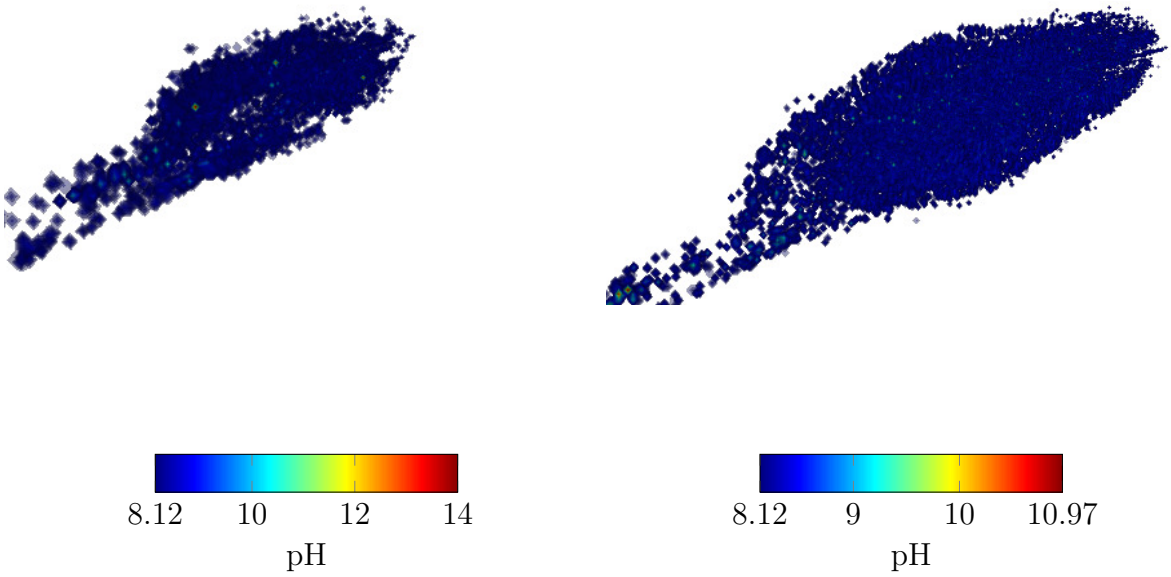

Figure 6.27: Iso-surfaces of pH, cases J=0.6 (left) and J=0.12 (right) at about t=90

The seawater pH has not a clear spiral pattern, with the presence of maximum peaks scattered in the surrounding region of the propeller. Furthermore, from figures 6.26 and 6.27 it can be highlighted the larger ability of the propeller with J=0.12 of diffusing the substance. Similar considerations can be made analysing concentration and pH profiles along y-direction:

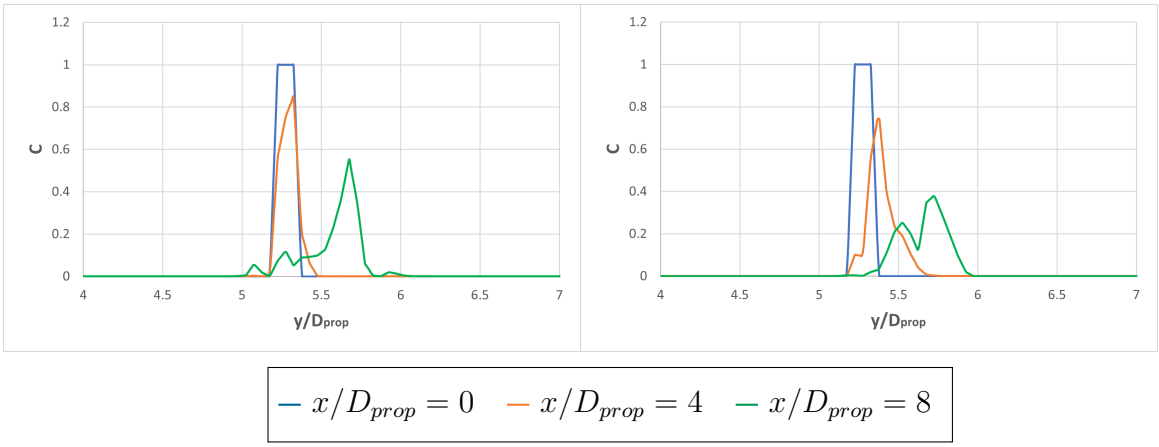

Figure 6.28: $Ca(OH)_2$ concentration profile along y-direction, cases J=0.6 (left) and J=0.12 (right) at about t=90

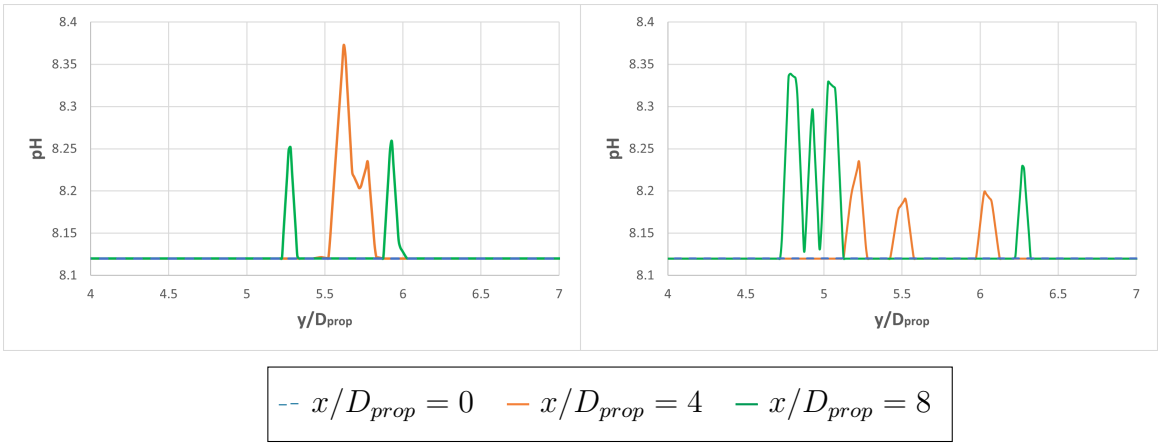

Figure 6.29: pH profile along y-direction, cases J=0.6 (left) and J=0.12 (right) at about t=90

The axial advance of the slaked lime causes the peak of the maximum concentration value to move along y-direction and decrease in value, with its diffusion into the surrounding region (see figure 6.28). On the contrary, especially for the case J=0.12, the pH profile presents scattered peak points, in restricted areas along y-direction (see figure 6.29). As regards those pH peaks it is important to study their persistence over time. Therefore, in figures 6.30, 6.31 it is presented the time history of the pH maximum value in two locations along the axial direction, for both the propeller operational regimes taken into account in this work. The two locations considered are about one non-dimensional diameter before ($x/D_{prop} \approx 2$) and two non-dimensional diameters after ($x/D_{prop} \approx 5$) the propeller longitudinal position. Together with the instantaneous values of maximum pH (red line), two different types of mean values are reported:

- Time filtered pH (green line): it is the application of a time filter on instantaneous values of maximum pH. At a given time instant, the mean value is computed considering only the previous 1000 time steps;
- Mean pH (black dashed line): it corresponds to the computation of the mean value of maximum pH, starting from the time instant of 30 non-dimensional time units until 90 non-dimensional time units.

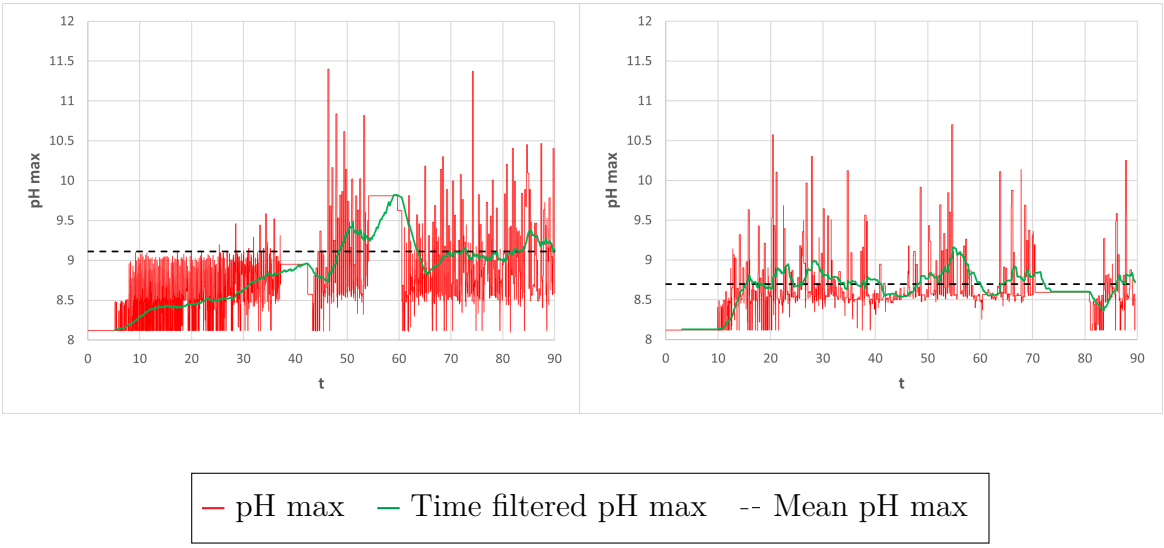

Figure 6.30: Time history of pH max before propeller axial position, cases J=0.6 (left) and J=0.12 (right)

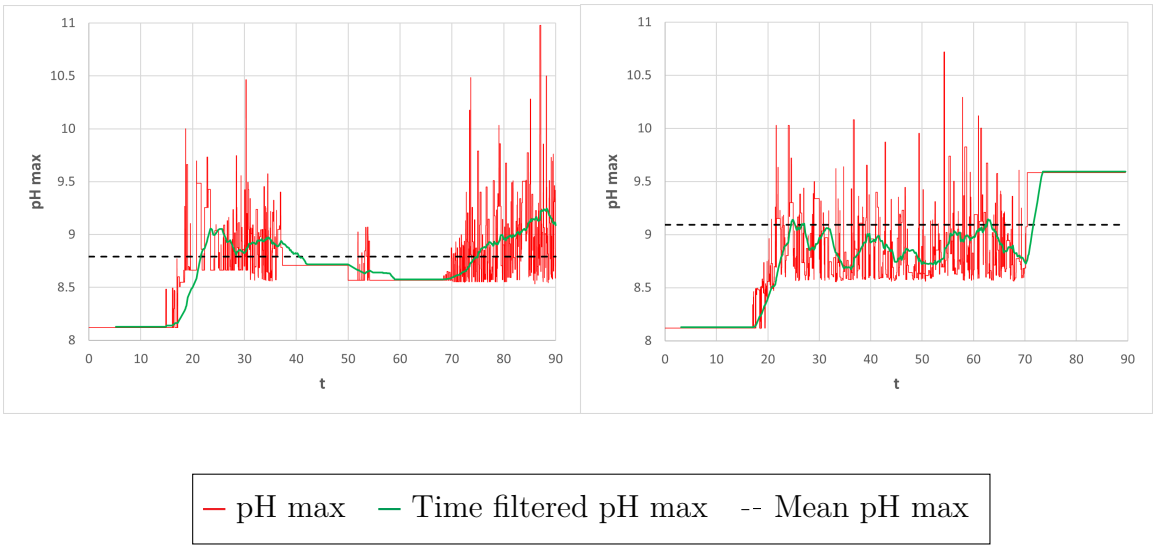

Figure 6.31: Time history of pH max after propeller axial position, cases J=0.6 (left) and J=0.12 (right)

Observing figures 6.30 and 6.31, it can be noticed that in both locations before and after the propeller the peaks of maximum pH have a small time duration, preventing the risks for the surrounding marine animal and vegetal species life. However, it would be useful for a future development to analyse if those peaks derive from the pH model adopted or an instability of the LES solver. Following a first analysis on the pH model functioning, described in details in Section 3.1.3, it turned out that those pH peaks derive from a significant sensibility of the model on the value of the dilution factor $D(t)$ (*i.e.* the dissolution of the non-reactive substance). In particular, fixing the value of pH increment due to addition of alkalinity ($\Delta pH(t)$), the final value of pH ($pH(t)$) greatly increases (or decreases) even with a small variation in the dilution factor. On the other hand, the constant intervals of maximum pH in figures 6.30 and 6.31 occur when the dilution factor remains constant and with values near to 1. In this case a pH variation due to addition of $Ca(OH)_2$ has a secondary effect on the final value of pH. In figure 6.32 it is presented the behaviour of the pH model, previously described.

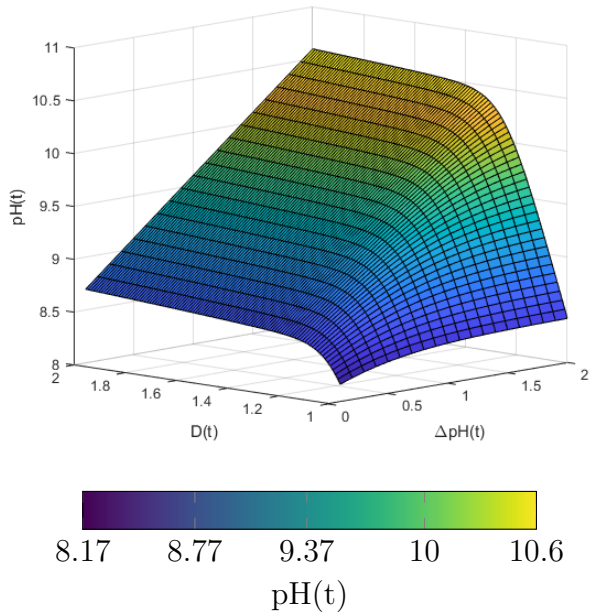

Figure 6.32: Analysis of pH model

The mean value of the maximum seawater pH tends to increase after the propeller for the case J=0.12, while for the case J=0.6 it tends to decrease. Indeed, for the case J=0.6 before the propeller we have a mean value of maximum pH equal to 9.11, while for the case J=0.12 it is equal to 8.70. On the contrary, for case J=0.6 after the propeller the mean value is equal to 8.79, while for J=0.12 it is equal to 9.09. This counter-trend behaviour could be caused by the position considered for the ensemble average: it is evident from the right figures in 6.20 and 6.22 that around two non-dimensional diameters after the propeller there is a peak in maximum concentration and pH. Having considered this axial position, the mean value of maximum pH is larger than its corresponding value before the propeller and the one in the same location but with different propeller configuration.

For the single injection configuration a further comparison is presented in the following paragraphs. Henceforth, only one operational regime of the propeller is used (J=0.6), nevertheless two different configurations are obtained by using two different mass flow rates. Being the mass flow defined as $\dot{m} = \rho A u$, considering a constant dimension of the orifice and a constant density, the different mass flow rates result in different injection velocities:

- $\dot{m} = 7,800\ kg/s$ with $u = 1$;
- $\dot{m} = 100\ kg/s$ with $u = 0.0128$.

The first mass flow rate is the result of considering a SL discharge velocity equal to the ship velocity, while the second value is taken from Caserini et al. [2021], where it was suggested as

the mass flow rate to be used for $Ca(OH)_2$ discharge in ocean. This mass flow guarantees a slaked lime discharge of 1 $Gt\ yr^{-1}$, which is the goal already presented in Chapter 2.

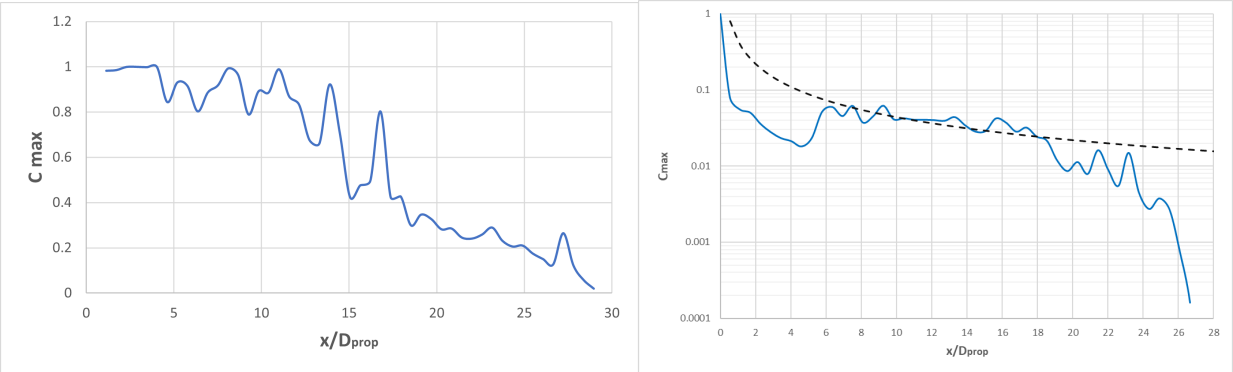

Figure 6.33: Axial distribution of maximum concentration, $u = 1$ (left) and $u = 0.0128$ (right) at about t=90; dashed line (right) is the jet model prevision (Kundu et al. [2011])

The first thing to notice is that with $u = 0.0128$ the reaction kinematics of slaked lime is much faster than its advancement velocity, for this reason in right plot of figure 6.33 a logarithmic axis for concentration has been adopted. This causes an immediate drop in concentration after the injection point, causing much smaller values of maximum concentration, than the case with injection velocity of $u = 1$, all along the axial length of domain. On the other hand, with an injection of $u = 1$ the calcium hydroxide dissolution starts to be noticeable once it passed through the propeller blades. The second important result is the evidence of the reaction contribution. With respect to the jet model of a non-reactive substance, the drop in concentration begins earlier and, globally, the values of concentration are much smaller. It is important to underline that those plots refer to the maximum concentration, while the jet model refers to a generic instantaneous value along the axial direction.

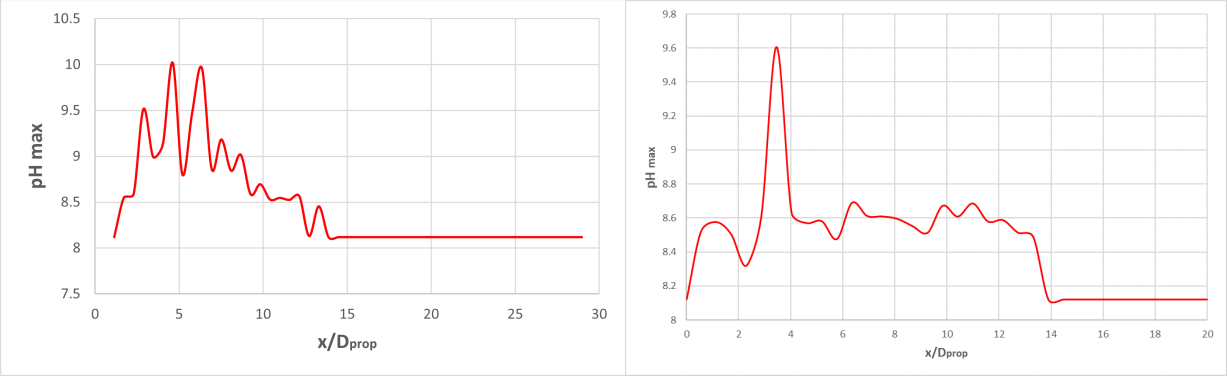

Figure 6.34: Axial distribution of maximum pH, $u = 1$ (left) and $u = 0.0128$ (right) at about t=90

From figure 6.34 it can be noted that the effect on pH of $Ca(OH)_2$ reaction is limited to the first half of the computational domain, with greater values reached by the configuration with bigger mass flow rate. From a certain longitudinal point (around 14 or 15 adimensional units) the pH values stay at the undisturbed value. The peaks of those graphs are really restricted to isolated points as can be observed in the figure 6.35.

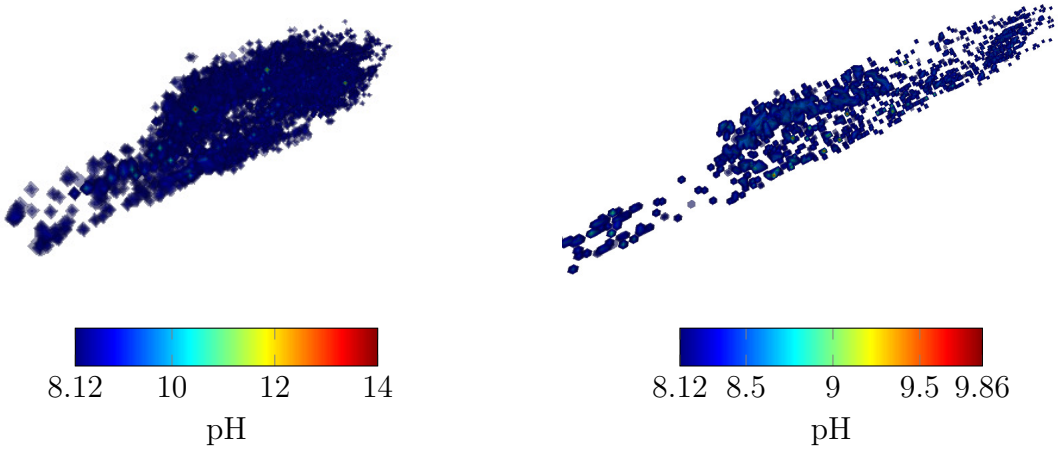

Figure 6.35: Iso-surfaces of pH, $u = 1$ (left) and $u = 0.0128$ (right) at about t=90

In figure 6.35 it is evident how the higher mass flow rate (left figure) generates a more extended region of increased alkalinity. Confirmation of this behaviour is given by the distribution of pH values, along y-direction, in different axial locations (figure 6.36).

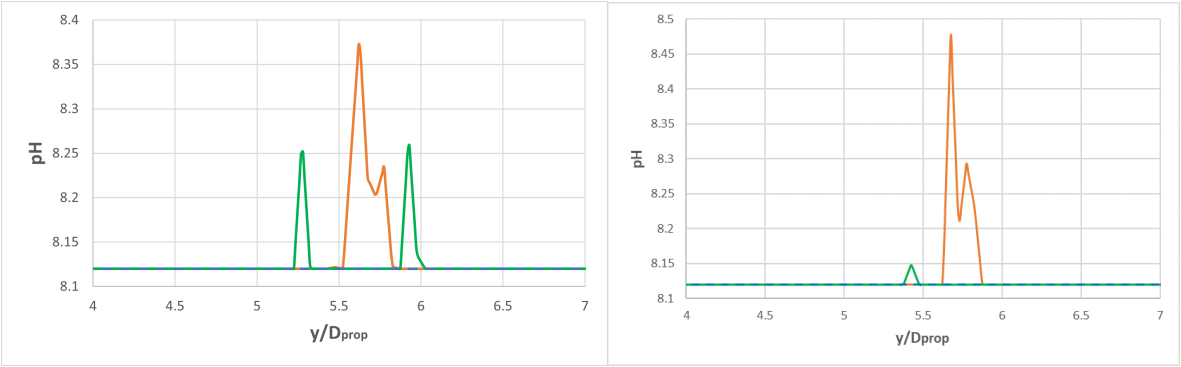

Figure 6.36: pH profile along y-direction, $u = 1$ (left) and $u = 0.0128$ (right) at about t=90

Despite the higher peak of pH at $x/D_{prop} = 4$ with $u = 0.0128$, with the injection of $u = 1$ the SL reaction effects on pH is still present at $x/D_{prop} = 8$: here the values of pH are higher and distributed on a larger portion of the y-direction.

Together with the spatial distribution, it is of considerable importance the analysis of time history, both for pH and concentration. The ensemble averages have been made in the same way as in the previous comparison between the two propeller configurations, so the two longitudinal positions and the time considered are unchanged.

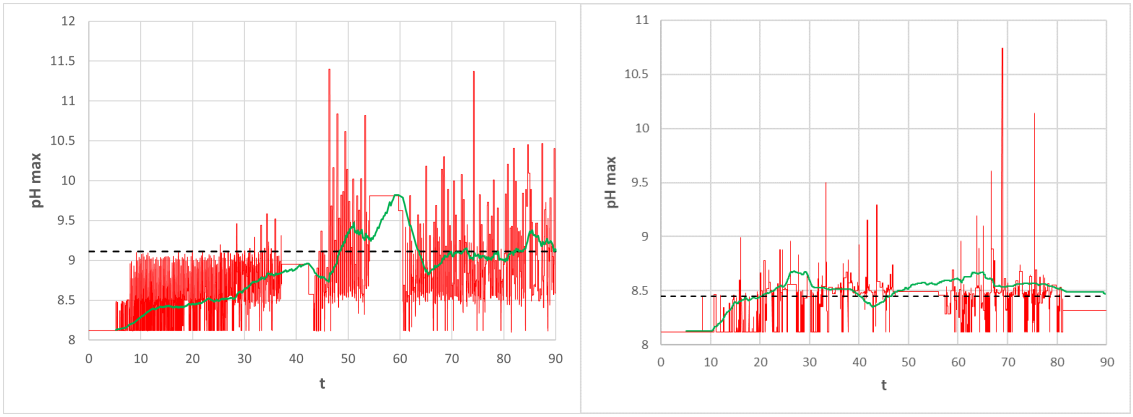

Figure 6.37: Time history of pH max before propeller axial position, $u = 1$ (left) and $u = 0.0128$ (right)

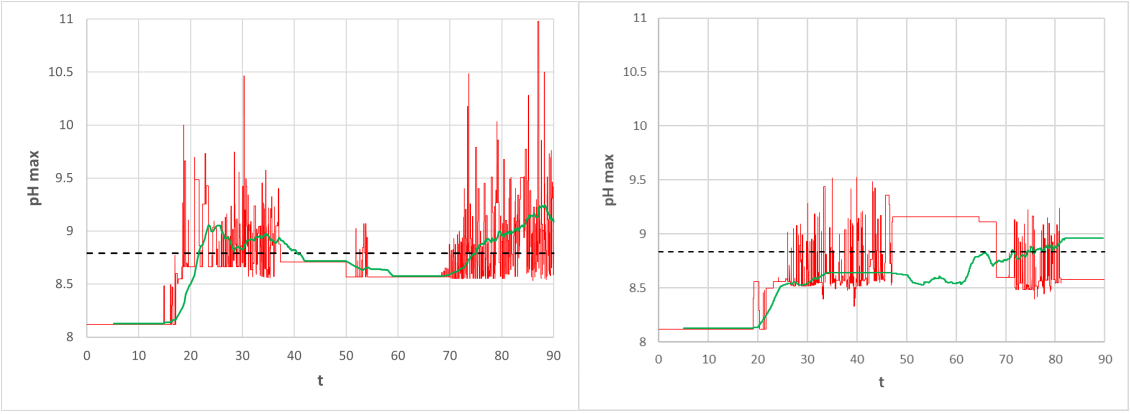

Figure 6.38: Time history of pH max after propeller axial position, $u = 1$ (left) and $u = 0.0128$ (right)

The ensemble average values of maximum pH are summarised in table 6.3.

	$u = 1$	$u = 0.0128$
$x/D_{prop} \sim 2$	9.11	8.45
$x/D_{prop} \sim 5$	8.79	8.84

Table 6.3: Values of the maximum pH ensemble averages

Comparing the results at the same axial position, it is evident that a higher mean of maximum pH is obtained when injecting slaked lime with a higher velocity ($u = 1$). On the other hand, comparing the mean values with the same configuration but on different longitudinal position there is not a univocal behaviour. In the case with $u = 1$, after the propeller the pH mean is lower than before it; on the other hand, in the case with $u = 0.0128$ the opposite is true.

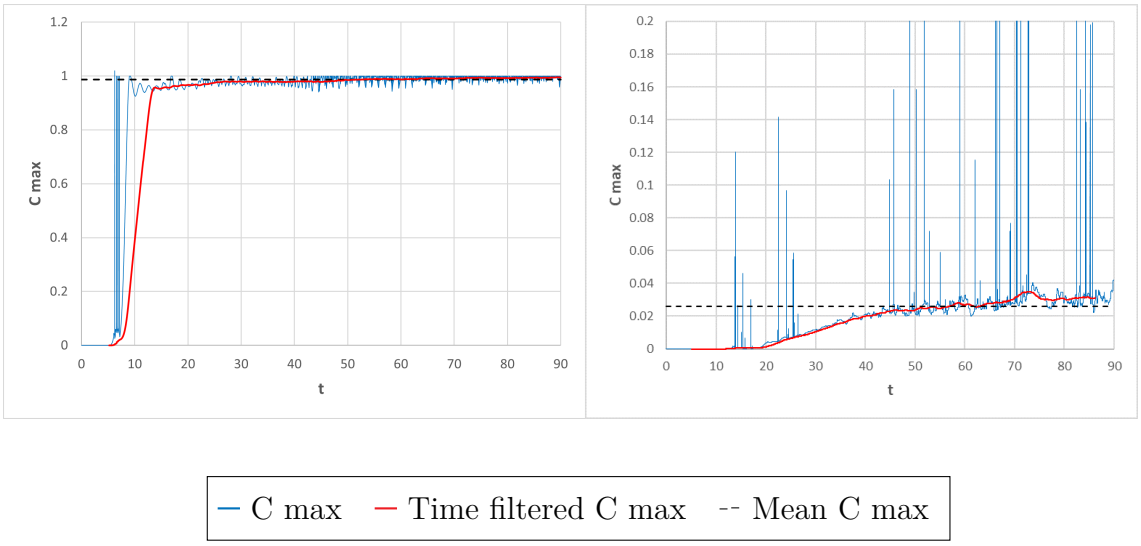

Figure 6.39: Time history of max concentration before propeller axial position, $u = 1$ (left) and $u = 0.0128$ (right)

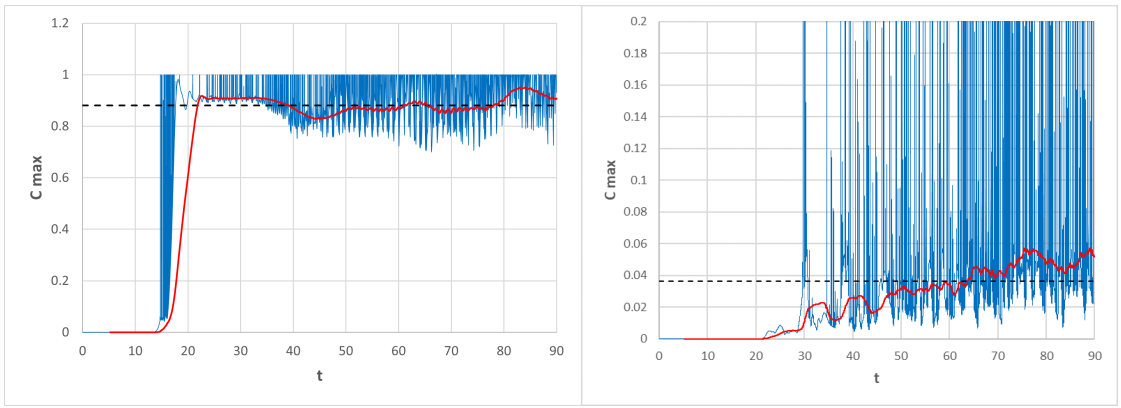

Figure 6.40: Time history of max concentration after propeller axial position, $u = 1$ (left) and $u = 0.0128$ (right)

The ensemble average values of maximum concentration are summarised in table 6.4.

	$u = 1$	$u = 0.0128$
$x/D_{prop} \sim 2$	0.9870	0.0259
$x/D_{prop} \sim 5$	0.8809	0.0364

Table 6.4: Values of the maximum concentration ensemble averages

In this case the behaviour of the maximum concentration is quite predictable: the mean values at same position are higher for $u = 1$ and lower for $u = 0.0128$; the same happens comparing the locations before and after the propeller, with higher mean values before it. Analysing the peak values of concentration, mainly present in right plots of figures 6.39 and 6.40, the explanation given is different by the one for pH peaks. Among the three terms composing the equation of concentration dynamics (3.13), the diffusive term is much smaller than the others, the source term, representing the reaction, can assume only negative values. Therefore, it is most likely that the concentration peaks are given by instability of the convective term.

6.1.5 Double Injection

The present Section has the same purpose as the previous one, now considering a double injection (from two orifices) of slaked lime. In order to maintain the same mass flow rate of 100 kg/s, each orifice has half of the total mass flow rate, so in the simulation the velocity used is $u = 0.0064$ for each point of injection. The other simulation used for comparison still has an injection velocity of $u = 1$.

As stated before, in Section 6.1.4, the assessment of OL feasibility goes through the study of space and time evolution of the maximum values of $Ca(OH)_2$ concentration and seawater pH. After the same amount of 90 non-dimensional time units, the axial distribution of maximum concentration is shown in figure 6.41. In the left figure the theoretical prevision of concentration longitudinal trend has been added, according to the jet model proposed by Kundu et al. [2011]. Only the data from this simulation can be compared to the theoretical model because they share the same mass flow condition, even if that model do not consider the reaction with seawater. It is evident that considering the reaction of slaked lime in the simulation contributes to obtain lower values of concentration.

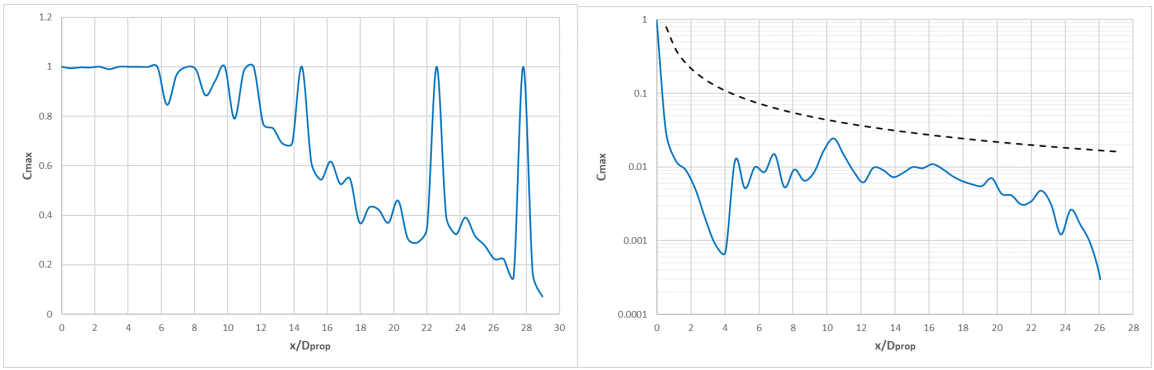

Figure 6.41: Axial distribution of maximum concentration, $u = 1$ (left) and $u = 0.0064$ (right) at about t=90; dashed line (left) is the jet model prevision

In the right figure of 6.41, it is clearly evident that the simulation concentration values are constantly lower than the ones from jet model, caused by the marked difference between the reaction kinematics and advancement velocity of the substance. In this graph a logarithmic y-axis has been used, for a better comprehension of the trend, as previously done in the right plot of figure 6.33. Furthermore, from the two plots ($u = 1$ and $u = 0.0064$) it is very clear how the concentration of slaked lime drops immediately when using a lower injection velocity, while in the other case the concentration remains almost constant until it reaches the propeller (located at $x = 3$ in both simulations). This behaviour is even more evident from the iso-surfaces of the concentration in the figure 6.43, where the highest levels of concentration are located in the initial region, near the inflow (left figure). Nevertheless, both plots in figure 6.41 show a decreasing trend, even if it is definitely more noticeable in the left one.

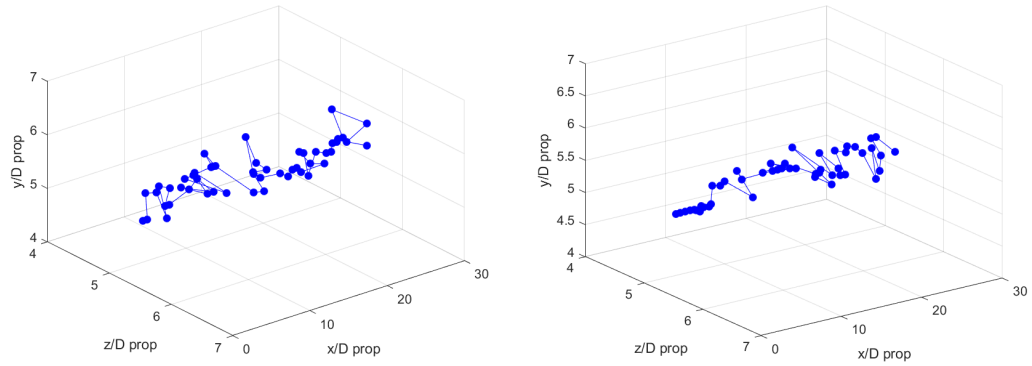

Figure 6.42: Locations of $Ca(OH)_2$ maximum concentration, $u = 1$ (left) and $u = 0.0064$ (right) at about t=90

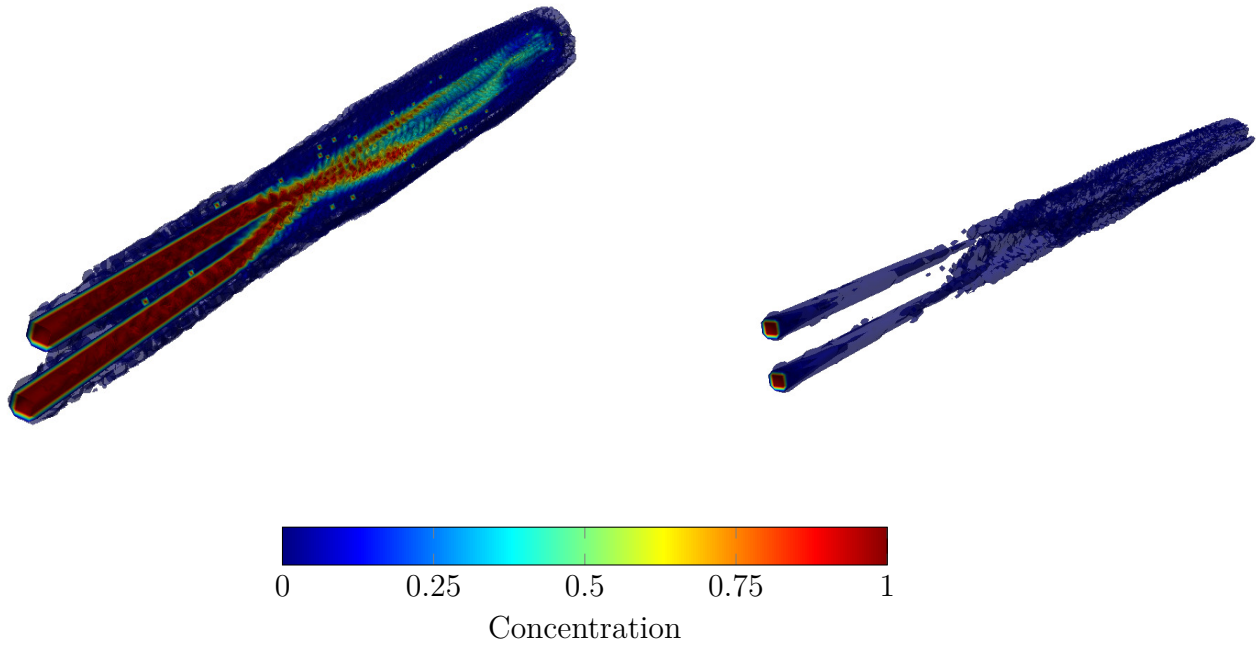

Figure 6.43: Iso-surfaces of $Ca(OH)_2$ concentration, $u = 1$ (left) and $u = 0.0064$ (right) at about t=90

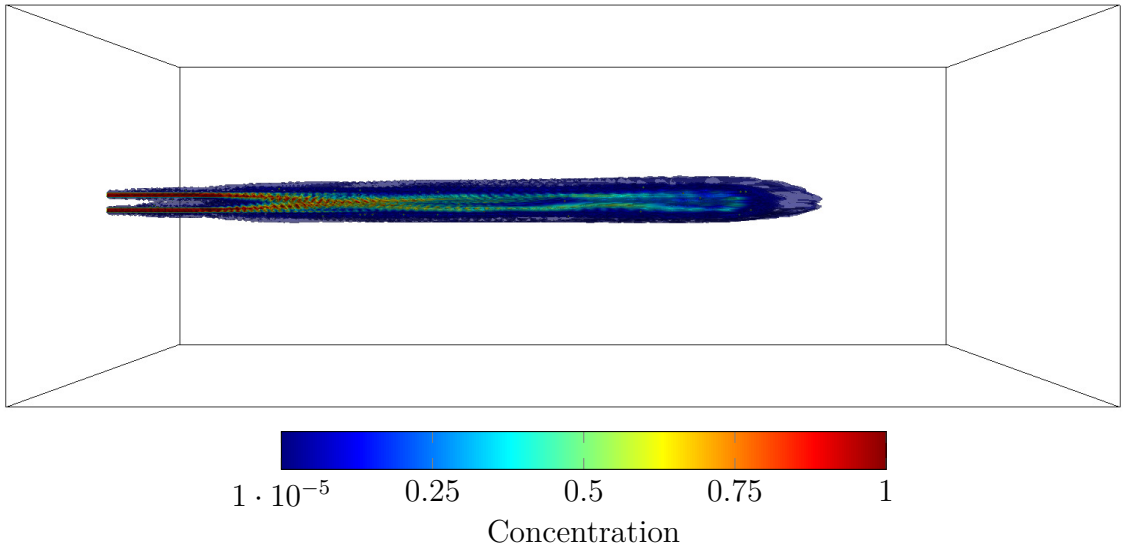

Figure 6.44: Iso-surfaces of $Ca(OH)_2$ concentration along axial direction, $u = 1$ at about t=90

The concentration decreasing tendency suggests that with $u = 0.0064$ the slaked lime

rapidly reacts with water, not having enough speed to proceed further; in the whole domain the maximum values of concentration are really smaller than the ones with an injection of $u = 1$. Because of the small values of concentration, the spiral pathway is almost lost in the case of smaller mass flow rate, but still noticeable in the other case (see figure 6.43). This spiral pathway can also be seen in figure 6.42, which is the 3D-plot of the locations of maximum concentrations along the domain. Unfortunately, a 2D representation has a big limit in showing three-dimensional patterns. As previously presented in Section 6.1.4, figure 6.44 is reported in order to show the axial and transversal propagation of $Ca(OH)_2$ concentration. Similarly to figure 6.25, the transversal extension is limited at the propeller wake region.

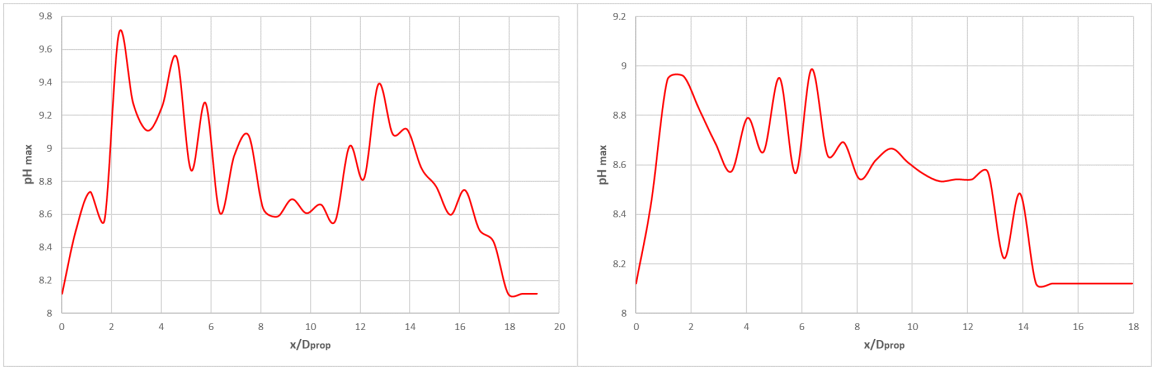

Figure 6.45: Axial distribution of maximum pH, $u = 1$ (left) and $u = 0.0064$ (right) at about t=90

Regarding the pH axial distribution, figure 6.45 shows that in both cases, despite of the wide oscillations, clearly there is a descending trend that follows a region of alkalinity growth. The main differences are firstly that the higher values of pH are reached with $u = 1$, and secondly that the region where pH starts to decrease begins earlier with $u = 0.0064$.

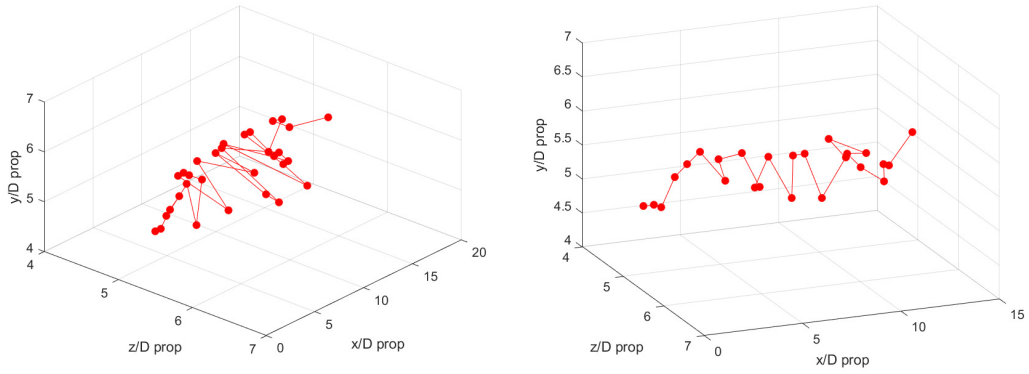

Figure 6.46: Locations of maximum pH, $u = 1$ (left) and $u = 0.0064$ (right) at about t=90

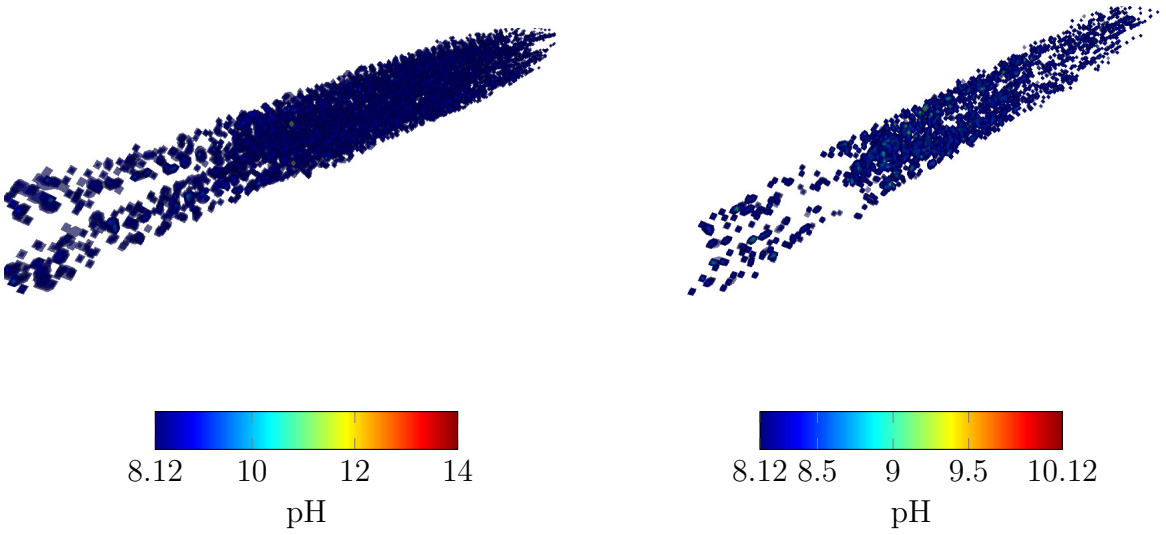

Figure 6.47: Iso-surfaces of pH, $u = 1$ (left) and $u = 0.0064$ (right) at about t=90

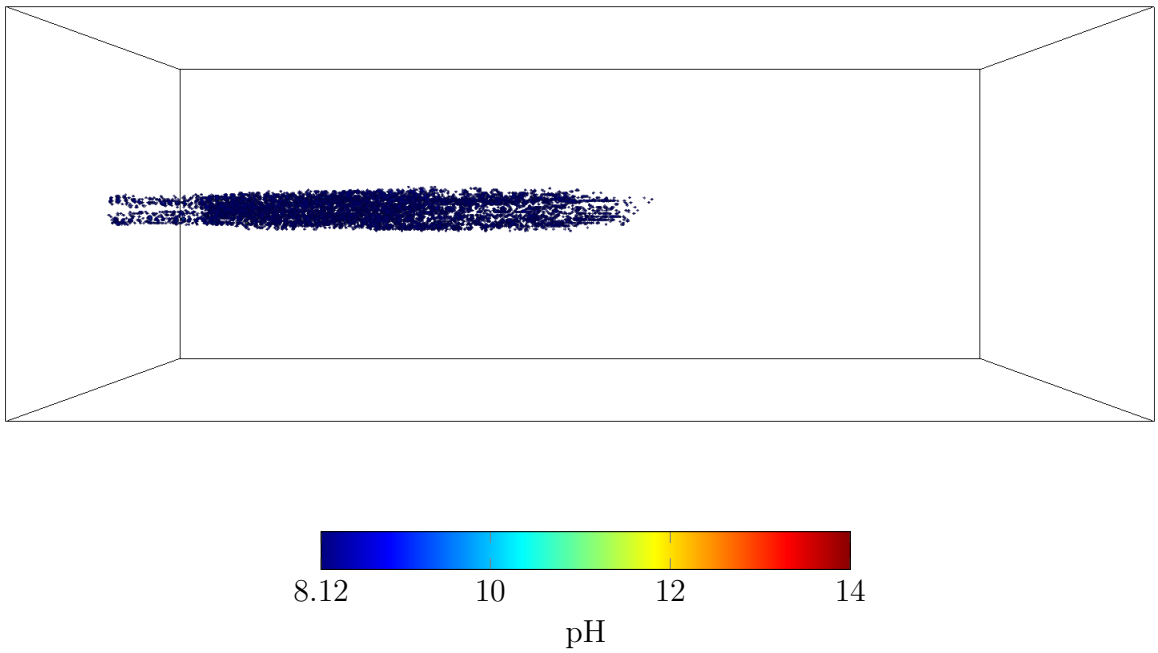

Figure 6.48: Iso-surfaces of pH, $u = 1$ (double injection) at about t=90

Differently from the concentration distribution, the pH has not a clear spiral pattern but generates a diffused region of increased pH, with the presence of disseminated peak values in the region behind the propeller. In figure 6.47, the remarkable difference between the two

configurations is how much the $Ca(OH)_2$ has affected the seawater pH: as expected, in the $u = 0.0064$ case, with lower levels of concentration beyond the propeller, also the seawater pH is nearer to the undisturbed value of 8.12.

As previously done for the single injection configurations, the y-direction distributions of pH and concentration, at different axial locations, have been studied.

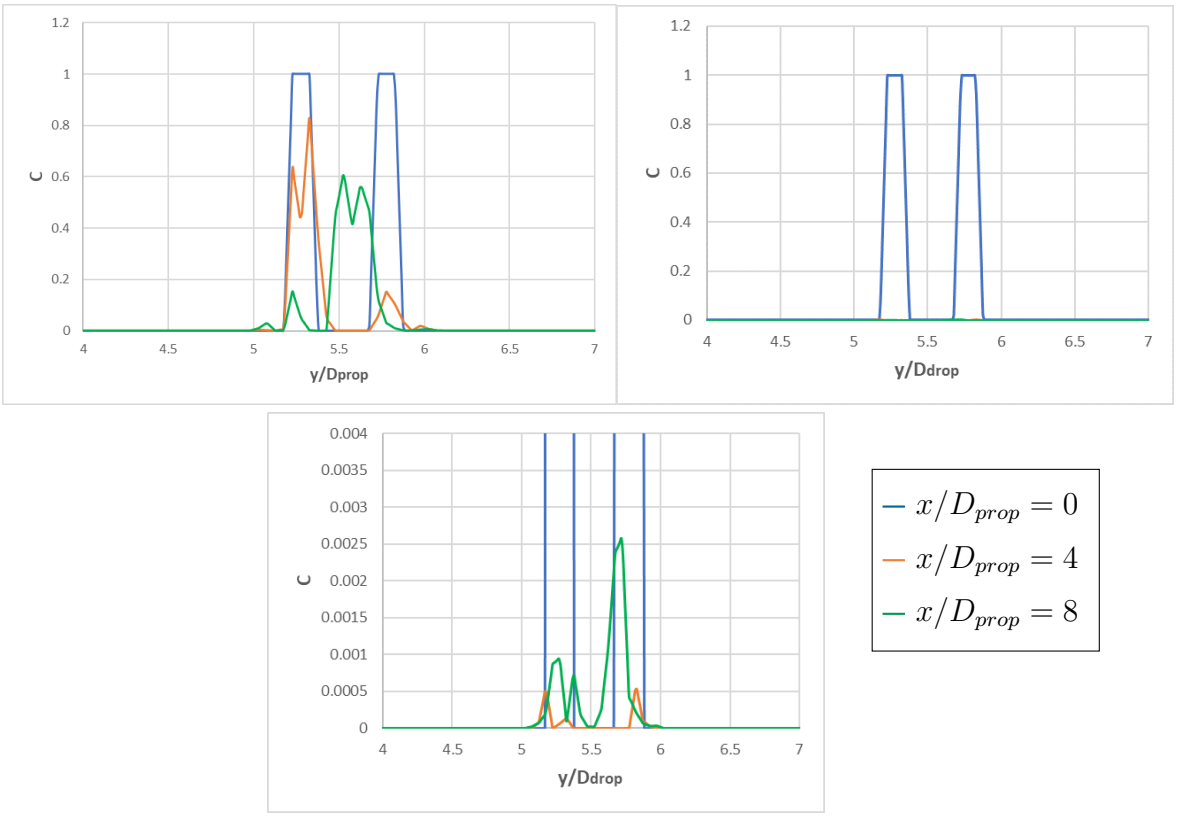

Figure 6.49: $Ca(OH)_2$ concentration profile along y-direction, cases $u = 1$ (left) and $u = 0.0064$ (right) at about t=90. The lower figure is a zoom of $u = 0.0064$ (left) to see the small changes

The important result deducible from figure 6.49 is how the two injection fluxes of concentration tend to fuse together after the propeller action ($x/D_{prop} = 8$), simultaneously the maximum value of concentration decreases.

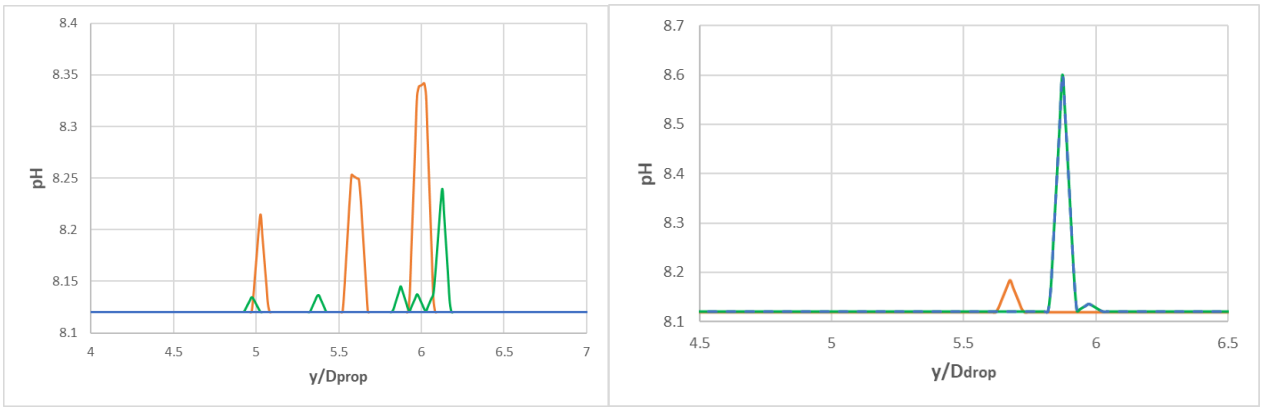

Figure 6.50: pH profile along y-direction, $u = 1$ (left) and $u = 0.0064$ (right) at about t=90

The most interesting result of pH distributions (figure 6.50) is the number of multiple pH peaks distributed on a wider portion, along y-direction, when using higher injection velocity. However, the height of a single peak is not of particular interest, for this reason it was necessary to conduct a temporal analysis. The locations where the data has been collected are respectively one diameter before the propeller and two diameters beyond it.

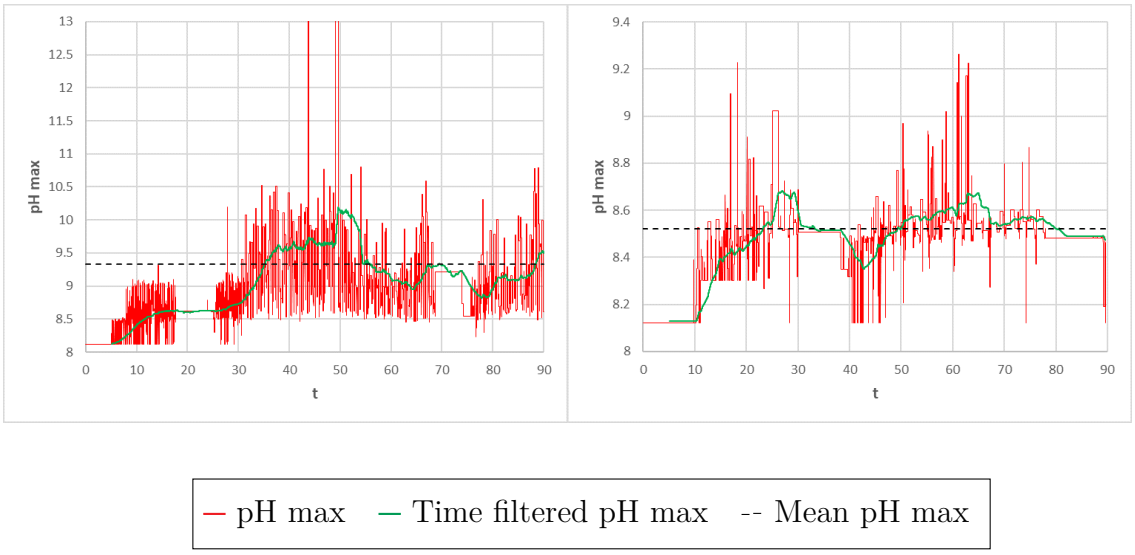

Figure 6.51: Time history of pH max before propeller axial position, $u = 1$ (left) and $u = 0.0064$ (right)

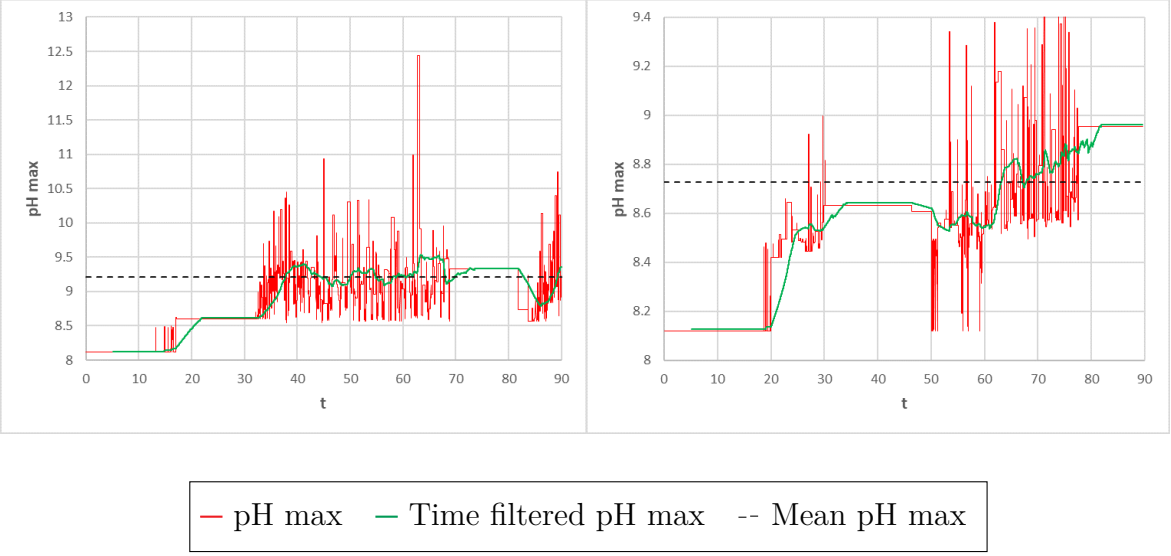

Figure 6.52: Time history of pH max after propeller axial position, $u = 1$ (left) and $u = 0.0064$ (right)

The values of ensemble average are reported in the following table:

	$u = 1$	$u = 0.0064$
$x/D_{prop} \sim 2$	9.33	8.52
$x/D_{prop} \sim 5$	8.21	8.73

Table 6.5: Values of the maximum pH ensemble averages for double injection configuration

As expected, the ensemble average of maximum pH at the same longitudinal position are higher for $u = 1$. On the other hand, the mean value after the propeller, with respect to the antecedent location, is higher with $u = 1$ but lower with $u = 0.0064$. A possible explanation of this behaviour is given in the next Section 6.1.6.

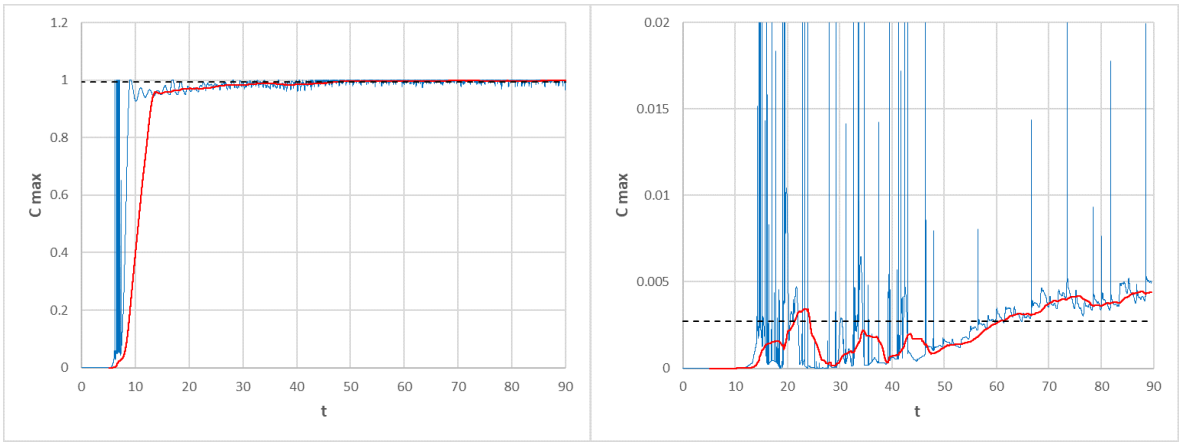

Figure 6.53: Time history of C max before propeller axial position, $u = 1$ (left) and $u = 0.0064$ (right)

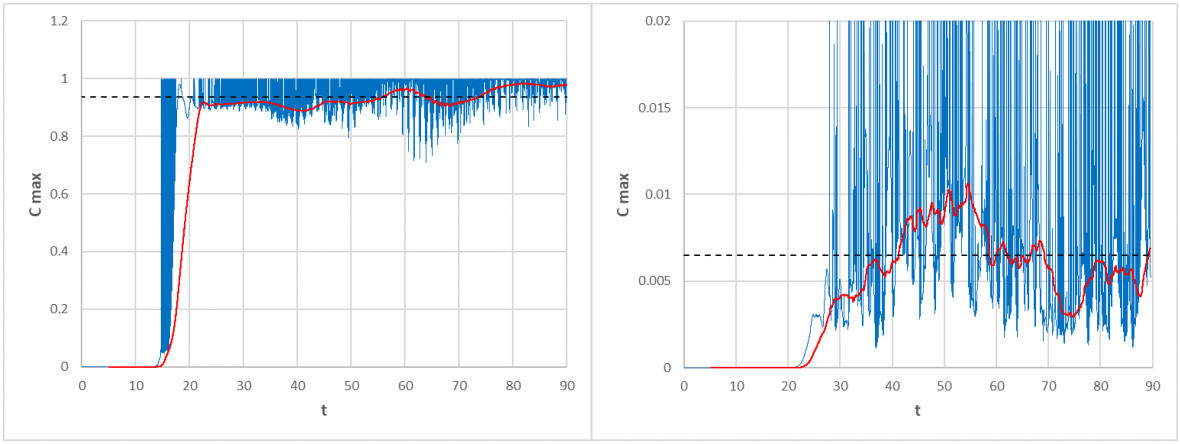

Figure 6.54: Time history of C max after propeller axial position, $u = 1$ (left) and $u = 0.0064$ (right)

The ensemble average values of maximum concentration (for double injection configurations) are summarised in table 6.6. Similar considerations to pH mean values could be made for concentration mean values.

	$u = 1$	$u = 0.0064$
$x/D_{prop} \sim 2$	0.9937	0.0027
$x/D_{prop} \sim 5$	0.9370	0.0065

Table 6.6: Values of the maximum concentration ensemble averages for double injection configuration

6.1.6 Single Injection vs. Double Injection

In this section it will be presented an overall comparison between the two configurations of single and double injection.

The first comparison presented is between the two cases with the velocity injection of $u = 1$. It is relevant to analyse the slaked lime dissolution process in function of space. In light of this, an average of concentration and seawater pH on different transverse sections has been computed, taking values on a square of $2D_{prop} \times 2D_{prop}$ along y and z-directions as shown below:

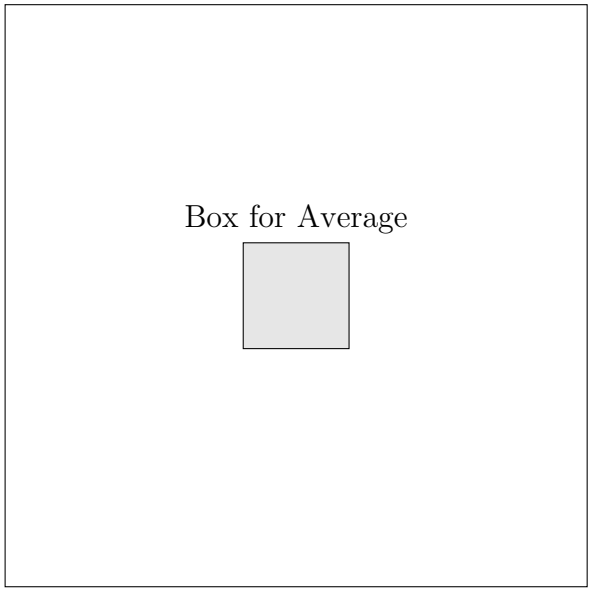

Figure 6.55: $2D_{prop} \times 2D_{prop}$ box (gray) on transverse section for average computation

The concentration and seawater pH axial distributions are shown in the following figures:

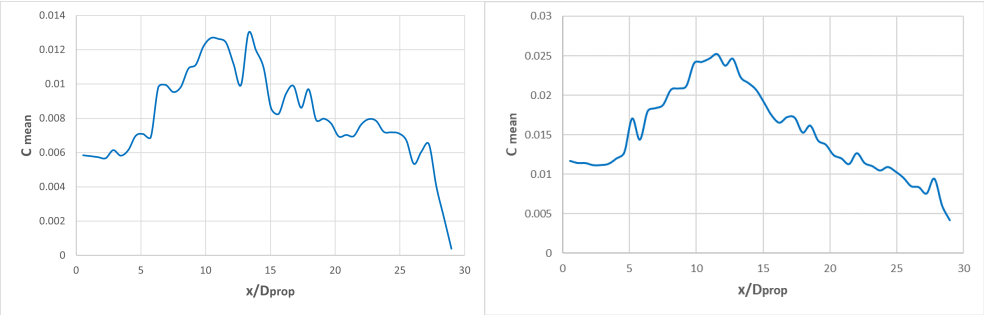

Figure 6.56: Mean concentration along x-direction, single injection (left) and double injection (right) at about t=90

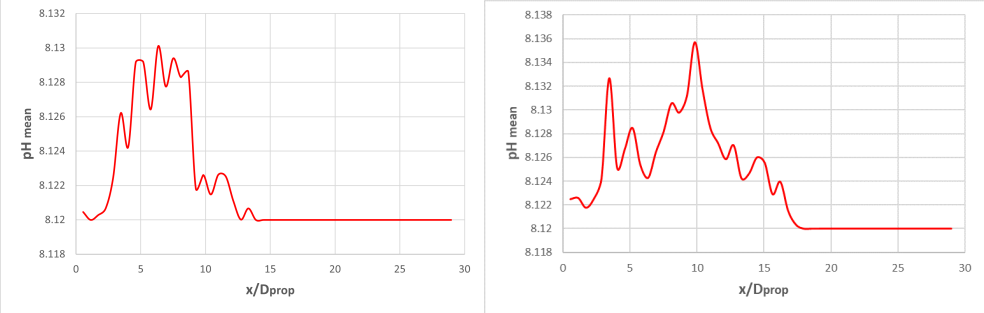

Figure 6.57: Mean pH along x-direction, single injection (left) and double injection (right) at about t=90

At equal injection velocity, the double injection allows to have an effect on further positions along x-direction, as can be seen in 6.57 by the axial extension of perturbed pH. In figure 6.56 it is clear that the concentration has the same longitudinal trend, while values reached by it are approximately double.

Hereafter are presented the figures of comparison at same mass flow rate of 100 kg/s.

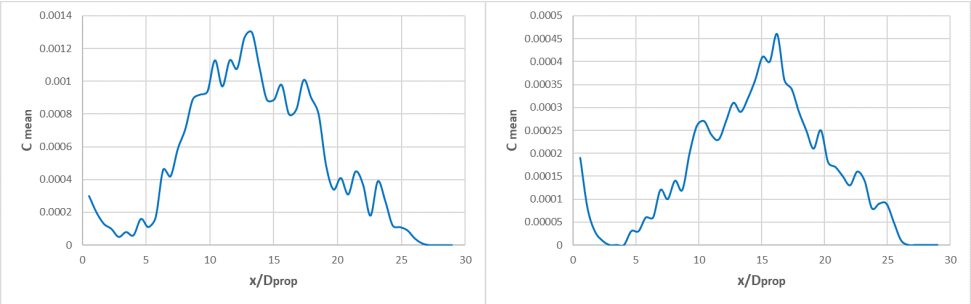

Figure 6.58: Mean concentration along x-direction, single injection (left) and double injection (right) at about t=90, mass flow rate $\dot{m} = 100\ kg/s$

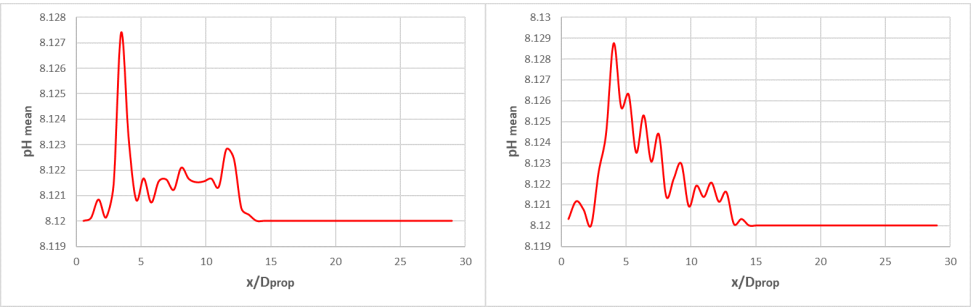

Figure 6.59: Mean pH along x-direction, single injection (left) and double injection (right) at about t=90, mass flow rate $\dot{m} = 100\ kg/s$

Differently from the previous case, now the double injection configuration does not have a farther effect on concentration and pH along the longitudinal direction. Moreover, in the double injection configuration the dissolution of slaked lime is more prominent, caused by both the larger contact surface between $Ca(OH)_2$ and water particles and the lower injection velocity. This can be explicitly seen in both figures (6.58 and 6.59), because the occurrence of the reaction favours the pH increment and the concentration reduction.

Finally, the behaviour in common among all the configurations presented, that explains what has been anticipated at the of Section 6.1.5, is the tendency of pH to quickly increase in the region right after the propeller, where concentration has a local minimum value. Therefore, the higher mixing effect of the propeller in this region enhances the dissolution of calcium hydroxide. In the subsequent area, until the middle of the domain, the concentration starts to increase. Hence, it can be deduced that, in this region, convection has a predominant effect respect to the reaction process.

6.2 Slaked lime discharge with bluff body

The previous slaked lime discharge simulations were focused on analysing the impact of the propeller in the dilution process of calcium hydroxide in seawater, with two different advance ratios. Moreover, two different layouts of discharging have been taken into account in order to have an additional parameter to refine the technique of $Ca(OH)_2$ release. Anyway, these types of simulations do not fully reflect what happens in reality. For this reason it was decided to simulate the contribution of the ship hull, with the addition of a bluff body at the inflow plane of the computational domain.

6.2.1 Problem geometry and setup

The LES simulation with the addition of the bluff body is characterized by a setup similar to the one of the previous simulations, presented in Section 6.1.1. The geometry of the computational domain is identical to the one of figure 5.3. Differently from the previous simulations, the propeller is located at 2 diameters from the inlet along the axial direction, in order to study the interaction between the wake of the hull and that of the propeller. Concerning the ship body, the hull is modelled as a bluff body positioned at the domain inlet for reducing the computational cost.

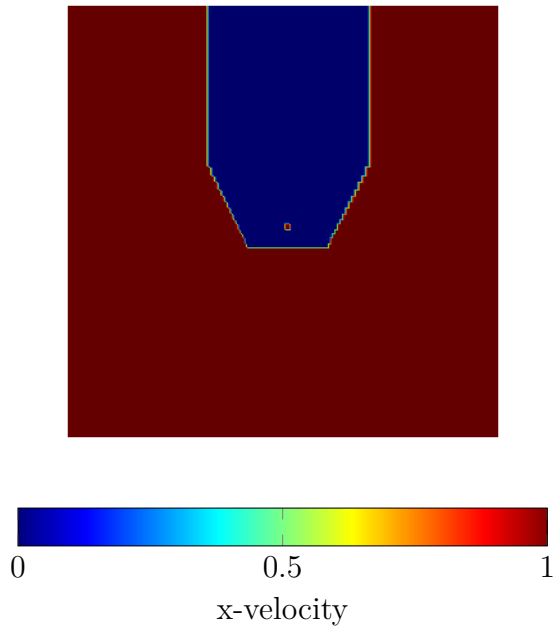

Figure 6.60: Axial velocity distribution at the inflow region

As can be seen from the figure 6.60, the bluff body, for modelling the ship hull, has a width of $4D_{prop}$ along z direction and a height of $5.5D_{prop}$, starting from the upper surface of the domain. As regards the main parameters of the simulation it is worth to notice that Reynolds number is maintained equal to the one of the previous simulations ($Re = 25,000$), while the Smagorinsky coefficient Cs has been increased to a value of $Cs = 0.04$, because the bluff body wake, simulated with $Cs = 0.02$ presented instability problem. In conclusion, the boundary and initial conditions, for pressure and velocity employed, are identical to the ones of table 6.1, except from the inlet velocity ones. Indeed, each velocity component is imposed to zero nearby the bluff body, while in the surrounding region only the axial velocity component is different from zero and has a constant value $u = 1$. Therefore, it is simulated a slaked lime discharge of about 7800 kg/s.

6.2.2 Mesh generation

Regarding the computational grid the mesh configuration adopted is analogous to the one employed in the propeller wake simulations. For details consult table 6.2. It was decided to not further refine the mesh in the region that surrounds the bluff body, because the resolution of the hull wake is beyond the scope of the present work. The aim of this thesis is a preliminary study of the mutual interference between the wake of the hull and the one of the propeller, that could influence the discharging pattern of the slaked lime and the kinematics of the reaction with seawater.

6.2.3 Results

The following Section is dedicated to the presentation of the results obtained with the addition of a bluff body and a brief comparison between them and the ones from the single injection configuration already presented in Section 6.1.4. The main focus is on the interaction between the hull and propeller wakes and their effects on the dissolution process of slaked lime. Hereafter, it is presented the wake visualisation of the modelled hull (located at the inflow):

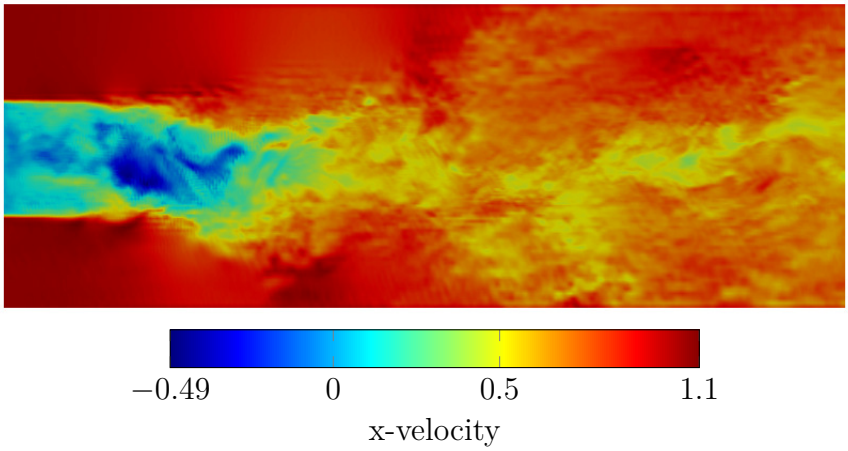

Figure 6.61: Axial velocity distribution on $x - z$ upper plane

Concerning the simulations data, the axial distribution of concentration and pH maximum values, for the single injection with only the propeller ($u = 1$) and with addition of the bluff body, are presented below:

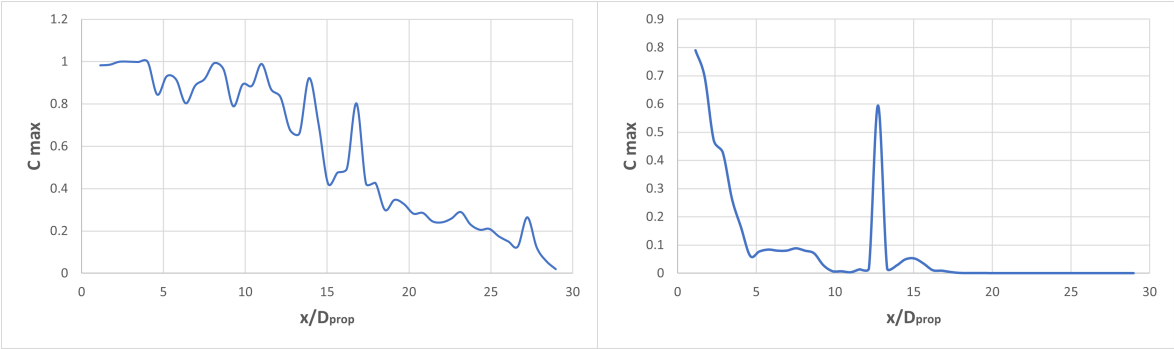

Figure 6.62: Axial profile of maximum concentration for propeller only simulation (left) and bluff body simulation (right) at about t=90

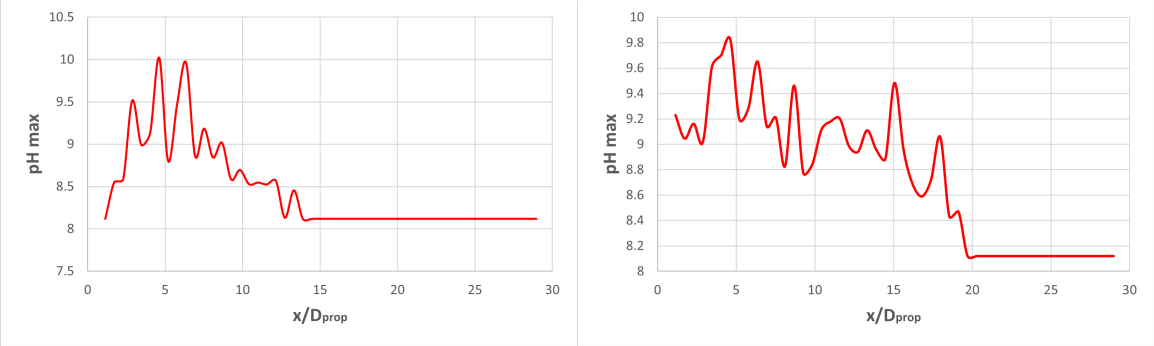

Figure 6.63: Axial profile of maximum pH for propeller only simulation (left) and bluff body simulation (right) at about t=90

At the equal mass flow rates of the simulations, it is evident from figure 6.62 that the turbulent recirculation region, after the bluff body, accentuates the mixing and dissolution of slaked lime, with a faster reduction of maximum concentration values in the axial direction (with the exception of an isolated peak at about $x/D_{prop} = 13$). Such effects generate an increase in seawater alkalinity, that extends more in axial and transversal directions than the simulation with the absence of the bluff body.

A confirmation of the previous statement can be found in the following visualisations of concentration and pH iso-surfaces:

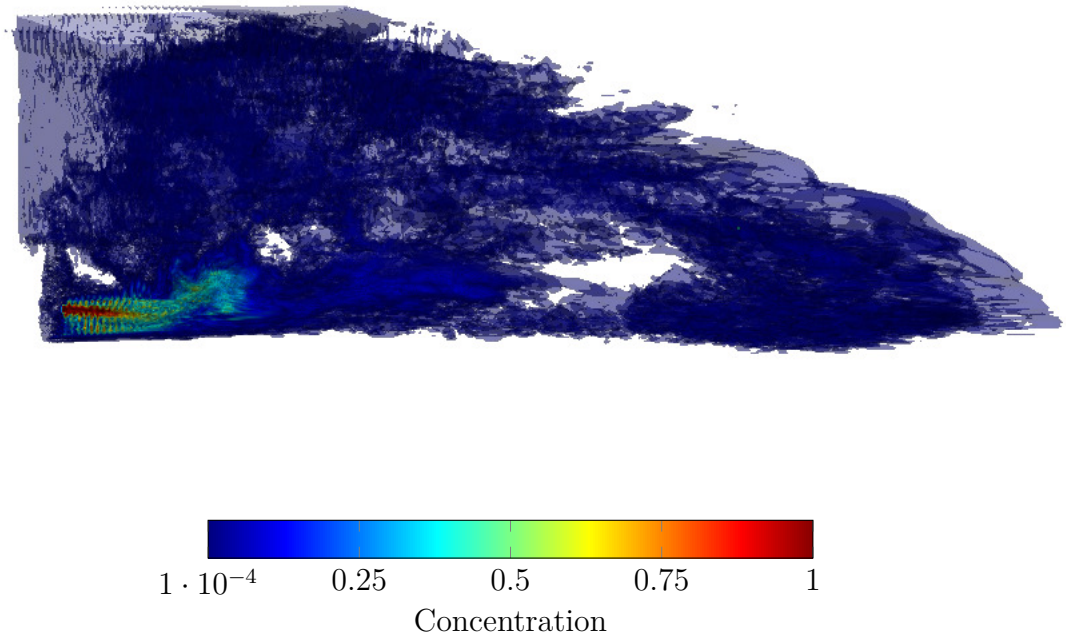

Figure 6.64: Iso-surfaces of concentration along axial direction for bluff body simulation

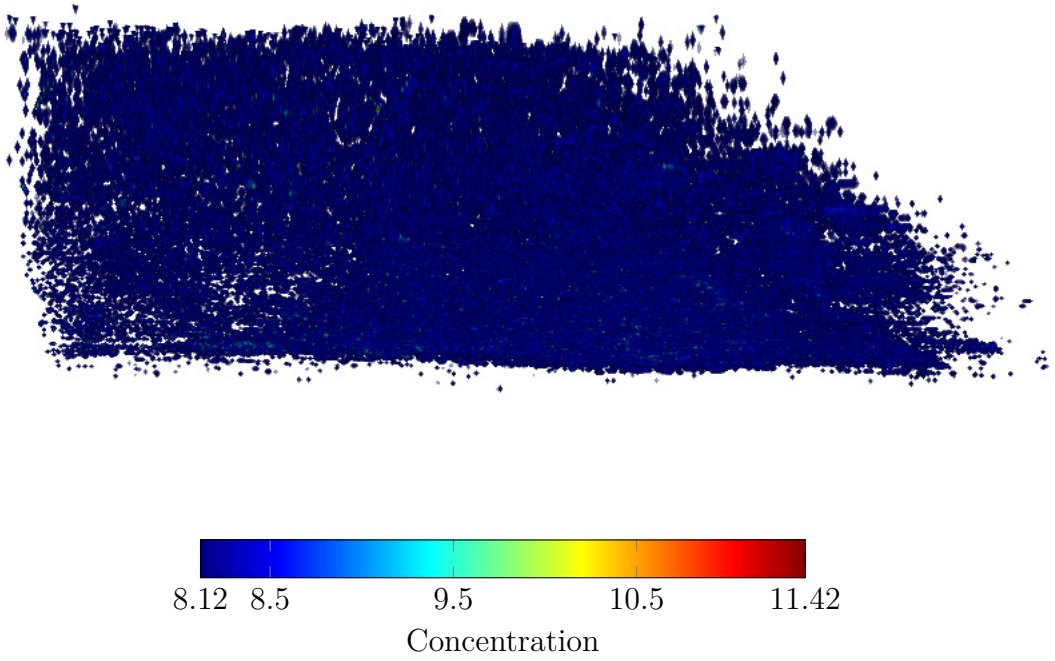

Figure 6.65: Iso-surfaces of pH along axial direction for bluff body simulation

From figures 6.64 and 6.65 it is evident that the turbulent recirculation region right after the bluff body makes the slaked lime to diffuse in a much larger area than the case of simulation without its presence at the inflow. In particular, the turbulent separation beyond the bluff body tends to force the propeller wake towards the upper part of the domain. The process just described can be found analysing the concentration distribution along y-direction in different axial locations:

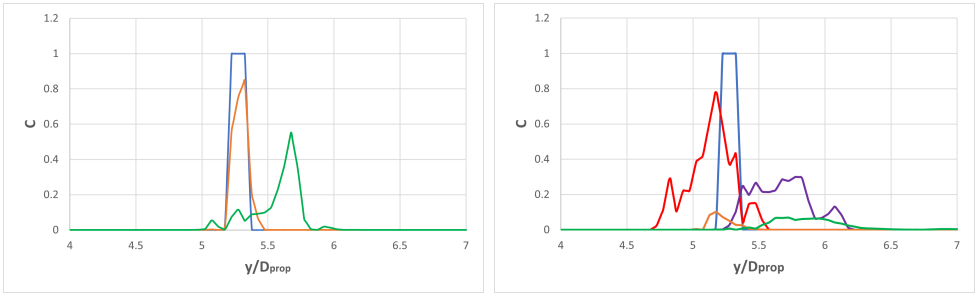

Figure 6.66: Concentration distribution along y-direction in different axial locations, cases propeller only (left) bluff body (right)

The simulation with the addition of a bluff body at the inlet makes the concentration to move towards the upper part of the computational domain. In the end, it is interesting to analyse the time evolution of slaked lime concentration and seawater pH. As stated in previous Sections, the temporal data have been collected at about 1 diameter before the propeller and 2 diameters after the propeller, along the axial direction. The results are presented below in figures 6.67 and 6.68:

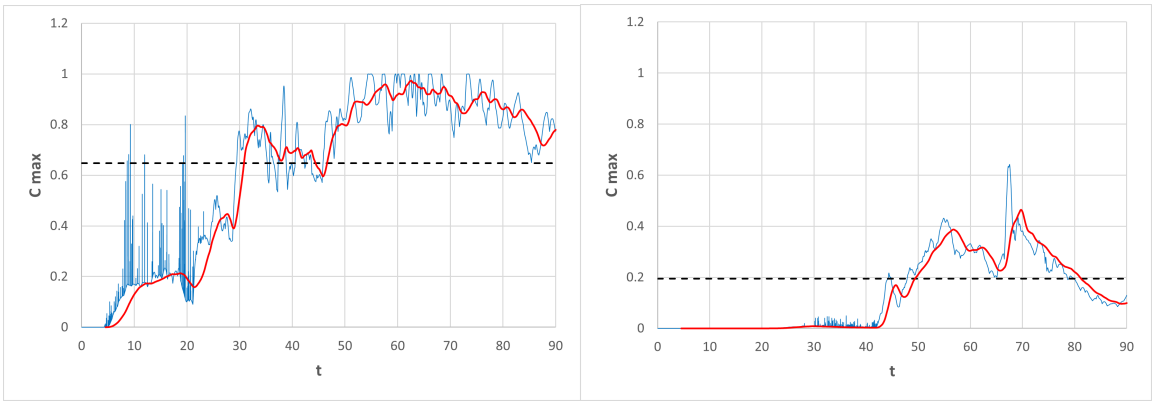

Figure 6.67: Time evolution of maximum concentration along axial direction, before propeller (left) and after propeller (right)

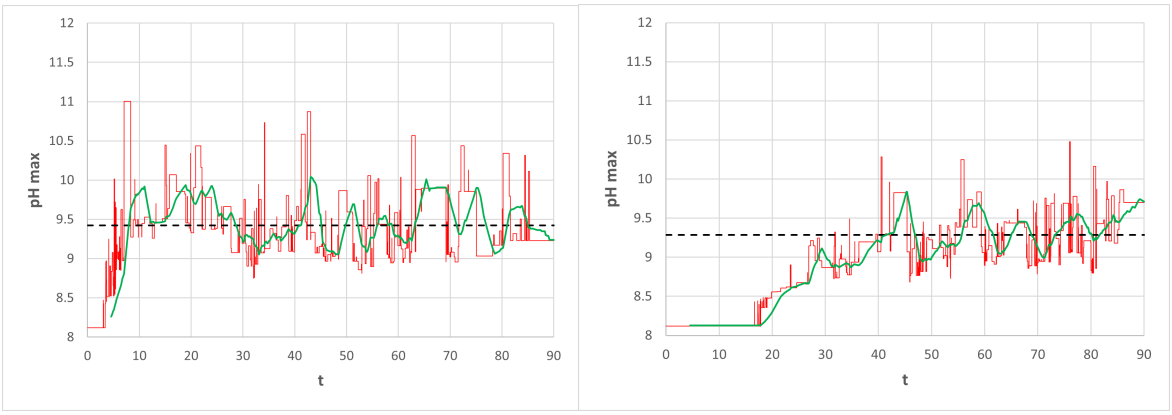

Figure 6.68: Time evolution of maximum pH along axial direction, before propeller (left) and after propeller (right)

The mean value of maximum concentration and pH are summarized in the following table, with the addition of the data collected in the simulation with the propeller only:

	Bluff body	No Bluff body
Before propeller	0.8217	0.9871
After propeller	0.1948	0.8809

Table 6.7: Values of the maximum concentration ensemble averages, with and without bluff body

	Bluff body	No Bluff body
Before propeller	9.42	9.11
After propeller	9.29	8.79

Table 6.8: Values of the maximum pH ensemble averages, with and without bluff body

In light of the presented results, it can be highlighted that the presence of the bluff body causes a much larger diffusion and dilution of the injected calcium hydroxide, with consequent higher values of seawater pH. The hull wake stucks the slaked lime in the region right after it, activating immediately the reaction between slaked lime and water and preventing it to advance farther in axial direction.

7. Conclusions and future remarks

The present thesis work has, first of all, brought to the development of an useful tool for future analysis. Nevertheless, important results in the analysis of calcium hydroxide dynamics and reaction have been obtained.

Firstly, it is truly important to highlight how much a different propeller affects the diffusion and reaction of the slaked lime. Keeping this in mind, the choice of an appropriate propeller (or even suitable ship) could be a key factor for the optimization of slaked lime transportation and discharge. The data taken from the simulations show that the propeller with a lower advance ratio (but higher hydrodynamic coefficients) generates a larger pH increase after it; because of its superior mixing, it facilitates the reaction between slaked lime and water. The second big variations among the simulations is the injection mass flow rate. The greatest difference which can be inferred from the data is how much the slaked lime can affect the near region after the propeller. Therefore when using a higher mass flow rate, as it is shown in concentration and pH average distributions, the effect on this portion of seawater is certainly larger. This behaviour is still verified both for the single injection and double injection. Fixing the flow rate at 100 kg/s, the data shows that there seems to not be a great difference in the seawater pH, despite of the lower levels of concentration in the double injection configuration. This could be caused by a diffusion of slaked lime on a larger area. The extension of concentration and pH perturbation along the axial direction is very similar with both injection layouts. Lastly, the introduction of the bluff body has the effect of accentuating the slaked lime diffusion and on a greater region. In addition, thanks to the high turbulence generated, also the dissolution is emphasised. In the end, the following conclusion can be made: although the peaks of maximum pH encountered in all the configurations simulated are very strong, with possible dangerous consequences for surrounding marine environment, they are very short in time and localized in space; this is confirmed by the analysis of mean values of maximum pH across transversal sections of the domain, as shown in figures 6.57 and 6.59. Therefore, the ocean flora and fauna should not to be exposed to high pH values for an extended period of time.

For the future development of the work many are the aspects to be improved. Starting from an improved LES solver, where the Smagorinsky model for subgrid stress tensor in the filtered NS equations can be replaced by an anisotropic dynamic model, that can allow the backscatter process in the scales energy transfer and represents the smallest scales anisotropy. Concern-

ing the setup of the simulations, the propeller can be simulated considering its real geometry, without implementing a RADM, combined with BET, physical model. Similar considerations can be done for the physical model of the ship hull. As stated in the previous Section 6.2, modelling the ship hull with a bluff body implies to have a strong recirculation region, negatively influencing the resulting dilution of slaked lime. Therefore, the simulation of a more hydrodynamic shape of the hull, for example with the immersed boundary method, would make the study more complete and realistic. It is worth noticing that such modifications necessarily make the simulations more demanding from a computational point of view. Regarding the model used for simulating the dissolution of $Ca(OH)_2$ in seawater, it would be very useful to further investigate the nature of concentration and pH peaks described in Sections 6.1.4 and 6.1.5, as well as a wider range of values for diffusion potential Φ_0. Finally, the biggest step to complete the research would be the integration of a chemical software (*e.g.* PHREEQC by U.S. Geological Survey Survey, mentioned in Caserini et al. [2021]), for analysing the dilution of $Ca(OH)_2$ and the pH seawater, in the fluidynamic solver. This interaction would allow to avoid the approximations implemented in the present work for the study of seawater pH and slaked lime concentration dynamics. In relation to this, it could be very useful to study the evolution of seawater pH in a fixed region, after the injection of slaked lime, for a larger period of time than the one simulated in this work.

A. Numerical Approximations

This appendix contains the discretization procedure for the governing equations solved in the code. In particular, both the convective and diffusive terms are made explicit.

A.1 Mimetic Scheme

The following are the approximations of the continuity and momentum equations, which uses the mimetic scheme:

$$\nabla \cdot (\boldsymbol{u})_{i,j,k} = 0 \tag{A.1}$$

$$\frac{\partial u_{i+1/2,j,k}}{\partial t} = -\nabla \cdot (\boldsymbol{uu})_{i+1/2,j,k} - \delta_x \left(p + \overline{K}\right)_{i+1/2,j,k} + \frac{1}{Re}\nabla^2 (\boldsymbol{u})_{i+1/2,j,k} \tag{A.2a}$$

$$\nabla \cdot (\boldsymbol{uu})_{i+1/2,j,k} = \overline{\omega}^y_{i+1/2,j,k}\overline{w}_{i+1/2,j,k} - \overline{\omega}^z_{i+1/2,j,k}\overline{v}_{i+1/2,j,k} \tag{A.2b}$$

$$\nabla^2 (\boldsymbol{u})_{i+1/2,j,k} = \delta_z \left(\omega^y\right)_{i+1/2,j,k} - \delta_y \left(\omega^z\right)_{i+1/2,j,k} \tag{A.2c}$$

$$\frac{\partial v_{i,j+1/2,k}}{\partial t} = -\delta_y(p + \overline{K})_{i,j+1/2,k} + \frac{1}{Re}\nabla^2 (\boldsymbol{uu})_{i,j+1/2,k} \tag{A.2d}$$

$$\nabla \cdot (\boldsymbol{uu})_{i,j+1/2,k} = \overline{\omega}^z_{i,j+1/2,k}\overline{u}_{i,j+1/2,k} - \overline{\omega}^x_{i,j+1/2,k}\overline{w}_{i,j+1/2,k} \tag{A.2e}$$

$$\nabla^2 (\boldsymbol{u})_{i,j+1/2,k} = \delta_x(\omega^z)_{i,j+1/2,k} - \delta_z(\omega^x)_{i,j+1/2,k} \tag{A.2f}$$

$$\frac{\partial w_{i,j,k+1/2}}{\partial t} = -\delta_z(p + \overline{K})_{i,j,k+1/2} + \frac{1}{Re}\nabla^2 (\boldsymbol{u})_{i,j,k+1/2} \tag{A.2g}$$

$$\nabla \cdot (\boldsymbol{uu})_{i,j,k+1/2} = \overline{\omega}^x_{i,j,k+1/2}\overline{w}_{i,j,k+1/2} - \overline{\omega}^y_{i,j,k+1/2}\overline{u}_{i,j,k+1/2} \tag{A.2h}$$

$$\nabla^2 (\boldsymbol{u})_{i,j,k+1/2} = \delta_y(\omega)_{i,j,k+1/2} - \delta_x(\omega)_{i,j,k+1/2} \tag{A.2i}$$

The quantities defined by an overbar are the variables linearly interpolated at points where they are not defined. Moreover, the spatial discretization of first and second order derivatives is computed with second-order accuracy.

A.2 Conservative Scheme

Here are presented the approximations of the concentration and particle radius equations, which use the conservative scheme:

$$\frac{\partial C_{i,j,k}}{\partial t} = -\nabla \cdot (\boldsymbol{u}C)_{i,j,k} + \frac{1}{ReSc}\nabla^2(C)_{i,j,k} + S_c \tag{A.3a}$$

$$\begin{aligned}\nabla \cdot (\boldsymbol{u}C)_{i,j,k} = &\left[u_{i+1/2,j,k}\overline{C}_{i+1/2,j,k} - u_{i-1/2,j,k}\overline{C}_{i-1/2,j,k}\right]\frac{1}{\Delta x_i} \\ &- \left[v_{i,j+1/2,k}\overline{C}_{i,j+1/2,k} - v_{i,j-1/2,k}\overline{C}_{i,j-1/2,k}\right]\frac{1}{\Delta y_j} \\ &- \left[w_{i,j,k+1/2}\overline{C}_{i,j,k+1/2} - w_{i,j,k-1/2}\overline{C}_{i,j,k-1/2}\right]\frac{1}{\Delta z_k}\end{aligned} \tag{A.3b}$$

$$\begin{aligned}\nabla^2(C)_{i,j,k} = &\left[\left(\frac{C_{i+1,j,k} - C_{i,j,k}}{\Delta x_{i+1}} - \frac{C_{i,j,k} - C_{i-1,j,k}}{\Delta x_i}\right)\frac{2}{\Delta x_i}\right. \\ &+ \left(\frac{C_{i,j+1,k} - C_{i,j,k}}{\Delta y_{j+1}} - \frac{C_{i,j,k} - C_{i,j-1,k}}{\Delta y_j}\right)\frac{2}{\Delta y_j} \\ &\left.+ \left(\frac{C_{i,j,k+1} - C_{i,j,k}}{\Delta z_{k+1}} - \frac{C_{i,j,k} - C_{i,j,k-1}}{\Delta z_k}\right)\frac{2}{\Delta z_k}\right]\end{aligned} \tag{A.3c}$$

$$\frac{\partial r_{p_{i,j,k}}}{\partial t} = -\nabla \cdot (\boldsymbol{u}r_p)_{i,j,k} + S_{r_p} \tag{A.4a}$$

$$\begin{aligned}\nabla \cdot (\boldsymbol{u}r_p)_{i,j,k} = &\left[u_{i+1/2,j,k}\overline{r}_{p_{i+1/2,j,k}} - u_{i-1/2,j,k}\overline{r}_{p_{i-1/2,j,k}}\right]\frac{1}{\Delta x_i} \\ &- \left[v_{i,j+1/2,k}\overline{r}_{p_{i,j+1/2,k}} - v_{i,j-1/2,k}\overline{r}_{p_{i,j-1/2,k}}\right]\frac{1}{\Delta y_j} \\ &- \left[w_{i,j,k+1/2}\overline{r}_{p_{i,j,k+1/2}} - w_{i,j,k-1/2}\overline{r}_{p_{i,j,k-1/2}}\right]\frac{1}{\Delta z_k}\end{aligned} \tag{A.4b}$$

The variables characterized by an overbar are the quantities linearly interpolated at points where they are not defined.

Bibliography

F. S. A. Quarteroni. *Calcolo Scientifico*. Springer-Verlag Italia, Milan, Italy, 2008.

A. Abbà and L. Bonaventura. A mimetic finite difference discretization for the incompressible navier–stokes equations. *Int. J. Numer. Meth. Fluids*, 56(3):1101–1106, 2008. doi: 10.1002/fld.1678.

S. Alekseenko, A. Bilsky, V. Dulin, B. Ilyushin, and D. Markovich. Non-intrusive determination of turbulent energy balance in free and confined jet flows. *Proc.* 4_{th} *Intern. Symp. on Turbulence and Shear Flow Phenomena (TSFP-4)*, pages 605–610, 2005.

U. Bathmann. LOHAFEX: Overview about the concept and first results of the indian-german iron fertilization experiment. *32nd meeting of the London Convention and the London Protocol*, 25th May 2009, Rome. doi: http://hdl.handle.net/10013/epic.32728.d001.

B. Boersma, G. Brethouwer, and F. Nieuwstadt. A numerical investigation on the effect of the inflow conditions on the self-similar region of a round jet. *Physics of Fluids*, 10(4):899–909, 1998. doi: 10.1063/1.869626.

R. Byrne and T. Dietz. Ion transport and acid-base balance in freshwater bivalves. *J. Exp. Biol.*, 200(3):457–465, 1997. doi: 10.1242/jeb.200.3.457.

S. Caserini, D. Pagano, F. Campo, A. Abbà, S. D. Marco, D. Righi, M. Grosso, and P. Renforth. Potential of maritime transport for ocean liming and atmospheric CO_2 removal. *frontiers in Climate*, 2021. doi: 10.3389/fclim.2021.575900.

A. Chorin. Numerical solution of the navier-stokes equations. *Mathematics Of Computation*, 22(104):745–762, 1968. doi: 10.1090/S0025-5718-1968-0242392-2.

H. T. Chou. On the dilution of liquid waste in ships' wakes. *Journal of marine science and technology*, 1:149–154, 1996.

U. Ciri, K. Carrasquillo, C. Santoni, V. Iungo, M. Salvetti, and S. Leonardi. Effects of the subgrid-scale modeling in the large eddy simulations of wind turbines and wind farms. *Direct and Large-Eddy Simulation 10*, 2015.

G. Cripps, S. Widdicombe, J. Spicer, and H. Findlay. Biological impacts of enhanced alkalinity in carcinus maenas. *Mar. Pollut. Bull*, 71(1-2):190–198, 2013. doi: 10.1016/j.marpolbul.2013.03.015.

G. Cripps, P. Lindeque, and K. J. Flynn. Sequestering atmospheric carbon dioxide by increasing ocean alkalinity. *Global Change Biology*, 20(11):3377–3385, 2014. doi: 10.1111/gcb.12582.

M. Dall'Aglio. *Simulation of slaked lime discharge in the wake of a ship*. Master Thesis in Aeronautical Engineering, Politecnico di Milano, Milano, 2019.

Desarc-Maresanus. Desarc maresanus contrastare l'acidificazione dei mari rimuovendo carbonio dall'atmosfera. URL `http://www.desarc-maresanus.net`. Accessed: 2021-05-24.

J. Fuhrman and D. Capone. Possible biogeochemical consequences of ocean fertilization. *Limnol. Oceanogr.*, 36(8):1951–1959, 1991. doi: 10.4319/lo.1991.36.8.1951.

M. Germano. A proposal for a redefinition of the turbulent stresses in the filtered navier–stokes equations. *Phys. Fluids*, 29(7):2323–2324, 1986.

M. Germano, U. Piomelli, P. Moin, and W. Cabot. A dynamic subgrid-scale eddy viscosity model. *Phys. Fluids*, 3(7):1760–1765, 1991.

J. Guermond and P. Minev. A new class of massively parallel direction splitting for the incompressible navier–stokes equations. *Comput. Methods Appl. Mech. Engrg.*, 200(23-24):2083–2093, 2011. doi: 10.1016/j.cma.2011.02.007.

F. H. Harlow and J. E. Welch. Numerical calculation of time-dependent viscous incrompressible flow of fluid with free surface. *The Physics of Fluids*, 8(12):2182–2189, 1965. doi: 10.1063/1.1761178.

G. Henderson, R.Rickaby, and H. Bouman. Decreasing atmosphere co_2 by increasing ocean alkalinity. 2008.

H. Hussein, S. Capp, and W. George. Velocity measurements in a high reynolds number, momentum-conserving axisymmetric turbulent jet. *J. Fluid Mech.*, 258:31–75, 1994. doi: 10.1017/S002211209400323X.

B. Ilyushin and D. Krasinsky. Large eddy simulation of the turbulent round jet dynamics. *Thermophysics and Aeromechanics*, 13(1):43–54, 2006. doi: 10.1134/S1531869906010059.

C. Kennedy, M. Carpenter, and R. Lewis. Low-storage, explicit runge–kutta schemes for the compressible navier–stokes equations. *Applied Numerical Mathematics*, 35(3):177–219, 2000. doi: 10.1016/S0168-9274(99)00141-5.

H. S. Kheshgi. Sequestering atmospheric carbon dioxide by increasing ocean alkalinity. *Energy*, 20:915–922, 1995.

P. Kundu, I. Cohen, and D. Dowling. *Fluid Mechanics, Fifth Edition*. Elsevier, 2011.

A. Leonard. Energy cascade in large-eddy simulations of turbulent fluid flows. *Adv. in Geophys. A*, 18:237–248, 1974.

M. Lesieur and R. Rogallo. Large-eddy simulation of passive scalar diffusion in isotropic turbulence. *Phys. Fluids A*, 1(4):718–722, 1989.

A. Locke, K. Doe, W. Fairchild, P. Jackman, and E. Reese. Preliminary evaluation of effects of invasive tunicate management with acetic acid and calcium hydroxide on non-target marine organisms in prince edward island, canada. *Aquat. Invasions*, 4(1):221–236, 2009. doi: 10.3391/ai.2009.4.1.23.

L. Martinez-Tossas, M. Churchfield, and S. Leonardi. Large eddy simulations of the flow past wind turbines: actuator line and disk modeling. *Wind Energy*, 18(6):1047–1060, 2015. doi: 10.1002/we.1747.

OpenFOAM. Openfoam: User guide: Rotor disk. URL `http://www.openfoam.com/documentation/guides/latest/doc/guide-fvoptions-sources-rotor-disk.html`. Accessed: 2021-05-24.

S. V. Patankar. *Patankar Numerical Heat transfer and Fluid flow*. Taylor & Francis, Milton Park, Oxfordshire United Kingdom, 1980.

R. Peyret and T. Taylor. *Computational methods for fluid flow*. Springer Science & Business Media, 2012.

S. Pope. *Turbulent Flows*. Cambridge University Press, Cornell University, New York, 2000.

A. Quarteroni. *Modellistica Numerica per Problemi Differenziali*. Springer-Verlag Mailand, Lausanne, Switzerland, 2016.

R.Courant, K.Friedrichs, and H.Lewy. On the partial difference equations of mathematical physics. *IBM Journal of Research and Development*, 11(2):215–234, 1967. doi: 10.1147/rd.112.0215.

P. Renforth and G. Henderson. Assessing ocean alkalinity for carbon sequestration. *Reviews of Geophysics*, 55:636–674, 2017. doi: 10.1002/2016RG000533.

P. Renforth, B. G. Jenkins, and T. Kruger. Engineering challenges of ocean liming. *Energy*, 60:442–452, 2013. doi: http://dx.doi.org/10.1016/j.energy.2013.08.006.

A. Ridgwell and R. Zeebe. The role of the global carbonate cycle in the regulation and evolution of the earh system. *Earth and PLanetary Science Letters*, 234:299–315, 2005. doi: 10.1016/j.epsl.2005.03.006.

P. Sagaut. *Large Eddy Simulation for Incompressible Flows*. Springer, Paris, France, 2006.

D. Scott, M. Lucas, and R. Wilson. The effect of high ph on ion balance, nitrogen excretion and behaviour in freshwater fish from an eutrophic lake: A laboratory and field study. *Aquat. Toxicol.*, 73(1):31–43, 2005. doi: 10.1016/j.aquatox.2004.12.013.

J. Smagorinsky. General circulation experiments with the primitive equations. *Month. Weath. Rev.*, 91(3):99–165, 1963.

K. R. Sreenivasan. Turbulent mixing: a perspective. *PNAS*, 116(37):18175–18183, 2019. doi: 10.1073/pnas.1800463115.

U. G. Survey. Phreeqc. URL `www.usgs.gov/software/phreeqc-version-3`. Accessed: 2021-05-24.

M. Tannenberger and H. Klein. Settling and dissolution of calcium hydroxide particles. *München: Lehrstuhl für Anlagen und Prozesstechnik; Semesterarbeit*, 2009.

J. Taucher, L. T. Bach, T. Boxhammer, J. Nauendorf, and T. G. C. K. Consortium. Influence of ocean acidification and deep water upwelling on oligotrphic plankton communities in the subtropical north atlantic: Insights from a in situ mesocosm study. *Frontiers in Marine Science*, 4(85), 2017. doi: 10.3389/fmars.2017.00085.

I. Wygnanski and H. Fiedler. Some measurements in the self-preserving jet. *J. Fluid Mech.*, 38(3):577–612, 1969. doi: 10.1017/S0022112069000358.

T. Zanelli. *Large Eddy Simulation of Turbulent Flows by a Direction Splitting Solver in Complex Geometries*. Master Thesis in Aeronautical Engineering, Politecnico di Milano, Milano, 2018.

M. Zangrandi. *Aerodynamics over complex terrains and its effects on wind farm power production: an LES study*. Master Thesis in Aeronautical Engineering, Politecnico di Milano, Milano, 2019.

L. Zhiheng, Y. Jiawei, F. Dakui, J. Kaijun, and Z. Yujie. Research on the improved body-force method based on viscous flow. *Proceedings of the ASME 2019* 38^{th} *International Conference on Ocean, Offshore and Arctic Engineering*, 2019. doi: 10.1115/OMAE2019-95887.